To the Graduate Council:

I am submitting herewith a dissertation written by Syed-Ahmed Mohammed Said entitled "An Analytical And Experimental Investigation Of Natural Convection Heat Transfer In Vertical Channels With A Single Obstruction." I have examined the final copy of this dissertation for form and content and recommend that it be accepted in partial fulfillment of the requirements for the degree of Doctor of Philosophy, with a major in Mechanical Engineering.

R. J. Krane, Major Professor

We have read this dissertation and recommend its acceptance:

Accepted for the Council:

Vice Provost
and Dean of The Graduate School

AN ANALYTICAL AND EXPERIMENTAL INVESTIGATION OF NATURAL CONVECTION HEAT TRANSFER IN VERTICAL CHANNELS WITH A SINGLE OBSTRUCTION

A Dissertation
Presented for the
Doctor of Philosophy
Degree
The University of Tennessee, Knoxville

Syed-Ahmed M. Said

March 1986

ACKNOWLEDGMENTS

The author would like to express his sincere appreciation to Professor R.J. Krane for his constant guidance and continued interest during this study. His encouragement and constant help made this work possible. I am also grateful to the other members of the doctoral committee, J.W. Hodgson, J.R. Parsons and J.J. Perona for their careful review of this study.

The author acknowledges all the people with whom he has had the pleasure to work with over the past three years and to thank them for the pleasure of their company. A special thanks is due to my colleagues, the graduate students for their consistent help and encouragement.

A special thanks is due to Jenny Wren for her careful typing of the manuscript.

The author wishes to dedicate this dissertation to his parents, wife and children.

The author's study at UTK was supported by the Research Institute of the University of Petroleum and Minerals, Dhahran, Saudi Arabia.

ABSTRACT

This dissertation is concerned with the heat transfer due to natural convection flows of air in a vertical channel with a single obstruction. The work is separated into two sections: one dealing with experimental measurements and the other with the numerical solution of the two-dimensional conservation equations.

The numerical work consists of the solution of the governing differential equations. The equations which are derived using the Boussinesq approximation, are solved using a general purpose finite element computer code called NACHOS. The NACHOS program is based on the Galerkin form of the finite element method (FEM) and is designed for the solution of transient or steady state laminar flows described by the Navier-Stokes equations. Both thermal boundary conditions, uniform wall temperature (UWT) and uniform heat flux (UHF), are considered numerically.

In the experimental study, optical techniques were used to obtain measurements of both quantitative data (heat fluxes and temperatures) and qualitative data (flow visualization). The range of Rayleigh numbers for these tests was $2 \times 10^3 < Ra \leq 10^5$. Only uniform wall temperature (UWT) boundary conditions were investigated experimentally.

The main objective of this dissertation is to perform a combined numerical and experimental study of the effects of a single obstruction on natural convection flows in a vertical channel. It is found that the presence of the obstruction reduces the average Nusselt number by 5% at a Rayleigh number (Ra′) of 10^4 to about 40% at a Rayleigh number (Ra′) of 10, for a uniform wall temperature (UWT) boundary condition. It is also found that

the location of the obstruction along the wall affects the rate of heat transfer. Moving the obstruction away from the entrance towards the exit reduces the the average heat transfer rate for the channel. For the case of uniform heat flux (UHF) boundary conditions; it is found that the maximum temperature occurs at the intersection of the top edge of the obstruction and the wall is only 4% higher than the maximum temperature for an unobstructed channel (which occurs at the exit of the channel).

TABLE OF CONTENTS

CHAPTER	PAGE

LIST OF TABLES

LIST OF FIGURES

FIGURE		PAGE

FIGURE		PAGE

NOMENCLATURE

AR	aspect ratio of the channel (b/L)
b	channel width
C_p	specific heat of fluid
g	magnitude of the acceleration to the gravity
Gr	Grashof number, $g\beta(T_w - T_\infty)b^3/\nu^2$
Gr*	modified Grashof number, $g\beta q_w b^4/\nu^2 K$
K	fluid thermal conductivity
L	channel height
L_1	obstruction height from channel entrance, see Figure 4
P	motion pressure
P	dimensionless pressure, $(P - P_\infty)/g\beta\rho_\infty(\Delta T)L$ for UWT
P*	modified dimensionless pressure, $(P - P_\infty)K/g\beta\rho_\infty q_w bL$ for UHF
P_∞	hydrostatic fluid pressure
Pr	Prandtl number, ν/α
q_w	wall heat flux
r	obstruction radius, see Figure 4
Ra	Rayleigh number, (= Pr Gr)
Ra*	modified Rayleigh number, (= Pr Gr*)
Ra′	Rayleigh number, (= Ra AR)
T	fluid temperature
ΔT	$(T_w - T_\infty)$
u	x-component of velocity
u	dimensionless x-component of velocity, $(= ub^2/\alpha L)$
v	y-component of velocity

v	dimensionless y-component of velocity, (= vb^2/α)
x, y	spatial coordinates, see Figure 4
α	thermal diffusivity
β	thermal expansion coefficient of fluid
μ	dynamic viscosity of fluid
ν	kinematic viscosity of fluid
ρ	density of fluid
θ	dimensionless temperature, $(T - T_\infty)/(T_w - T_\infty)$ for UWT
θ'	dimensionless temperature, $(T - T_\infty)/(q_w b/k)$ for UHF
θ_{max}	dimensionless maximum temperature, $(T_{max} - T_\infty)/(q_w b/k)$ for UHF

<u>Superscripts</u>

i	refers to one of the vertical walls of the obstructed channel
w	wall value
max	maximum value
x	value at distance x from channel entrance
∞	indicating the conditions at infinity

CHAPTER I

INTRODUCTION

1.1 Motivation for the Present Research

Steady-state natural convection flows in vertical channels are of interest in a number of engineering applications. One of these applications is the natural convection cooling of electronic cabinets containing circuit cards which are aligned to form vertical channels, as shown in Figure 1*. Designers prefer to cool electronic equipment by natural convection because of the inherent high reliability of this technique. Some personal computers and pieces of peripheral equipment for these computers are designed to operate with natural convection cooling, though a fan may be used in a few cases to increase the heat transfer rate for long periods of operation and in environments that are at relatively higher temperatures than normal room temperature. A second application of natural convection flows in channels is the cooling of nuclear reactors by natural convection flows produced by the temperature difference between the nuclear reactor core and the gas surrounding it.

As will be shown in Section 1.2, unobstructed natural convection channel flows have been extensively investigated and many aspects of these flows are presently well understood. For the purposes of this investigation, an "obstruction" in a flow channel is defined as a protrusion from a channel wall. When the channels do not contain obstructions, the governing equations describing the flows are parabolic in nature and their analyses may

---

* All figures will be found in Appendix F.

be based on the boundary layer equations. The presence of obstructions in a channel, however, results in flows of an elliptic nature. This change from parabolic to elliptic flows is due to the formation of regions of recirculating flow that are created when an obstruction causes the main flow to separate from the channel walls, as shown in Figure 2.

In contrast to unobstructed flows, little is known about the detailed nature of obstructed natural convection flows in channels. Since obstructed flows are elliptic, however, their analysis cannot be based on the boundary layer equations. Also, the computation of these elliptic flows is much more difficult than the computation of the parabolic flows since the boundaries of the regions of separated flow are initially unknown, and must be determined as part of the solution. The lack of knowledge of these practically-important flows and the need for such an investigation were discussed by Aung [1], [2] at recent meetings on natural convection heat transfer. Thus, we may conclude that there is a definite need for investigation of the effects of obstructions on natural convection flows in vertical channels. Hence, the objective of this research is to perform a combined numerical and experimental study of the effects of obstructions on natural convection flows in vertical channels.

1.2 Literature Review

Natural convection heat transfer has been the subject of a considerable amount of research in recent years. This subject has been extensively reviewed in the books by Jaluria [3], Bejan [4], and Kakac, et al. [5]. Reviews of the importance of heat transfer considerations in the design of electronic equipment have been given by Aung and Chimah [6], Jaluria [7] and Kraus and Bar-Cohen [8].

Many diverse flow configurations are of interest in electronic cooling applications. The most important of these configurations is the vertical channel. Laminar, natural convection heat transfer in vertical channels has been investigated theoretically (on the basis of boundary layer equations), as well as experimentally. Representative contributions to the analytical literature on the subject include several investigators. Engel and Mueller [9] analyzed the development of natural convection in channels of finite length for a wide range of Prandtl and Rayleigh numbers for both the constant wall temperature and constant wall heat-flux boundary conditions. Bodoia and Osterle [10] have investigated the development of free convection in an isothermal vertical channel by using the finite-difference method to numerically integrate the boundary layer equations. Aung and co-workers [11] have investigated numerically and experimentally the development of free convection heat transfer in vertical channels with asymmetric heating. They considered both thermal boundary conditions of uniform wall heat fluxes and uniform wall temperature. Miyatake, et al. [12] analyzed numerically the natural convection heat transfer between two vertical parallel plates where uniform heat flux is applied to one plate, while the other plate is thermally insulated. In another study, Miyatake and Fujii [13] analyzed the same problem with one plate isothermally heated and the other thermally insulated. Aung, et al. [14] have studied numerically and experimentally natural convection cooling of arrays of vertically-oriented circuit cards aligned to form vertical channels or ducts. Coyne [15] also has investigated the same problem analytically. This analysis involves the calculation of the steady-state, laminar, two-dimensional parabolic flow in vertical channels. Kettleborough [16] studied numerically the transient laminar free convection in a heated vertical channel. Nakamura, et al. [17] performed a numerical analysis of the same problem as Kettleborough without using the boundary-layer approximation. Burch, et al. [18] used a finite difference procedure to investigate the problem of laminar natural convection between finitely conducting vertical plates. Carpenter [19] investigated numerically the interaction of radiation with developing free convective heat transfer in vertical parallel plate channels with asymmetric heating. Aihara [20] studied the effect of inlet boundary-conditions on the numerical solution of free convection flow in vertical channels. The three-dimensional buoyancy-induced flow in a duct has been analyzed in the studies by Karki and Patankar [21], and Ramakrishna, et al. [22]. Similar analysis for vertical circular tubes has been analyzed in the studies by Davis and Perona [23], Kageyama and Izumi [24], and Dyer [25].

The original experimental study of natural convection between parallel plates is that of Elenbass [26]. Ebenbass' results are often compared with analytical results for parallel plate channels. Natural convection heat transfer measurements for vertical channels with different temperature isothermal walls are presented in the work of Sernas, et al. [27]. A recent experimental study by Sparrow and Bahrami [28], encompasses three types of hydro-dynamic boundary conditions along the lateral edges of the channel. Akbari and Borges [29] solved numerically the two-dimensional, free convective, laminar flow in the Trombe wall channel; while Tichy, [30] solved the same problem using an Oseen-type approximation. Levy, et al. [31] address the problem of optimum plate spacings for laminar natural convection flow between two plates. Churchill [32], using the theoretical and experimental results obtained by a number of authors for the mean rate of heat transfer in laminar, buoyancy driven flow through vertical channels, developed a general correlation equation for these results. Sparrow and Prakash [33] and Prakash and Sparrow [34] dealt with natural convection in vertical arrays of interrupted parallel plates. Aung, et al. [14] made an attempt to derive a general expression which account for the effect of flow restrictions while still considering the governing equation to be parabolic. Flow restrictions encountered in Aung's study [14] are in the form of staggered cards and baffles (see Figure 3).

When obstructions are located inside a channel, (as encountered in many practical applications), the problem becomes elliptic. Very little is known regarding the natural convection phenomena in such complex flows [1]. Hence, the present study will be concerned with a combined experimental and numerical investigation of the laminar natural convection flows of air in a vertical channel with a single obstruction. Although very useful, the numerical approaches are inherently limited by problems originating from numerical diffusion, calculation instabilities, and the incorrect implementation of boundary conditions. The elimination (or, at least, the minimization) of such deficiencies can be verified by comparison with experimental results. Therefore an experimental investigation aimed at characterizing qualitatively (through flow visualization) and quantitatively (through optical measurements) the natural convection flow field structure for air in a two-dimensional, isothermal channel with an internal obstruction is needed. The experimental and numerical data that will be obtained should be of value to researchers concerned with furthering the fundamental understanding and accurate numerical modeling of such flows.

1.3 A Detailed Statement of the Problem

The present study considers the two-dimensional steady-state, laminar natural convection flows of a Newtonian fluid that occur in the obstructed vertical channel shown in Figure 4. Since this is the first systematic study of natural convection flows in an obstructed channel, the channel is assumed to contain only one obstruction (with a semi-cylindrical shape). Restricting the number of obstructions to one permits attention to be focused on the fundamental phenomena of interest by eliminating the complexities associated with interactions and reducing the number of geometrical parameters that would occur if there were multiple obstructions in the channel. Either uniform wall temperature (UWT), or uniform heat flux (UHF), boundary conditions are assumed to occur on the channel walls and the surface of the obstruction. In either case, the thermal boundary conditions will be symmetrical; that is, the same temperature, or heat flux, is assumed to occur on all of the surfaces of the channel wetted by the flow.

The flows are assumed to be such that they can be adequately modeled by the Boussinesq approximation [3], [35] and that compression work, viscous dissipation, and radiative transport are negligibly small. Thus, the governing equations are given as follows:

Conservation of Mass

$$\frac{\partial \bar{u}}{\partial \bar{x}} + \frac{\partial \bar{v}}{\partial \bar{y}} = 0 \qquad (1)$$

Newton's Second Law

$$\bar{u}\,\frac{\partial \bar{u}}{\partial \bar{x}} + \bar{v}\,\frac{\partial \bar{u}}{\partial \bar{y}} = -\frac{1}{\rho_o}\,\frac{\partial \bar{P}}{\partial \bar{x}} + \nu_o\left(\frac{\partial^2 \bar{u}}{\partial \bar{x}^2} + \frac{\partial^2 \bar{u}}{\partial \bar{y}^2}\right) + g\beta_o(\bar{T} - T_\infty) \tag{2}$$

$$\bar{u}\,\frac{\partial \bar{v}}{\partial \bar{x}} + \bar{v}\,\frac{\partial \bar{v}}{\partial \bar{y}} = -\frac{1}{\rho_o}\,\frac{\partial \bar{P}}{\partial \bar{y}} + \nu_o\left(\frac{\partial^2 \bar{v}}{\partial \bar{x}^2} + \frac{\partial^2 \bar{v}}{\partial \bar{y}^2}\right) \tag{3}$$

Conservation of Energy

$$\left(\rho_o C_{p_o}\right)\left(\bar{u}\,\frac{\partial \bar{T}}{\partial \bar{x}} + \bar{v}\,\frac{\partial \bar{T}}{\partial \bar{y}}\right) = K\left(\frac{\partial^2 \bar{T}}{\partial \bar{x}^2} + \frac{\partial^2 \bar{T}}{\partial \bar{y}^2}\right) \tag{4}$$

where u and v are the velocity components in the x- and y-directions, T is the temperature, P is the "motion pressure" (defined as the actual pressure in fluid less the pressure when the fluid is at rest at a uniform temperature, T_o), g is the magnitude of the acceleration due to gravity, and ρ_0, ν_0, β_0, C_{P_0}, and K_0 are, respectively, the fluid density, kinematic viscosity, coefficient of thermal expansion, constant pressure specific heat, and thermal conductivity of air all evaluated at some reference temperature, T_o.

The boundary conditions for these equations are given by:

$$\begin{array}{lll} & \bar{u} = \bar{v} = 0 & \text{For } \bar{y} = 0 \text{ and } \bar{x} \le (\bar{L}_1 - \bar{r}) \\ & \text{and} & \\ & \bar{T} = T_w\,(= \text{const.}) & \text{For } \bar{y} = 0 \text{ and } \bar{x} \ge (\bar{L}_1 + \bar{r}) \\ \text{or} & \dot{q} = q_w\,(= \text{const.}) & \text{For } \bar{y} = \sqrt{\bar{r}^2 - (\bar{L}_1 - \bar{x})^2} \text{ and } (\bar{L}_1 - \bar{r}) \le \bar{x} \le (\bar{L}_1 + \bar{r}) \end{array} \tag{5}$$

$$\left.\begin{array}{ll} & \bar{u} = \bar{v} = 0 \\ & \text{and} \\ & \bar{T} = T_w\,(= \text{const.}) \\ \text{or} & \dot{q} = q_w\,(= \text{const.}) \end{array}\right\} \quad \text{For} \quad \bar{y} = b \qquad \text{and} \qquad (0 \leq \bar{x} \leq L) \tag{6}$$

$$\left.\begin{array}{r} \partial\bar{u}/\partial\bar{x} = 0 \\ \bar{v} = 0 \\ \partial\bar{T}/\partial\bar{x} = 0 \\ \partial\bar{P}/\partial\bar{x} = 0 \end{array}\right\} \quad \text{For} \quad \bar{x} = L \qquad \text{and} \qquad (0 \leq \bar{y} \leq b) \tag{7}$$

$$\left.\begin{array}{r} \partial\bar{u}/\partial\bar{x} = 0 \\ \bar{v} = 0 \\ \bar{T} = T_\infty \\ \partial\bar{P}/\partial\bar{x} = 0 \end{array}\right\} \quad \text{For} \quad \bar{x} = 0 \qquad \text{and} \qquad (0 \leq \bar{y} \leq b) \tag{8}$$

These equations are now expressed in terms of the following dimensionless variables and parameters

$$u = \frac{\bar{u}\,b^2}{\alpha L}; \quad v = \frac{\bar{v}\,b}{\alpha}; \quad x = \frac{\bar{x}}{L}; \quad y = \frac{\bar{y}}{b}$$

$$r = \frac{\bar{r}}{L}; \quad L_1 = \frac{\overline{L_1}}{L}; \quad Pr = \frac{\nu}{\alpha} \tag{9}$$

For the constant wall temperature (UWT) channel

$$\theta = \frac{(\bar{T} - T_\infty)}{(T_w - T_\infty)}$$

and

$$P = \frac{(\bar{P} - P_\infty)}{g\beta\rho_\infty(T_w - T_\infty)L} ,$$

while for the uniform wall heat flux (UHF) channel

$$\theta = \frac{(\bar{T} - T_\infty)}{q_w b/k}$$

and

$$P = \frac{(\bar{P} - P_\infty)k}{g\beta\rho_\infty q_w b L} .$$

The resulting equations are:

<u>Conservation of mass</u>

$$\frac{\partial u}{\partial x} + \frac{\partial v}{\partial y} = 0 \tag{10}$$

<u>Newton's Second Law</u>

$$\frac{1}{Pr}\left[u\frac{\partial u}{\partial x} + v\frac{\partial u}{\partial y} \right] = Ra\left(\frac{b}{L}\right)\left[\theta - \frac{\partial P}{\partial x}\right] + Pr\left[\left(\frac{b}{L}\right)^2 \frac{\partial^2 u}{\partial x^2} + \frac{\partial^2 u}{\partial y^2}\right] \tag{11}$$

$$\frac{1}{Pr}\left(\frac{b}{L}\right)^2\left[u\frac{\partial v}{\partial x} + v\frac{\partial v}{\partial y} \right] = -Ra\left(\frac{b}{L}\right)\frac{\partial P}{\partial y} + \left(\frac{b}{L}\right)^2\left[\left(\frac{b}{L}\right)^2 \frac{\partial^2 v}{\partial x^2} + \frac{\partial^2 v}{\partial y^2}\right] \tag{12}$$

Conservation of Energy

$$u \frac{\partial \theta}{\partial x} + v \frac{\partial \theta}{\partial y} = \left(\frac{b}{L} \right)^2 \frac{\partial^2 \theta}{\partial x^2} + \frac{\partial^2 \theta}{\partial y^2} \tag{13}$$

where the Rayleigh number, Ra, is given by:

$$Ra = Pr Gr = Pr \frac{\beta g (T_w - T_\infty) b^3}{\nu^2} \quad \textit{for the UWT case}$$

or,

$$Ra = Pr \frac{\beta g q_w b^4}{\nu^2 k} \quad \textit{for the UHF case.}$$

The boundary conditions for equations (10)-(13) are:

$u = v = 0$ — For $y = 0$ and $x \leq (L_1 - r)$

and

$\theta = 1$ — For $y = 0$ and $x \geq (L_1 + r)$ (14)

or $\partial\theta/\partial y = -1$ — For $y = \sqrt{r^2 - (L_1 - x)^2}$ and $(L_1 - r) \leq x \leq (L_1 + r)$

$u = v = 0$

and

$\theta = 1$ — For $y = 1$ and $(0 \leq x \leq 1)$ (15)

or $\partial\theta/\partial y = 1$

$$\left.\begin{aligned} \partial u/\partial x &= 0 \\ v &= 0 \\ \partial\theta/\partial x &= 0 \\ \partial P/\partial x &= 0 \end{aligned}\right\} \quad \text{For} \quad x = 1 \quad \text{and} \quad (0 \leq y \leq 1) \qquad (16)$$

$$\left.\begin{aligned} \partial u/\partial x &= 0 \\ v &= 0 \\ \theta &= 0 \\ \partial P/\partial x &= 0 \end{aligned}\right\} \quad \text{For} \quad x = 0 \quad \text{and} \quad (0 \leq y \leq 1) \qquad (17)$$

In the above boundary conditions, the change of vertical velocity with the direction normal to the boundary ($\partial u/\partial x$) at the channel entrance, and the change of exit temperature with the direction normal to the boundary ($\partial T/\partial x$) are prescribed equal to zero. These boundary conditions are not required to be explicitly enforced at each node along the entrance or the exit when using the finite element algorithm. Instead, they are naturally enforced through the elemental surface integrals generated by the method of weighted residuals (MWR) formulation of the finite element algorithm. Through the method of discretization of the differential equations; the elemental surface integrals vanish as shown by Baker [39]. For the surface integral to vanish, either the dependent variable (called an "essential boundary condition") must be prescribed or its differential with the direction normal to the boundary (called "a natural boundary condition") must vanish. In this problem, we do not know the values of the dependent variables u at the entrance or T at the exit; so we choose the natural boundary conditions. Satisfying these boundary conditions through the elemental surface integral is a so-called "weak enforcement" of Neumann boundary conditions.

CHAPTER II

NUMERICAL STUDY

2.1 Introduction

The boundary value problem outlined in section 1.3 is too complicated for exact solution. Hence, one must resort to the use of a numerical method to obtain a solution for this set of coupled, non-linear, elliptic partial differential equations. Among such methods the finite difference method (FDM) have been most popular [36-38]. Finite difference techniques are particularly convenient for use on domains for which each boundary lies along a constant value of a spatial coordinate; that is, domains with "regularly-shaped" boundaries.

Another numerical method that has been developed to treat problems in convection is the finite element method (FEM) which has been thoroughly described by numerous authors [39-41]. In recent years notable progress has been made in the development of finite element procedures for viscous flows. In these procedures, the generation of discrete equations for a non-uniform mesh, over a domain with an irregular boundary is a relatively straightforward task. This capability for handling irregular boundaries is one of the main advantages of the finite element procedure over the finite difference approach. The second main advantage is that the FEM is computationally more efficient than the FDM in determining quantities such as the wall heat flux [42].

In the present study, the analysis was carried out using the general purpose finite element computer code called NACHOS. The NACHOS code was written by Dr. David K. Gartling of Sandia Laboratories and has been modified to run on the IBM/3081 at The University of Tennessee [43].

The NACHOS program is based on the Galerkin form of the FEM and is designed for the solution of transient or steady state laminar flows described by the Navier-Stokes equations. The derivation of finite element equations on which NACHOS is based has been described in sufficient detail elsewhere [44-45] and will not be repeated here. However, for the sake of completeness, the salient features of the numerical procedure used by the NACHOS code are briefly outlined in Appendix A.

2.2 The Computational Matrix

As shown in section 1.3, the dimensionless parameters of interest in the problem are the Rayleigh number (Ra), the dimensionless distance of the obstruction center line above the bottom of the channel (L_1), and the dimensionless obstruction radius (r). The numerical calculations were performed for 31 different cases. Nine of these cases were run for the unobstructed channel ($r = 0$); of which 8 cases were for the constant wall temperature boundary condition and 1 case for the uniform wall heat flux. The solutions for these cases were obtained for comparison with those of other authors in order to verify the code and the accuracy of the numerical procedure. Twenty-one of the remaining twenty-two cases were run for the obstructed channel ($r = 0.091$) with uniform wall temperature boundary condition; and 1 case was run for the obstructed channel with uniform heat flux boundary condition. The cases for the obstructed channel were performed since it is the primary interest of the present study. The computational matrices are shown in Tables 1 and 2.

Table 1 Computational Matrix for Cases with Uniform Wall Temperature Boundary Condition.

Unobstructed Channel	**Obstructed Channel (r = 0.091)**		
Ra′	**Ra**	**L_1**	**AR**
3.5×10^2	6.8×10	0.50	0.1364 0.1818
6.4×10^2	1.3×10^2	0.50	0.1364 0.1818 0.2727
1.0×10^3	3.4×10^2	0.50	0.1364 0.1818 0.2727
2.5×10^3	1.0×10^3	0.50	0.1364 0.1818 0.2727
5.5×10^3	2.6×10^3	0.50	0.1364 0.1818 0.2727
1.0×10^4	6.0×10^3	0.50	0.1818 0.2727
1.8×10^4	2.0×10^4	0.50	0.2727
----	5.0×10^4	0.50	0.3636
2.0×10^2	9.0×10^2	0.25	0.2182
----	9.0×10^2	0.50	0.2182
----	9.0×10^2	0.91	0.2182

Table 2 Computational Matrix for Cases with Uniform Heat Flux Boundary Condition.

Unobstructed Channel	**Obstructed Channel (r = 0.091)**		
Ra′	**Ra**	**L_1**	**AR**
5.0×10^2	2.3×10^3	0.50	0.2182

2.3 Computational Results

For the analysis of the vertical parallel-plate channels with no obstruction outlined in the previous sections, a non-uniform mesh of 17 x 8 quadrilateral elements was employed. Since the flow is symmetrical, only half of the channel was considered for the sake of computational efficiency. As shown in Fig. 5a, the elements were concentrated near the wall boundaries in anticipation of the large velocity and temperature gradients that were expected to occur in these regions at higher values of Ra. For the analysis of the obstructed vertical parallel-plate channels outlined in the previous section, a non-uniform mesh of 190 quadrilateral elements was employed. As shown in Fig. 5b, the elements were concentrated near the obstruction boundaries. Since the primary interest of the numerical study was to determine the steady state flow field, the computations were made using the iterative solution procedures provided in NACHOS. When using these procedures, convergence is defined to have been obtained when the maximum change in temperature is less than 0.5%. As required by the NACHOS code, the calculations were actually performed in terms of the physical variables.

All calculations were performed on the IBM 3081 machine located in Stokely Management Center, The University of Tennessee, Knoxville. The following results were obtained for each case:

(1) The heat flux distributions on the channel walls,

(2) the values of the stream function values at each node in the flow field (obtained from the velocity solution),

(3) contour plots of temperature and streamlines for the flow field, and

(4) velocity and temperature profile plots for the flow field.

The local heat transfer coefficients and the dimensionless flow rates were calculated from the numerical results. The local heat transfer coefficient for the UWT boundary condition is based on the temperature difference between the wall and the surrounding, that is

$$(h_x)_i = \frac{-K}{(T_w - T_\infty)} \left(\frac{\partial T}{\partial y}\right)_i, \quad i = 1,2 \ .$$

Then, the average heat transfer coefficient may be defined as:

$$(\bar{h}_i) = \frac{1}{L_i} \int_0^{\ell} (h_x \, dx)_i \ .$$

An average Nusselt number is defined using the average heat transfer coefficient, that is:

$$(\overline{N}u)_i \equiv \frac{\bar{h}_i b}{K}$$

where the subscript i denotes one of the two vertical walls.

The dimensionless volumetric flow rate in the channel is given by

$$M = \int_0^1 u \, dy \ .$$

In order to verify the results of the NACHOS code and the accuracy of the numerical procedure, the numerical solutions for the constant wall temperature unobstructed channel were compared with those of other investigators, as shown below. The numerical and experimental results for other cases will be discussed in Ch. 4 where they are compared with the experimental results.

2.3.1 Discussion of the numerical results for an unobtructed channel

Typical local heat transfer coefficients and average Nusselt number (Nu) calculations were carried out for $2 \times 10^2 \leq Ra \leq 10^4$. In Figure 6, Nu is plotted against Ra for Pr = 0.72; and a comparison is made between the numerical results of this investigation, the numerical work of Bodoia and Osterle [10], the experimental work of Elenbass [26] and the present experimental work (which is described in Ch. 3). The comparisons show excellent agreement (within an average of 3% difference).

Shown in Figures 7-21 are streamline, isotherm, temperature profiles and velocity profiles plots for four representative values of Ra which are typical of the results in the literature. As can be seen from the isotherm and streamline plots (Figures 7-10); the channel walls become thermally independent of one another as the aspect ratio (b/L) increases.

Figures 11-14 show the dimensionless temperature distribution at the mid-height and exit planes of the channel. In all cases, the minimum temperatures are on the center line. The maximum dimensionless temperature on the center line at the exit plane decreases as the Rayleigh number increases, as shown in Figure 15. This is because as the Rayleigh number increases the thickness of the thermal boundary layer decreases. In the limiting case of a very large Rayleigh number, the flow on each wall of the channel approaches that for free convection from an isolated, isothermal vertical plate immersed in a fluid of infinite extent. In this limit, a boundary layer is formed on each plate with the temperature on the center line between them remaining at the ambient temperature ($\theta = 0.0$)

Figures 16-19 show the velocity distribution at the inlet, mid-height and exit of the channel. When analyzing the free convective heat transfer between isothermal plates maintained at the same temperature, many authors [9-13] assumed a uniform inlet velocity profile. However, as shown in Figures 16-19, the velocity profile appears to be parabolic when the entrance velocity distribution is determined by applying the natural boundary condition. The effects of the inlet boundary conditions on numerical solutions for free convection in vertical channels is discussed by Miyatake, et al. [13] and Aihara [20]. Miyatake concluded that there is no significant effect on the calculated values of average Nusselt number when a uniform inlet velocity profile is assumed at the entrance. Aihara, however, states that it does have a significant effect. There is good agreement between the present numerical work and that of Bodoia and Osterle [10] (In which they assume a uniform inlet velocity profile at the entrance). This supports Miyatakes' conclusion, but still, there is a need for velocity measurements at the channel entrance.

The dimensionless volumetric flow rate (M) induced between the plates is shown as a function of $1/G_r$ in Figure 20. As shown in this figure, the dimensionless volumetric flow rate (M) increases with decreasing Grashof number (increasing $1/G_r$). A plot of the local Nusselt number (N_{ux}) against channel elevation for different values of Ra is shown in Figure 21. As expected, the local Nusselt number (N_{ux}) decreases with increasing channel elevation and increases with increasing Rayleigh number (Ra).

Table 3 summarizes some of the main computational results. As shown when the Rayleigh number increases, the mean Nusselt number (N_u) and the maximum dimensionless velocity (v_m) at the channel exit increase, and the center line temperature at the exit (θ_L) decrease. Also as the Rayleigh number (Ra) increases, the large induced vertical velocity causes an increase in the energy transport by convection. Also because of the large induced vertical velocity, the fluid does not remain long enough in the channel to be heated up to a temperature approaching the wall temperature.

Finally, the successful modeling of the unobstructed channel problem verified that the NACHOS code was properly implemented and hence can be used to model the obstructed channel problem.

Table 3. Summary of Computational Results For An Unobstructed Channel

Ra'	3.5×10^2	1.0×10^3	5.5×10^3	1.8×10^4
Nu	2.38	3.36	5.41	7.47
v_m	11.91	23.68	78.85	220
M	0.032	0.022	0.014	0.012
θ_L	0.517	0.217	0.010	0.000

CHAPTER III

THE EXPERIMENTAL INVESTIGATION

3.1 Introduction

Although very useful, the numerical approaches are inherently limited by problems originating from numerical diffusion, calculation instabilities, and the incorrect implementation of boundary conditions. Such deficiencies can be minimized by reference to experiments, which help to clarify the physics, and measurements of quantifiable accuracy and precision against which corresponding calculations may be compared.

Therefore, the objectives of the experimental investigation are: (1) to characterize qualitatively (through flow visualization) and quantitatively (through optical measurements) the structure of the natural convection flow field in air in a two-dimensional, isothermal channel with a single obstruction; and (2) to check by direct comparison with experimental measurements the accuracy of the numerical solutions.

3.2 Description of the Experimental Apparatus

The basic experimental apparatus consists of a two-dimensional channel with isothermal walls maintained at the same temperature. The geometry of the channel is shown in Figure 4. Since natural convection is extremely sensitive to disturbances in the environment, the channel is mounted in a test chamber which provides a controlled environment for the experiments. The apparatus can provide an arbitrary spacing between the test plates. Glass windows seal the two ends of the channel. One of the walls has a semi-cylindrical protrusion which serves as the obstruction in the channel. The isothermal walls are constructed from copper plates which are 2.75 inches high by 12.75 inches long and 0.5 inches thick. Copper was chosen because its high thermal conductivity assures an isothermal surface. The isothermal walls were made by milling a slot in a 0.25 inch thick copper plate. Another plate of the same thickness was then tightly soldered on the copper plate, which has drainage holes leading both to and from milled slot as shown in Figure 22. The spacing between the plates is set with the aid of a screw device. This allows the aspect ratio (width/height) of the channel to be changed. The length of the channel was taken to be fairly large relative to its height or width to minimize the magnitude of the end effects that disturb the flow from the original idealized assumption of two-dimensionality. Although the length of the walls is 12.75 in., the distance between the glass windows is 13.75 in. to allow space for gaskets. The walls were heated by circulating heated water from a Haake Model NK22 Constant-temperature Circulating Baths available in the laboratory. The circulatory water enters or leaves through copper tubes that extend from the backs of the walls. Insulated plastic hoses connect these tubes to the constant-temperature baths.

In order to measure the surface temperatures of the plates to check for uniformity of temperature, fifteen thermocouples were attached to each plate. The thermocouples were made from 36 gauge copper-constantan wire manufactured by the Omega Engineering Corporation. A number 55 drill bit (.052 inches) was used to drill from the back sides of the plates to within about .03 inches of the faces of the plates. The couples were held into the thermocouple holes by contact cement. The thermocouple wires extended through holes in the back sides of the plates and through the wall of the test chamber. Foam insulation was added at the back, top and two ends of the walls to reduce heat transfer and hence maintain a uniform surface temperature for each plate.

The test chamber (Figure 23) has internal dimensions of 12 in. x 12 in. in a horizontal plane and a height of 40 in. Plywood was used to construct the chamber. Two 9 in x 9 in. x 1/2 in. optically flat plate glass windows were mounted in opposite sides of the chamber. The windows allowed optical measurements and photographic studies to be performed. The vertical ends of the isothermal plates were firmly held against the windows to complete the channel geometry. One of the vertical plates was fixed while the other was movable horizontally to set the spacing between the two plates. The various spacings were obtained by inserting precisely machined metal rectangular spacers between the two plates. The spacers were made longer than the length of the plates to be able to hold them centrally between the two plates while a desired spacing was being established. Spacer thicknesses of .375, 0.50, 0.75 and 1 inch were employed.

3.3 Instrumentation and Data Acquisition System

The instruments used in this experimental study may be divided into two groups. The first group includes the instruments used to provide the qualitative data. Qualitative data were provided by making a Mach Zender Interferogram and performing flow visualization tests and recording the results. The Mach Zehnder Interferometer (MZI) tests provided the distributions of the isotherms; while the flow visualization tests provided the streamlines patterns. A general description of the MZI is given in Appendix B. A more detailed description of the MZI is given in reference [46]. The flow visualization tests are discussed in the following section. The second group included the instruments used to provide quantitative data. Quantitative data was obtained by performing Wollaston Prism Interferometer (WPI) tests and by direct measurements of structural (plate and enclosure wall) temperatures and the laboratory air temperature. The WPI tests yielded the local and average heat fluxes. A general description of the WPI is given in Appendix C. More detailed descriptions of the WPI are given in references [51, 52].

A Hewlett-Packard (HP)9826 micro-computer was used in conjunction with an HP 3497-A Data Acquisition system to read all thermocouple voltages. The laboratory air temperature (outside the test chamber) was measured with an accurate mercury-in-glass thermometer. This measurement was made to ensure that the air in the test chamber (enclosure) was in equilibrium with its surroundings.

3.4 Flow Visualization

In order to observe flow patterns smoke was injected into the air in the test section using a smoke generator. A schematic diagram of the smoke generator is shown in Fig. 24. A flat narrow sheet of light was used to illuminate the smoke particles against a dark background The flat narrow sheet of light was produced by means of the optical configuration shown in Fig. 25. A 15 mW helium-neon laser was used as a light source. The laser beam was passed through a small (3/16 inch) diameter glass rod, positioned in front of the laser, which produced the flat narrow sheet of light in a plane perpendicular to the test surface.

After smoke injection, the flow was allowed to reach steady state conditions before observations were made. The observations of the flow patterns were done both visually and by recording them using a Sony video cassette recorder.

3.5 Descriptions of the Experiments Performed

3.5.1 The unobstructed vertical channel

In order to establish the validity of the data obtained with the Wollaston Prism Interferometer (WPI), a validation test was performed with a channel that had vertical isothermal walls maintained at the same temperature. A view of the two isothermal plates is shown in Figure 26. The plates were 2.75 inches high and 12.75 inches long. The plates were constructed out of aluminum and heated by circulating hot water from a constant temperature circulating bath. Thermocouples were imbedded in the walls to determine the surface temperature on the free convection side. For a wall temperature of 130°F, horizontal variations in the temperature were maintained to within $\pm$ .2°F and vertical temperature variations to within $\pm$ 0.5°F. The room temperature was 77°F. The plates were 1 inch apart.

The Wollaston Prism Interferometer pattern for this test was recorded photographically and the fringe deflections at each wall were measured from the interferogram using a microscope. These fringe deflections were converted into heat fluxes. The procedures for reading the interferograms and calculating the heat fluxes are described in Appendix C. Experimental heat transfer coefficients obtained from this test are shown in Figure 27 for comparison with numerical data obtained for the same test case using NACHOS. The agreement is within an average of 10 percent. The average

Nusselt number for this test is plotted as a single point in Figure 5. The results compared favorably with those of Elenbass [23], as shown in Figure 6.

3.5.2 The obstructed vertical channel

Having established the validity of the experimental apparatus and procedures, the actual experiments of interest were carried out. The experiments were performed with an obstructed channel that had vertical isothermal walls and an isothermal, semi-cylindrical obstruction; all of which were maintained at the same temperature. A side view of the channel is shown in Figure 4. The experiments were performed for an obstructed vertical channel of length $L = 2.75$ inches, $L_1/L = 0.5$, $r = 0.091$, with $(T_w - T_\infty) = 53$ R and for values of Rayleigh number (Ra) that range from 10^2 to 10^4. The Rayleigh number and the aspect ratio were varied by changing the spacing between the two parallel vertical plates. For each experiment, the following steps were performed:

(1) An interferogram was made with the Wollaston Prism Interferometer (WPI). The local and average heat transfer coefficients were determined by reading this interferogram, which was reduced in the same manner as described in Appendix C. The interferograms were recorded photographically and a reproduction of one of them is shown in Figure 28.

(2) A flow visualization test was performed and the results were recorded as described above in section 3.4.

(3) Structural (plate and enclosure wall) temperatures and air temperatures in the enclosure and the laboratory, were recorded.

(4) A Mach-Zehnder Interferometer (MZI) interferogram was made with the Mach-Zehnder Interferometer in the infinite fringe setting to produce a fringe pattern that represented the isotherms. A reporduction of one of these interferograms is shown in Figure 29.

(5) A Mach-Zehnder Interferometer (MZI) interferogram was made with the Mach-Zehnder Interferometer in the wedge fringe setting. Each interferogram was recorded photographically and a reproduction of one is shown in Figure 30. The temperature distribution in the channel was determined from the interferogram. The procedure for reducing these interferograms is described in Appendix B.

The experimental results will be presented and discussed along with the numerical results in Chapter 4. An uncertainty analysis was performed on the experimental data. Details of this analysis are presented in Appendix D.

CHAPTER IV

RESULTS AND DISCUSSION

Results are obtained from the numerical solution for air for both the condition of uniform wall temperature and uniform wall heat flux for all the cases described in section 2.2. Also results are obtained from the experimental data for air for the condition of uniform wall temperature for the cases described in section 3.5.2. The solution for these conditions with different cases are discussed individually in the following sections (4.1, 4.2).

4.1 Uniform Wall Temperature

The numerical and experimental results for the unobstructed channel ($r = 0$) with constant wall temperature boundary condition were presented and discussed in section 2.3.1.

For the obstructed vertical channel with isothermal walls, solutions are obtained for the local Nusselt numbers (Nu_x). Figures 31-34 show comparison of local Nusselt numbers from the numerical solutions with those obtained from the experimental data using the Wollaston Prism Interferometer. Good agreement between the theoretical and experimental results may be noted, except near the entrance to the channel ($x/L \leq 0.1$).

At lower values of the Rayleigh number (Ra), the effect of the obstruction on the heat transfer from the unobstructed wall is shown by the curve of local Nusselt number (Nu_x) along that wall. As can be seen from Figures 31, 32 at a point along the wall, the local Nusselt number (Nu_x) increases with distance up the wall and then decreases. The same trend can also be observed for the obstructed wall curves for all Rayleigh number (Ra).

The lowest values of local Nusselt number (Nu_x) are obtained at the two intersections between the obstruction and the wall. As the velocity of the flow increases in the vicinity of the obstruction, the heat transfer coefficient increases to a maximum value then decreases further up the channel where the velocity decreases.

An average Nusselt number (Nu) for the obstructed channel is defined, using the net heat transfer, (see Appendix E) as:

$$\overline{N}u = \frac{\overline{N}u_1 \ell_1 + \overline{N}u_2 \ell_2}{\ell_1 + \ell_2}$$

where Nu_1, L_1 and Nu_2, L_2 are the average Nusselt number (Nu) and the length of the obstructed and unobstructed walls, respectively.

The average Nusselt numbers (Nu) from the numerical solution as well as those obtained from the experimental data are plotted against the Rayleigh number (Ra) (on a log-log plot) for different aspect ratio (AR) as shown in Figure 35. The comparison between the numerical results and the measurements are seen to agree within a 5% average, with a maximum deviation of 6.25%. There are no experimental data points at lower Rayleigh numbers (Ra). To obtain lower Rayleigh numbers (Ra) either the temperature difference (ΔT) or the distance between the two vertical plates should be decreased. Small temperature differences will result in very small fringe shifts which will be difficult to measure; and because of the obstruction size, the distance between the plates can be decreased to a certain value. Hence, because of these two constraints experimental data points were not taken at lower Rayleigh numbers (Ra).

From the non-dimensional governing equations and boundary conditions, it can be seen that the non-dimensional parameters are the

Rayleigh number (Ra), the aspect ratio, the obstruction size (r) and the obstruction location (L_1). For a constant r and L_1, the average Nusselt number (Nu) will be a function of Rayleigh number (Ra) and aspect ration (AR). From Figure 35, it can be noted that as Rayleigh number increases the the effect of the aspect ratio (AR) decreases. This observation can also be drawn from the non-dimensional form of the governing equations by noticing that the aspect ratio term multiplies the terms which can reasonably be expected to be relatively small, such as the term in the energy equation representing conduction in the streamwise (x) direction. As Rayleigh number (Ra) decreases the effect of the aspect ratio increases. This is to be expected, since for the lower Rayleigh numbers the flow approaches fully developed channel flow.

Since one of the primary objectives of this research is to study the effect of obstructions on natural convection flows in vertical channels, the average Nusselt numbers (Nu) from the numerical solution for both unobstructed and obstructed channels are plotted in Figure 36 against the Rayleigh number (Ra′), which is defined as (Ra)(AR). The curve for the unobstructed channel shown in Figure 36 is taken from the study of Churchill and Usagi [8]. This curve represents the three flow regimes (fully developed, transition and isolated vertical flat plates) for the unobstructed channel; while the ones for the obstructed channel represent only two flow regimes (transition and isolated vertical plates). A comparison of these curves shows that there is a significant reduction in the Nusselt number due to the presence of the obstruction, in the transition flow regime for the obstructed channel. It ranges from about 5% at a Rayleigh number of 10^4 to about 40% at a Rayleigh number of 10. This is caused by the reduction of flow area due to the presence of the obstruction. Although the reduction in the cross-sectional area of the channel increased the velocity of the flow around the tip of the obstruction and thereby increased the local heat transfer rate in that area; this does not compensate for the reduced flow rate due to area reduction. The regions of recirculating flow which are formed above and below the obstruction also affect the heat transfer, since the heat is transferred across the recirculating regions by conduction only. The region of recirculating flow above the obstruction is larger as shown by the computed streamline plots. The regions of recirculating flow at the bottom of the obstruction is usually quite small and they are detected in the numerical results by examining the streamline values at those nodes. The experimental observations of these recirculating flow regions show a similar trend as observed numerically.

The computed streamlines and isotherms are shown in Figures 37-40. From the streamline plots, it can be seen that the density of the streamlines increases in the region around the tip of the obstruction, due to the reduction of the channel cross-sectional area. Hence, the flow speeds up in this region. From the isotherm plots, it can be seen that, in the case of a very large Rayleigh number, a boundary layer is formed on each plate. Figures 41-42 show reproduction of the Mach-Zehnder Interferometric ("infinite fringe setting") pattern taken in the vicinity of the mid-length of the obstructed channel. In this setting, the light and dark fringe lines map out constant temperature lines (isotherms). Physical observations of streamlines through flow visualization, and of isotherms through interferograms (in the infinite fringe setting) show a good qualitative agreement with the numerical results.

The computed temperature profiles from the numerical solution at $x/L = .5$ and $x/L = 1$ are indicated in Figures 43-46. As can be seen from these Figures as the Rayleigh number increases the minimum temperature at these two planes ($x/L = .5$ and $x/L = 1$) decreases.

The computed velocity profiles from the numerical solution at $x/L = 0$, $x/L = .5$ and $s/L = 1$ are indicated in Figures 47-50. As can be seen from these Figures that the entrance velocity profile appears to be parabolic when the entrance velocity distribution is determined by applying the natural boundary condition. The maximum velocity occurs at mid-plane ($x/L = 0.5$) due to the reduction of the channel cross-sectional area. As the Rayleigh number increases the maximum velocity in the channel increases.

Figure 51 shows a comparison between temperature profiles obtained numerically and experimentally. The comparison between the measurements and the numerical results show a reasonably good agreement.

Finally, in summary, although due to the presence of obstruction in the channel, the flow velocity increased near the obstruction and the surface area on obstructed wall increased (both of them should increase the heat transfer rate); but the average Nusselt number decreased compared to the unobstructed channel. This is due to the reduction of mass flow rate and the existence of the regions of recirculating flow caused by the presence of the obstruction in the channel.

For the obstructed vertical channel with isothermal walls ($r = 0.091$) and $L_1/L = 0.25, 0.5$ and 0.91, the numerical solutions were obtained for the local and average Nusselt numbers and the mass flow rates. These values are compared with each other to examine the effect of moving the obstruction location along the wall on heat transfer rates. The comparison is shown in Figures 52, 53.

As can be seen in Figures 52, 53, for the obstructed channel, as the value of L_1/L increases (obstruction is moved away from the channel entrance) both the average Nusselt number and the mass flow rate decrease. As expected both of these values are less than those obtained for the unobstructed channel. The question which arises is: "Why should the Nusselt number decrease as L_1/L increases?"

In an attempt to find a reasonable answer, the local Nusselt number (Nu_x) along the obstructed walls is plotted in Figure 54, and the isotherms are shown in Figure 55 for $L_1/L = 0.25, 0.5$ and 0.91. As can be seen from Figure 54, the maximum value of the local Nusselt number (Nu_x) near the obstruction decreases as L_1/L increases. From Figure 55, it can be noted that as L_1/L increases, the temperature at the channel exit plane increases. Also from Figure 55, it can be noted that as L_1/L decreases, the boundary layer thickness at the channel entrance decreases and hence the temperature gradient at the wall increases as L_1/L decreases. Therefore, the Nusselt number, which is a function of temperature gradient, increases as L_1/L decreases.

4.2 Uniform Wall Heat Flux

For the vertical channel with uniform heat flux walls, solutions are obtained for heat flux values of 4.1472 Btu/hr ft^2. Computed temperature distributions along the walls are shown in Figure 56. The maximum temperature along the two walls of the unobstructed channel occurs at the corner at the top of the obstruction. This is expected due to the region of recirculating flow at that location. The magnitude of the maximum wall temperature in the obstructed channel however is only about 4% greater than the magnitude of the maximum temperature on the obstructed ?? channel. This is not a significant difference.

CHAPTER V

CONCLUSIONS AND RECOMMENDATIONS

Natural convective heat transfer in parallel plate vertical channels in air, with and without an internal obstruction, has been studied numerically and experimentally for a Prandtl number of 0.72 and over a range of Rayleigh numbers from 10^2 to 10^4. Two thermal conditions of the parallel walls are considered: uniform wall temperature (UWT) and uniform heat flux (UHF).

The results for the unobstructed channel with UWT boundary condition show that as the Rayleigh number increases, the Nusselt number, the mass flow rate and the maximum velocity at the exit all increase. However, with increasing Rayleigh number the exit center line temperature decreases. Also as the rayleigh number increases; the large induced vertical velocity causes an increase in the energy transport by convection. Also because of the large induced vertical velocity, the fluid does not remain long enough in the channel to be heated up to a temperature approaching the wall temperature. In all these cases, the minimum temperatures are on the center line. In the limiting case of a very large Rayleigh number, the flow on each wall approaches that of free convection from an isolated heated vertical plate. A boundary layer is formed on each plate with the temperature on the center line between them remaining at the ambient temperature ($\theta = 0.0$).

The local value of the Nusselt number decreases as the fluid flows up the channel, being a minimum at the top. The present solutions give the average Nusselt number which describes the heat transfer to the fluid. The average Nusselt number is found to be related to the Rayleigh number by a universal curve for all wall temperature, providing the wall temperature difference (above the temperature of the fluid at the channel entrance) is used to define these parameters. The slope of this line is 0.250 and the intercept is 0.671.

A comparison is made (on a log-log plot) between these present results and those reported in the literature by other authors. The comparison show a good agreement. This good agreement verified that NACHOS code was properly implemented and can be used with the case of obstructed channels.

The results for the obstructed channel with UWT boundary condition and with $L_1 = 0.5$ showed that as the Rayleigh number increases, the Nusselt number, the quantity of flow and the maximum velocity increases. However, with increasing Rayleigh number the minimum temperature at the exit decreases. This is for the same reason discussed above for the case of unobstructed channel. The present solutions give the local and the average Nusselt number for each wall. It is found that the average Nusselt number for the obstructed wall is less than the one for the unobstructed wall. The local value of Nusselt number decreases as the fluid flows up the obstructed wall until it reaches the bottom corner of the obstruction ($L_1 = 0.41$); and then it increases as the fluid flows around the bottom half of the obstruction and it decreases again along the top half of the obstruction where it reaches its minimum value at the corner at the top of the obstruction ($L_1 = 0.59$), and from here on it starts to increase again up to the exit. For values of Rayleigh numbers less than 3×10^3 the local value of Nusselt number decreases as the fluid flows up the unobstructed wall to a point where the vertical velocity starts to increase, because of the reduction in channel cross-sectional area due to the presence of the obstruction, and hence the local Nusselt number increases for some distance and then decreases again, being a minimum at the exit. The comparison between the measurements and the numerical results show a reasonably good agreement. The present solutions also give the average Nusselt number for the obstructed channel. The plot of the Nusselt number versus Rayleigh number for different aspect ratios (on a log-log plot) is shown in Figure 36. It is noted that for $Ra > 10^3$ the effect of the aspect ratio is small, while it is significant for $Ra < 10^3$.

Comparison of the average Nusselt number for the obstructed channel with the corresponding ones for an unobstructed channel shows a reduction in heat transfer for the obstructed channel which range from 5% at Rayleigh number of 10^4 to 40% at Rayleigh number of 10.

The effect of varying the location of the obstruction on the natural convection heat transfer in parallel plate vertical channels in air has also been investigated in this study numerically. Only the isothermal thermal condition of the channel walls is considered. Numerical solutions give the local and the average Nusselt numbers. It is found that moving the location of the obstruction along the wall from the leading edge to the exit causes a reduction in the heat transfer rate in the channel. Moving the obstruction from the location $L_1/L = 0.25$ to $L_1/L = 0.5$ resulted in about a 16% reduction in the magnitude of the average Nusselt number.

For the vertical channel whose walls are heated uniformly, the presence of the obstruction increased the magnitude of the maximum temperature by 4%; and that maximum temperature occurred at the corner at the top of the obstruction and not at the exit as the case for unobstructed channels.

Finally, virtually nothing was previously known about the detailed nature of obstructed natural convection flows in channels. Based on the present investigation, however, we can conclude that the presence of an obstruction and its location have significant effects on natural convection flows in vertical channels. This is an open-end research area. Hopefully, the present study will serve to whet the appetite of other investigators to get involved in this area of research. The effect of different obstruction geometries and locations with different thermal boundary conditions need to be investigated experimentally as well as numerically. Multiple obstructions, as well as obstructions on both walls need to be investigated.

REFERENCES

REFERENCES

1. Aung, W., Yener, Y., "Research Directions in Natural Convection," Natural Convection - Fundamentals and Applications, S. Kakac, W. Aung, R. Viskanta, eds., Hemisphere Publishing Corporation, Washington, D.C., (1985).

2. Aung, W., In Proceedings of a Workshop on Natural Convection, K. T. Yang, J. R. Lloyd, eds., July, (1982), Beaver Run, Breckenridge, Colorado.

3. Jaluria, Y., Natural Convection Heat and Mass Transfer, Pergamon Press, (1980).

4. Bejan, A., Convection Heat Transfer, J. Wiley and Sons, New York, (1984).

5. Kakac, S. Aung, W. Viskanta, R., Natural Convection - Fundamentals and Applications, Hemisphere Publishing Corporation, Washington, D.C. (1985).

6. Aung, W., Chimah, B., "Laminar Heat Exchange in Vertical Channels - Applications to Cooling of Electronic Systems," in Low Reynold Number Flow Heat Exchange, S. Kakac, R.K. Shah, A.E. Bergles, eds., Hemisphere Publishing Corporation, Washington, D.C., (1983), pp.395-413.

7. Jaluria, Y., "Natural Convective Cooling of Electronic Equipment," in Natural Convection, Fundamentals and Applications. Hemisphere Publishing Corporation, Washington, D.C., (1985), pp. 961-981.

8. Kraus, A.D., Bar-Cohen, A. Thermal Analysis and Control Of Electronic Equipment, McGraw-Hill, (1983).

9. Engel, R. K., Mueller, W. K., "An Analytical Investigation of Natural Convection in Vertical Channels," ASME Paper No. 67-HT-16, Presented at the ASM-AIChE Heat Transfer Conference, Seattle, WA, August 6-8, (1967).

10. Bodoia, J. R., Osterle, J. F., "The Development of Free Convection Between Heated Vertical Plates," ASME J. Heat Transfer, Vol. 84, pp. 40-44, (1961).

11. Aung, W., Fletcher, L. S., Sernas, V., "Developing Laminar Free Convection Between Vertical Flat Plates With Asymmetric Heating," International J. of Heat and Mass Transfer, Vol. 15, pp. 2293 - 2308, (1972).

12. Miyatake, O., Fujii, T., Fujii, M., Tanaka, H., "Natural Convective Heat Transfer Between Vertical Parallel Plates - One Plate With A Uniform Heat Flux and the Other Thermally Insulated," Heat Transfer Jpn. Res., Vol. 4, pp. 25-33, (1973).

13. Miyatake, O., Fujii, T., "Free Convective Heat Transfer Between Vertical Parallel Plates - One Plate Isothermally Heated and The Other Thermally Insulated," Heat Transfer Jpn. Res., Vol. 3, pp. 30-38, (1972).

14. Aung, W., Beitin, K. E., Kessler, J. J., "Natural Convection Cooling Of Electronic Cabinets Containing Arrays of Vertical Circuit Cards," ASME Paper No. 72-WA/HT-40, Presented at the ASME Winter Annual Meeting, New York, N. Y., Nov. 26-30, (1972).

15. Coyne, J. C. "An Analysis of Circuit Board Temperatures in Electronic Equipment Frames Cooled By Natural Convection, " Fundamentals of Natural Convection/Electronic Equipment Cooling, L. C. Witte, L. S. Saxena, eds., ASME Publication No. HTD-Vol. 32, pp. 59-65.

16. Kettleborough, C. F., "Transient Laminar Free Convection Between Heated Vertical Plates Including Entrance Effects," Int. J. Heat and Mass Transfer, Vol. 15, pp. 883-896, (1972).

17. Nakamura, H., Asako, Y., Naiton, T., "Heat Transfer By Free Convection Between Two Parallel Flat Plates," Numerical Heat Transfer, Vol. 5, pp. 95-106, (1982).

18. Burch, T., Rhodes, T., Acharya,S., "Laminar Natural Convection Between Finitely Conducting Vertical Plates," Int. J. Heat and Mass Transfer, Vol. 28, No. 6, pp. 1173-1186, (1985).

19. Carpenter, J. R., Briggs, D. G., Sernas, V., "Combined Radiation and Developing Laminar Free Convection Between Vertical Flat Plates With Asymmetric Heating," J. Heat Transfer, pp. 95-98, February, (1976).

20. Aihara, T., "Effects of Inlet Boundary-Conditions on Numerical Solutions of Free Convection Between Vertical Parallel Plates," Rep. Inst. High Speed Mech., Vol. 28 , pp. 1-27, (1973).

21. Karki, K. C., Patankar, S. V., "Cooling of a Vertical Shrouded Fin Array By Natural Convection: A Numerical Study, "Fundamentals of Natural Convection/Electronic Equipment Cooling, L. C. Witte, L. S. Saxena, eds., ASME Publication No. HTD-Vol. 32, pp. 33-40.

22. Ramakrishna, Rubin, Khosla, "Laminar Natural Convection Along Vertical Square Ducts," Numerical Heat Transfer, Vol. 5, pp. 59-79, (1982).

23. Davis, L. P., Perona, J. J., "Development of Free Convection Flow In a Heated Vertical Open Tube," Int. J. Heat Mass Transfer, Vol. 14, pp. 889-903, (1971).

24. Kageyama, R. Izumi, M., "Natural Heat Convection In A Vertical Circular Tube," Bulletin JSME, Vol. 13, pp. 382-394, (1970).

25. Dyer, J. R., "The Development of Natural Convection Flow In A Vertical Uniform Heat Flux Duct," Int. J. Heat Mass Transfer, Vol. 18, pp. 1455-1465, (1975).

26. Elenbass, W., "Heat Dissipation of Parallel Plates by Free Convection," Physica, pp. 1-28, (1942).

27. Sernas, V., Fletcher, L., Aung, W., "Heat Transfer Measurements With A Wollaston Prism Schlieren Interferometer," ASME Paper No. 72-HT-9, Presented at the AIChE-ASME Heat Transfer Conference, Denver, Colorado, August 6-9, (1972).

28. Sparrow, E. M., Bahrami, P. A., "Experiments in Natural Convection From Vertical Parallel Plates With Either Open or Closed Edges," ASME J. Heat Transfer, Vol. 102, pp. 221-227, (1980).

29. Akbari, H. T., Borges, R., "Finite Convective Laminar Flow Within Trombe Wall Channel," Solar Energy, 22, pp. 165-174 (1979).

30. Tichy, J. A., "The Effect of Inlet and Exit Losses on Free Convective Laminar Flow in The Trombe Wall Channel," ASME, Paper No. 82-WA / Sol-10, (1982).

31. Levy, E. K., Eichen, P. A., Cintani, W. R., Shaw, R. R., "Optimum Plate Spacings for Laminar Natural Convection Heat Transfer From Parallel Vertical Isothermal Flat Plates: Experimental Verification, "ASME J. Heat Transfer, Vol. 97, pp. 474-476, (1975).

32. Churchill, S. W., "A Comprehensive Correlating Equation for Buoyancy-Induced Flow in Channels," Letters in Heat and Mass Transfer, Vol. 4, pp. 193-199, (1977).

33. Sparrow, E. M., Prakash, C., "Enhancement of Natural Convection Heat Transfer By A Staggered Array of Discrete Vertical Plates," ASME J. Heat Transfer, Vol. 102, pp. 215-220, (1980).

34. Prakash, C., Sparrow, E. M., "Performance Evaluation for Discrete (In-Line or Staggered) and Continuous-Plate Arrays," Numerical Heat Transfer, Vol. 3, pp. 89-106, (1980).

35. deBoer, P. C. T., "Thermally Driven Motion of Strongly Heated Fluids," Int. J. Heat Mass Transfer, Vol. 27, No. 12, pp. 2239-2251, (1984).

36. Richtmyer, R. D., Morton, K. W., Difference Methods for Initial-Value Problems, John Wiley & Sons, New York, (1967).

37. Mitchell, A. R., Griffiths, D. F., The Finite Difference Method in Partial Differential Equations, John Wiley & Sons, New York, (1980).

38. Peyret, R., Taylor, T. D., Computational Methods for Fluid Flow, Springer-Verlag, New York, (1983).

39. Baker, A. J., Finite Element Computational Fluid Mechanics, McGraw-Hill, New York, (1983).

40. Zienkiewicz, O.C., The Finite Element Method, McGraw-Hill, New York, (1977).

41. Huebner, K. H., The Finite Element Method for Engineers, John Wiley & Sons, New York, (1975).

42. Denny, V. E., Clever, R. M., "Comparisons of Galerkin and Finite Difference Methods for Solving Highly Nonlinear Thermally Driven Flows," J. Comp. Physics, Vol. 16, pp. 271-284, (1974).

43. Beach, T., "NACHOS - Manual for University of Tennessee Users," Technical Rpt. No. MAE-NCL-12, University of Tennessee, Knoxville, TN, February (1985).

44. Gartling, D. K., "NACHOS - A Finite Element Computer Program for Incompressible Flow Problems, Part I - Theoretical Background," SAND 77-1333, Sandia Laboratories, Albuquerque, NM, (197~~8~~7).

45. Gartling, D. K., "NACHOS - A Finite Element Computer Program for Incompressible Flow Problems, Part II - User's Manual," SAND 77-1334, Sandia Laboratories, Albuquerque, NM, (197~~8~~7).

46. Jessee, J. W., "The Development of a Natural Convection Heat Transfer Research Facility," M.S. Thesis, University of Tennessee, Knoxville, TN, August (1985).

47. Eckert, R. G., Goldstein, R. J., Measurements in Heat Transfer, Hemisphere Publishing Corporation, Washington, D.C., (1976).

48. Hauf, W., Grigull, U., "Optical Methods in Heat Transfer," Advances in Heat Transfer, J. P. Hartnett, T. F. Irvine, eds., Vol. 6, pp. 133-366, (1970).

49. Merzkirch, W., Flow Visualization, Academic Press, New York, (1974).

50. Heidari, M. Y., Parsons, J. R., "The UTK Dept. of Mechanical Engineering and Aerospace Engineering Wollaston Prism Interferometer," Rpt. No. MAE NCL-2, University of Tennessee. Dec 1980

51. Irby, R. G. A., and Parsons, J.R., "Examination of Natural Convection From Selected Downward-Facing Heated Surfaces with the Wollaston Prism Interferometer," Technical Rpt. No. MAE NCL-3, University of Tennessee, Knoxville, TN.

52. Sernas, V., "The Wollaston Prism Schlieren Interferometer," von Karman Institute for Fluid Dynamics Lecture Series 6, Advanced Measurements Techniques in Fluid Mechanics, March 7-11, (1977).

53. Kline, S. J., and McClintock, F. A., "Describing Uncertainties in Single-Sample Experiments," Mechanical Engineering, p. 3, January, (1953).

APPENDICES

APPENDIX A

FINITE ELEMENT SOLUTION ALGORITHM USED BY THE NACHOS CODE

A-1 Formulation of the F.E. Equations

The finite element algorithm for convective energy transport in terms of the method of weighted residuals (MWR) deals directly with the governing differential equations and their boundary conditions, which may be written in general as $L(q) = 0$ and $\ell(q) = 0$, respectively. First, an approximate solution, say, q^h, is hypothesized to exist. Then, upon direct substitution, $L(q^h)$ and $\ell(q^h)$ are measures of the error in the solution approximation. For more details, see references [39] and [44].

The derivation of the finite element equations begins with the division of the continuum region of interest into a number of simply-shaped regions called "finite elements." Each element includes a set of nodal points at which the finite element approximations for the dependent variables (q_e^e) are evaluated.

Hence, the semi-discrete approximation $q_e^h(x_i)$ to the solution $q_e(x_i)$ is defined as

$$q_e(x_i) = q_e^h(x_i) \equiv \sum_{e=1}^{M} q_e^e(x_i)$$

where q_e^e is defined in terms of the cardinal basis as

$$q_e^e(x_i) \equiv \left[N_k(x_i)\right]^T [Q]_e \quad .$$

The elements of $[Q]_e$ are the nodal values of $q_e(x_i)$. N_k is the cardinal basis and k is the degree of the basis.

The finite element algorithm concept, as defined within the MWR, requires the approximate error in $L(q_e^h)$ and $l(q_e^h)$ to be orthogonal to the basis $[N_k]$. Combining these linearly independent constraints, and using a multiplier λ (an arbitrary constant), the finite element solution algorithm for the governing equations and associated boundary conditions can be shown to be given by:

$$\int_{R^2} [N_k] L(q_e^h)\, d\tau \; + \; \lambda \int_{\partial R} [N_k] \ell(q_e^h)\, d\sigma \;\equiv\; [0] \qquad \text{(A-1)}$$

Independent of the degree k of the basis $[N_k]$, equation (A-1) represents a system of ordinary differential (and algebraic) equations written on the unknown $q_e^h(x_i)$ of the form

$$[F(Q)] = \{u + K\}[Q] + [b] = [0] \qquad \text{(A-2)}$$

The differential equations describing the 2-D natural convection flow in obstructed channels can be written in tensor notation as follows:

$$\textit{Conservation of mass} \qquad \frac{\partial u_i}{\partial x_i} = 0 \qquad \text{(A-3a)}$$

$$\textit{Conservation of momentum} \qquad \rho \frac{Du_i}{Dt} + \frac{\partial \tau_{ij}}{\partial x_j} + \rho g_i \qquad \text{(A-3b)}$$

$$\textit{Conservation of energy} \qquad \rho c \frac{DT}{Dt} = -\frac{\partial q_i}{\partial x_i} \qquad \text{(A-3c)}$$

where the stress tensor is

$$\tau_{ij} = P\delta_{ij} + \mu\left(\frac{\partial u_i}{\partial x_j} + \frac{\partial u_j}{\partial x_i}\right)$$

and the heat flux vector is given by

$$q_i = -K \frac{\partial T}{\partial x_i} .$$

The equation of state may be written as

$$\rho = \rho_o \left[1 - \beta (T - T_\infty) \right] .$$

In the above equations, u_i is the velocity component in the x_i coordinate direction, t is the time, P is the pressure, T is the temperature, ρ is the density, τ_{ij} the stress tensor, q_i the heat flux vector, μ the viscosity, C_p the specific heat, k the thermal conductivity and β the coefficient of volume expansion. Also D/Dt is the substantial derivative and δ_{ij} the Kronecker delta.

Carrying out the general algorithm outline above, the dependent variables (u_i, P, T) can be expressed in the following form within each element

$$u_i(x_i,t) = \left[N_k(x_i) \right]^T U_i(t) \tag{A-4a}$$

$$P(x_i,t) = \left[N_k(x_i) \right]^T P(t) \tag{A-4b}$$

$$T(x_i,t) = \left[N_k(x_i) \right]^T T(t) . \tag{A-4c}$$

In eqns. (A-4) the u_i, P, and T are vectors of unknown nodal point variables and the N_k are vectors of interpolation, or basis, functions. k is the degree of the basis (k = 1 for linear basis and 2 for quadratic basis). Velocity components and temperature are approximated by quadratic basis functions within each element while the pressure is assumed to vary linearly. All dependent variables are forced to be continuous between elements. This continuity requirement is met through the appropriate summation of equations for nodes common to adjacent elements. The superscript T denotes a vector transpose and subscript i denotes the coordinate directions x and y.

Substituting the approximate forms u_i, P, and T into the field equations (A-3) yields a set of residuals (R_i), or error equations, as shown below.

Conservation of mass:

$$f_1(N_2, u_i) = R_1 \tag{A-5a}$$

Conservation of momentum:

$$f_2(N_2, N_1, N_2, u_i, P, T) = R_2 \tag{A-5b}$$

Conservation of energy:

$$f_3(N_2, N_2, T, u_i) = R_3 \tag{A-5c}$$

As discussed earlier, to use the MWR to reduce the residuals R_i to zero over each element; the residuals have to be orthogonal to the basis. That is,

$$< f_1, N_1 > = < R_1, N_1 > = 0 \tag{A-6a}$$

$$< f_2, N_2 > = < R_2, N_2 > = 0 \tag{A-6b}$$

$$< f_3, N_2 > = < R_3, N_2 > = 0 \tag{A-6c}$$

where <, > denotes the inner product defined by

$$< a, b > = \int_V a \quad b \; dV$$

with V being the volume of the element.

Carrying out the above integrals yields the set of coupled matrix equations shown below.

Momentum and Continuity:

$$Mu + [C(u)]\, V + [K]V = F(t) \qquad \text{(A-7)}$$

where $V^T = (u_1{}^T, u_2{}^T, p^T)$

$u^T = (u_1{}^T, u_2{}^T)$

Energy:

$$NT + [D(u)]\, T + [L]T = G \qquad \text{(A-8)}$$

Only the case of steady-state flows will be addressed in this study. For steady-state flows, ($T = u = 0$) and the matrix equations can, therefore, be reduced to

$$[C(u)]\, V + [K]V = F \qquad \text{(A-9)}$$

and,

$$[D(u)]\, T + [L]T = G. \qquad \text{(A-10)}$$

The matrix equations (A-9) and (A-10) represent the discrete analogs of the conservation equations for an individual finite element. The C and D matrices represent the convection of momentum and energy, respectively; while the K and L matrices represent the diffusion of momentum and energy. The F and G vectors provide the forcing functions for the system.

Once the matrix equations have been assembled, the task of solving this large set of strongly coupled, nonlinear equations still remains. The solution procedure will be discussed later.

A-2 Element Construction:

The element library in NACHOS consists of six-node isoparametric triangles and eight-node isoparametric quadrilaterals. For the present study the quadrilateral elements were selected. The quadratic basis, or interpolation, functions for the velocity components (u_i) and the temperature (T) for this element are given by the vectors,

$$N_2 = 1/2 \begin{Bmatrix} 1/2 \quad (1-s)(1-t)(-s-t-1) \\ 1/2 \quad (1+s)(1-t)(s-t-1) \\ 1/2 \quad (1+s)(1+t)(s-t-1) \\ 1/2 \quad (1-s)(1+t)(-s+t-1) \\ (1-s^2)(1-t) \\ (1+s)(1-t^2) \\ (1-s^2)(1+t) \\ (1-s)(1-t^2) \end{Bmatrix}$$

and the linear basis or interpolation functions for pressure for this element are given by the vector,

$$N_1 = 1/4 \left\{ \begin{array}{l} (1-s)(1-t) \\ (1+s)(1-t) \\ (1+s)(1+t) \\ (1-s)(1+t) \end{array} \right\}$$

A-3 Solution Procedure:

For steady-state NACHOS employs a solution algorithm that alternately solves equations (A-9) and (A-10) while continually updating the variable coefficient matrices to reflect the most recently computed values for the dependent variables. It consists of the following alternating procedure: The energy equation is advanced first using,

$$[D(u^n)]\,T^{n+1} + [L(T^n)]T^{n+1} = G(T^n)$$

Then, the momentum equation is advanced using,

$$[c(u^n)]\,V^{n+1} + [K(T^{n+1})]V^{n+1} = F(T^{n+1})$$

The solution algorithm will keep alternating between the energy and momentum equations, using updated values of temperature and velocity, as follows:

$$[D(u^{n+1})]\,T^{n+2} + [L(T^{n+1})]T^{n+2} = G(T^{n+1}) \tag{A-11}$$

.

.

.

etc

where the superscript n indicates the iteration number. The basic iteration scheme in equation (A-11) can often be accelerated by suitable choice of an interpolation procedure for the dependent variabes used to evaluate the coefficient matrices. For example, the [K] or [L] matrices can be evaluated at $T^{*(n+1)}$ using

$$T^{*(n+1)} = \alpha T^{n+1} + (1 - \alpha) T^{n} \qquad (0 < \alpha < 1)$$

NACHOS uses the above interpolation procedure for the temperature field with $\alpha = 1/2$. No interpolation on the velocity field is used.

APPENDIX B

GENERAL DESCRIPTION OF THE MACH-ZEHNDER INTERFEROMETER

In this appendix, a brief description of the Mach-Zehnder Interferometer (MZI) and the data reduction procedures for this instrument will be given. The Mach-Zehnder Interferometer (named after the two men who independently suggested its design) can be used for qualitative flow visualization as well as to obtain quantitative data over a flow field that is placed in one of the instruments light paths. The instrument is valuable for research on natural convection flows (as well as other flows) since it can measure the temperature distribution within a fluid and allow visualization of boundary layers and flow patterns. It is one of the most important optical instruments in the field of heat transfer.

The MZI's advantage over other types of interferometers is that the refraction errors are reduced [46]. Its disadvantages are that it is rather difficult to align and it requires a large number of high quality optical components. An Aerolab 6-inch MZI, located in the UTK Natural Convection Laboratory, was used for this investigation. The basic optical arrangement of the MZI is shown in Figure B1. For a more detailed descriptions of the MZI see references [46-49].

It was decided to begin the experiment by making some exposures with the MZI in the infinite fringe setting. In this setting, the light and dark fringe lines map out constant temperature lines (or isotherms). A reproduction of these isotherms are shown in Figure B2. The MZI was then set in the wedge fringe setting and a photograph of the interferogram was taken. In this setting, the displacement of a fringe from the isothermal (no flow) position is directly proportional to the change in temperature. All photographs were made with Polaroid Type 55 Positive - Negative film. For most exposures, the exposure time was approximately 1 to 2 seconds. All measurements or data values were obtained from the negatives (interferograms). Using the technique and theory described in reference [46], the data reduction technique will now be illustrated with the analysis of a typical interferogram. Measurements on the interferogram negatives were made using a measuring microscope (Nikon Shopscope). The measurements of the fringe number (s) and its location for a typical interferogram are shown in Table B1. The following relation was used to calculate the temperature (T) at any point in the flow field

$$T = \frac{T_w}{1 + aS_{ideal}}$$

where:

$$a = \frac{2\lambda R T_w}{3L\bar{r}p}$$

$$S_{ideal} = s + \Delta s_1 - \Delta s_2 = \textit{corrected fringe number}$$

$$\Delta s_1 = \frac{n\lambda L}{12(\bar{b})^2} = \textit{refraction error}$$

$$\Delta s_2 = 0.3698\, P \sqrt{\delta^2 - y^2} \left[\frac{1}{T_\infty} - \frac{1}{\sqrt{\Delta T T_\infty}}\, tan^{-1} \frac{\Delta T}{\sqrt{\Delta T T_\infty}} \right] = \textit{end effect error}$$

$$\bar{r} = \left(\frac{2}{3}\right)\left(\frac{(n-1)}{\rho}\right) = \textit{specific refractivity for air}$$

$$\rho = 1.13\left(\frac{kg}{m^3}\right) = \textit{density of air}$$

$$n = 1.000207 = \textit{refractive index for air}$$

$$\Delta T \equiv T_m - T_\infty$$

T_W = 54.4°C	=	wall temperature
P = 744.45 mmHg	=	air pressure
λ = 6328 x 10^{-10} m	=	wave length of laser light
R = 2.15297 m^3 mmHg/kg°k	=	ideal gas constant for air
L = 0.3256 m	=	plate length (in direction of optical path)
T_∞ = 25°C	=	ambient temperature

and

s	=	uncorrected fringe number
b	=	the fringe spacing (mm)
δ	=	the boundary layer thickness (mm)
T_m	=	the approximate, uncorrected value for air temperature at the s-value under consideration (°C)
y	=	the traverse distance from one of the walls to the point under consideration

Using the above listed values and the measurements shown in Table B1, the corrected fringe number and temperature data for this typical interferogram are shown in Table B2.

The uncertainty associated with an experimental value of temperature is 0.44°C (See Appendix D).

TABLE B1: Fringe Number and Uncorrected Temperature Data for the Interferogram at $x/L = 0.5$, $Ra = 5 \times 10^4$, AR = .3636

y(mm)	S	b(mm)	Uncorrected Temp. T, (°C)
6.385	0.		54.44
7.662	5.	1.528	38.84
9.450	8.5	2.469	28.38
12.413	9.5	2.939	25.63
17.367	9.5	2.757	25.63
17.926	9.5	1.947	25.63
19.211	9.	1.877	27.54
21.680	7.75	1.840	30.88
22.890	5.5	1.930	37.36
25.54	0.		54.44

TABLE B2: Fringe Number and Corrected Temperature Data for the Interferogram at $x/L = 0.5$, $Ra = 5 \times 10^4$, $AR = .3636$.

y/b	S	ΔS_1	ΔS_2	S_{ideal}	T(°C)	θ
0.250	0	0.000	0.000	0.000	54.40	1.000
0.300	5	0.007	0.092	4.915	39.09	0.479
0.370	8.5	0.003	0.011	8.490	28.68	0.115
0.486	9.5	0.002	0.000	9.502	25.88	0.021
0.680	9.5	0.002	0.000	9.502	25.88	0.021
0.702	9.5	0.005	0.000	9.502	25.88	0.021
0.752	9.0	0.005	0.020	8.985	27.43	0.083
0.850	7.75	0.005	0.040	7.715	30.977	0.203
0.896	5.5	0.005	0.120	5.385	37.70	0.431
1.000	0	0.000	0.000	0.000	54.44	1.000

APPENDIX C

WOLLASTON PRISM INTERFEROMETER

There has been increased emphasis on improving heat transfer measurements over the past few years, especially in the area of convective heat fluxes. This has led to a need for more refined experimental measurement techniques. As these experimental techniques have evolved, new and different instruments and applications have been developed, especially in the field of optical measurement systems. One class of optical devices, interferometers, have been found to be extremely useful for heat transfer studies, particularly when the insertion of an instrument into a fluid flow field would severly distort the measurements.

Several interferometric techniques have been devised in order to provide quantitative results. One of these techniques is the Wollaston Prism Schlieren interferometer (WPI), [27], [51], [52], which was used in this study. This technique of heat flux measurement utilizes a standard single pass schlieren optical system converted to an interferometer by replacement of the knife edge with two crossed polarizers and a Wollaston prism. The optical arrangement of the Wollaston prism interferometer (WPI) is shown in figure C1. When the two polarizers on each side of the prism are oriented at 45 degrees to the direction normal to the straight reference fringes, fringes are produced on the screen. The fringe shifts obtained with this technique are shown to be proportional to the temperature gradient within a two-dimensional test section [27]. The heat flux at any point on a heated wall is then obtained by multiplying the measured temperature gradient at the wall by the thermal conductivity of the fluid. This technique has the advantage of being relatively easy to use, and is suitable for measurement of moderate temperature gradients.

The WPI available in UTK Natural Convection Laboratory was custom-designed and built by Dr. J. R. Parsons and his students in the Department of Mechanical and Aerospace Engineering. The design is patterned after the devices built by Sernas at Rutgers University and by Flack at the University of Virginia.

To run the test, the WPI was set up and the laser beam collimated as described in Irby and Parsons [51]. The test section was then positioned in a 6 inch diameter schlieren beam in such a way that a large portion of the light is not disturbed by temperature gradients. This was done to provide straight reference fringes on the interferogram. The test section was allowed to reach steady-state. The Wollaston prism with the two polarizers was rotated as a unit until the straight reference fringes made an angle of anywhere between 30 and 60 degrees with the heated surfaces. The purpose of this rotation was to make the deflected fringes terminate at the wall. When the reference fringes are parallel to the wall, the fringe shifts in the heated channel were large, but very few fringes terminated at the wall. Thus, very few heat flux data points could be obtained from such an orientation.

Once this was accomplished, the interferometric pattern was recorded photographically by replacing the viewing screen with a polaroid camera. Measurements to determine the fringe deflections at each wall, fringe spacing, the magnification factor and the boundary layer thickness were made from the negative, using a Nikon Shopscope. The fringe deflections at each wall were then converted into heat transfer coefficients by the use of the following equation [51]:

$$h_{conv} = \left[\frac{\lambda}{K_{GD} Z_{eff} h} \right] \frac{RT_w^2}{p^2} \frac{k_w}{\sin\theta(T_w - T_\infty)} \frac{\Delta s}{s} \qquad \text{(C-1)}$$

where:

λ	=	wavelength of light
K_{GD}	=	Gladstone-Dale constant for air
Z_{eff}	=	the effective test section length along the light beam path
h	=	double image distance in test section
R	=	ideal gas constant for air
T	=	absolute temperature
p	=	atmospheric pressure
k	=	thermal conductivity of air
θ	=	angle between the direction normal to the straight reference fringe and the wall
Δs	=	fringe displacement
s	=	fringe spacing between straight reference fringes

Subscripts

w	indicates the conditions at the wall
∞	indicates the conditions at infinity

A sample interferogram is presented in Figure C2, with points representative of those used in the calculations indicated. Sample calculations are presented below.

T_w =	130°F	=	plate temperature
T_w =	77°F	=	ambient temperature
K_{GD} =	3.615×10^3 ft^3/lbm	=	Gladstone-Dale constant for air
λ =	6328×10^{-8}	=	wave length for Helium-Neon laser light
M_{avg} =	0.4678	=	average magnification factor
z =	12.75 inches	=	test section length
R =	53.35 lbf-ft/lbm °R	=	ideal gas constant for air
P =	14.4 lbf/in^2	=	atmospheric pressure

k_w = 0.016 Btu/hr ft. F = the thermal conductivity for air at the wall temperature, δ = 0.2161 inches = boundary layer thickness.

The double image distance (h) can be calculated using the following equation [52].

$$h = \frac{B\pi}{180}\left(f - \frac{uw}{f} + w\right)$$

where for this test case:

B =	0.0527°	=	separation angle of Wollaston Prism
f =	64 inches	=	focal length of spherical mirror

The distance from the spherical mirror (SM) focal point to the Wollaston Prism, W, is 18.0 inches and

$$\frac{1}{u} = \frac{1}{f} - \frac{1}{v}$$

where:

V =	91 inches	=	distance from camera to SM

Hence,

$$\frac{1}{u} = \frac{1}{64} - \frac{1}{91} \quad ,$$

which yields:

$$u = 215.7037$$

and therefore the double image distance h = 0.0196 inch.

The average magnification factor and the boundary layer thickness were used to estimate the end effects. From Heidari and Parson [50], Figure 5, for δ/z = (0.2161/12.75) = 0.0169 and h/δ = (.0146/0.2161) = 0.0907

$$\varepsilon = 0.27\%$$

$$\therefore z_{eff} = z(1 + .0027) = 12.75\,(1.0027) = 12.784\,inch$$

The remaining variables were calculated from data collected from the negative of the interferogram.

For determining the fringe spacing (s) and the fringe displacement (Δs), use was made of formulas from analytic geometry. From Irby and Parsons [51], the formula for s is given by

$$s = \frac{1}{N}\left|\frac{\left(y_1-y_2\right)x_4 + \left(x_2-x_1\right)y_4 + \left(x_1-x_2\right)y_3 + \left(y_2-y_1\right)x_3}{\left[\left(y_1-y_2\right)^2 + \left(x_2-x_1\right)^2\right]^{1/2}}\right|$$

where x_i, y_i (i = 1 4) are coordinates of four located points, two on the same fringe and the two others located on separate fringes, all points located on undisturbed portions of the fringes. These points are designated in Figure C2. N is the number of fringes between point 3 and point 4 and the formula for Δs is given by

$$\Delta s = \left| \frac{\left(y_1-y_2\right)x_6 + \left(x_2-x_1\right)y_6 + \left(x_1-x_2\right)y_5 + \left(y_2-y_1\right)x_5}{\left[\left(y_1-y_2\right)^2 + \left(x_1-x_2\right)^2\right]^{1/2}} \right. .$$

The following coordinates were read from the interferogram in Figure C2.

x_1	=	1.3829	y_1	=	0.4397
x_2	=	1.162	y_2	=	0.0861
x_3	=	1.435	y_3	=	0.2976
x_4	=	0.0677	y_4	=	0.3827

The number of fringes, N, between points 3 and 4 is 20.

Therefore, the fringe spacing (s) for this test case is:

$$s = 0.0602 \ .$$

Two additional points (5 and 6) were also measured from the interferogram to obtain the fringe displacement (Δs) at each desired location along the walls. Hence, Δs varies from one location to another.

The ratio of $\Delta s/s$ is an indication of heat flux in the direction normal to the fringe line. The heat flux at the wall in the direction normal to the wall is related to the heat flux in the direction normal to the line by the factor "sin θ," where θ is the angle between the direction normal to the straight reference fringe and the wall. From Figure C-3, one can see that the relationship between the angle θ, the slope angle α of the surface and fringe angle ϕ, is

$$\theta = 90 - (\phi + \alpha)$$

For a vertical surface, the surface slope angle $\alpha = 0$ and hence

$$\theta = 90 - \phi$$

where the fringe angle, Φ, is given by

$$\phi = tan^{-1} \left| \frac{x_2 - x_1}{y_2 - y_1} \right| = 31.994^\circ \; .$$

Using equation C1, the local heat transfer coefficients were calculated at various locations along the unobstructed and the obstructed wall for this sample test; and the results are presented in Tables C1 and C2. Tables C3 through C9 show the calculated local heat transfer coefficients for the other tests.

The estimated uncertainty associated with the experimental values of the heat transfer coefficients (h_{conv}) is approximately 19% (See Appendix D).

TABLE C1: Fringe Shifts and Convection Coefficients Along the Unobstructed Wall as Determined from Figure C2 .

$$h_{conv\,x} = 15.069\ \Delta s/\sin\theta$$

$$\alpha = 0 \text{ degrees}$$

Location (inches from L.E)	Δs (inches)	$h_{conv\,x}$ (Btu/hr ft^2 F)
0.233	0.121351	2.154
0.292	0.1183136	2.102
0.8867	0.0898394	1.596
1.192	0.0816244	1.450
1.443	0.081268	1.444
1.711	0.0757416	1.346
2.021	0.0552766	0.982
2.299	0.0451869	0.803
2.553	0.03452	0.613

TABLE C2: Fringe Shifts and Convection Coefficients Along the Obstructed Wall as Determined from Figure C2 .

$$h_{conv\,x} = 15.069\ \Delta s/\sin\theta$$

Location (inches from L.E)	Δs (inches)	α degrees	$h_{conv\,x}$ (Btu/hr ft^2 F)
0.400	0.07852	0	1.395
0.702	0.0614	0	1.091
0.927	0.05345	0	1.950
1.125	0.0363	0	0.645
1.180	0.0371	75	1.913
1.280	0.03652	42	1.995
1.380	0.0882	10	1.788
1.618	0.006392	0	0.114
2.407	0.05326	0	0.946
2.671	0.0561767	0	0.998

TABLE C3: Fringe Shifts and Convection Coefficients Along the Unobstructed Wall, Ra = 5×10^4, AR = .3636

Location (inches from L.E)	Δs (inches)	$h_{conv\,x}$ (Btu/hr ft^2 F)
0.508	0.0783	1.778
0.719	0.0672	1.526
0.922	0.0638	1.449
1.0921	0.0617	1.401
1.301	0.0561	1.274
1.693	0.0511	1.160
1.881	0.0476	1.081
2.062	0.0415	0.943
2.259	0.0390	0.886
2.442	0.0365	0.829
2.631	0.0343	0.779

TABLE C4: Fringe Shifts and Convection Coefficients Along the Obstructed Wall, Ra = 5×10^4, AR = .3636

Location (inches from L.E)	Δs (inches)	$h_{conv\,x}$ (Btu/hr ft^2 F)
0.234	0.0630	1.431
0.419	0.0598	1.350
0.627	0.0568	1.290
0.807	0.0436	0.990
0.987	0.0329	0.747
1.148	0.0206	0.8890
1.172	0.0245	1.8890
1.233	0.0907	2.441
2.124	0.0290	0.6590
2.284	0.0384	0.8720
2.479	0.0422	0.959

TABLE C5: Fringe Shifts and Convection Coefficients Along the Unobstructed Wall, Ra = 6×10^3, AR = .1818

Location (inches from L.E)	Δs (inches)	$h_{conv\,x}$ (Btu/hr ft^2 F)
0.424	0.0800	1.6240
0.641	0.0702	1.4230
1.100	0.0674	1.366
1.178	0.06601	1.337
1.440	0.06625	1.342
1.640	0.0589	1.193
1.880	0.0322	0.652
2.110	0.0297	0.602
2.380	0.0286	0.580
2.640	0.0277	0.562

TABLE C6: Fringe Shifts and Convection Coefficients Along the Obstructed Wall, Ra = 6×10^3, AR = .1818

Location (inches from L.E)	Δs (inches)	$h_{conv\,x}$ (Btu/hr ft^2 F)
0.197	0.0982	1.989
0.528	0.0595	1.205
0.822	0.0558	1.130
1.399	0.0787	1.594
1.500	0.0120	0.243
1.600	0.0103	0.209
1.973	0.0229	0.464
2.232	0.0267	0.541
2.491	0.0353	0.715

TABLE C7: Fringe Shifts and Convection Coefficients Along the Unobstructed Wall, Ra = 2.6×10^3, AR = .1364

Location (inches from L.E)	Δs (inches)	$h_{conv\ x}$ (Btu/hr ft^2 F)
0.407	0.0702	1.440
0.620	0.0591	1.212
0.792	0.0379	0.777
1.037	0.0525	1.076
1.263	0.0548	1.124
1.407	0.0439	0.901

TABLE C8: Fringe Shifts and Convection Coefficients Along the Obstructed Wall, Ra = 2.6×10^3, AR = .1364

Location (inches from L.E)	Δs (inches)	$h_{conv\,x}$ (Btu/hr ft^2 F)
0.429	0.0597	1.224
0.773	0.0285	0.584
1.480	0.0140	0.397
1.520	0.0164	0.345
1.630	0.0047	0.096
2.421	0.0066	0.135

TABLE C9: Fringe Shifts and Convection Coefficients Along the Wall of the Unobstructed Channel, Ra = 1.8×10^4

Location (inches from L.E)	Δs (inches)	$h_{conv\,x}$ (Btu/hr ft^2 F)
0.613	0.0657	1.457
0.633	0.0646	1.433
0.835	0.0614	1.362
1.034	0.0591	1.311
1.177	0.0540	1.149
1.419	0.0588	1.304
1.560	0.0541	1.200
1.833	0.0488	1.082
1.960	0.0479	1.063
2.220	0.0478	1.060

APPENDIX D

ERROR ANALYSIS

"Uncertainty" is defined as the estimated value of the error in an experimental measurement. In this Appendix, the uncertainties in the MZI and WPI data will be calculated. The analysis will follow the technique described by Kline and McClintock [53].

D-1 Uncertainty Analysis of the MZI Data

The air temperature values obtained with the interferometer were calculated using the following equation

$$T = \frac{T_w}{\left(1 + \left(\frac{CT_w}{P_\infty L}\right)S\right)} \tag{D-1}$$

where T_W is the wall temperature in °K, P_∞ is the air pressure in mmHg, L is the wall length in meters, S is the fringe number, and $C = 2\lambda R/3r = 0.005406$.

Assume that the uncertainty in the temperature, T, is due to uncertainties in the quantities T_W, P_∞, L, and S. And those due to C are neglected.

Hence, using the technique of Kline and McClintock, the resultant uncertainty in temperature, T, may be written as

$$\omega_T = \left[\left(\omega_{T_\omega} \frac{\partial T}{\partial T_w}\right)^2 + \left(\omega_{P_\infty} \frac{\partial T}{\partial P_\infty}\right)^2 + \left(\omega_L \frac{\partial T}{\partial L}\right)^2 + \left(\omega_S \frac{\partial T}{\partial S}\right)^2\right]^{1/2} \tag{D-2}$$

where ω_{T_w}, ω_{P_∞}, ω_L and ω_S are the uncertainties in T_W, P_∞, L, and S respectively. And performing the partial differentiations on the equation for temperature (D1), we get

$$\frac{\partial T}{\partial T_{\omega}} = \frac{\left[D - \left(\frac{CS}{P_{\infty}L}\right)T_{w}\right]}{D^2} ,$$

$$\frac{\partial T}{\partial P_{\infty}} = \frac{\left[\left(\frac{CS}{P_{\infty}^2 L}\right)T_{w}^2\right]}{D^2} ,$$

$$\frac{\partial T}{\partial L} = \frac{\left[\left(\frac{CS}{P_{\infty}L^2}\right)T_{w}^2\right]}{D^2} ,$$

$$\frac{\partial T}{\partial S} = -\frac{\left[\left(\frac{C}{P_{\infty}L}\right)T_{w}^2\right]}{D^2} ,$$

where:

$$D = 1 + \left(\frac{CT_{w}}{P_{\infty}L}\right)S .$$

Substituting the nominal values of T_W = 327.4°K, P_∞ = 744.45 mmHg, L = 0.3256 m, and S = 0 or 10 (the minimum and approximate maximum values of S), we get the results shown in the following table

	S	
	0	10
$\partial T/\partial T_{\omega}$	1.0	0.869
$\partial T/\partial P_{\infty}$	0.0	0.028
$\partial T/\partial L$	0.0	63.770
$\partial T/\partial S$	2.391	2.076

Thus at S = 0,

$$\Delta T = \left[\left(\omega_{T_w} \right)^2 + \left(2.391 \ \omega_s \right)^2 \right]^{1/2} \qquad \text{(D-3)}$$

and at S = 10

$$\Delta T = \left[\left(0.869 \, \omega_{T_w} \right)^2 + \left(0.028 \, \omega_{P_\infty} \right)^2 + \left(63.77 \, \omega_L \right)^2 + \left(2.076 \ \omega_s \right)^2 \right]^{1/2} . \qquad \text{(D-4)}$$

Assuming (these assumptions are based on the least count of the measuring instrument),

$$\omega_{T_w} = 0.3°C \ , \ \omega_{P_\infty} = 1 \ mmHg \ , \ \omega_L = .005 \ m, \ and \ \omega_S = 0.1 \ ,$$

and substituting in equations (D3) and (D4), we get for S = 0

$$\Delta T = 0.38°C$$

and for S = 10

$$\Delta T = 0.462°C \ .$$

D-2 <u>Uncertainty Analysis of the WPI Data</u>

An uncertainty analysis was performed for the experimental heat transfer coefficients obtained by Wollaston Prism Interferometer techniques. The equations and assumptions used and the results of this analysis are presented below.

As shown in Appendix C, the experimental heat transfer coefficients can be obtained from the following equation:

$$h_{conv} = \left[\frac{\lambda}{K_{GD} Z_{eff} \, h} \right] \left(\frac{R T_w^2}{P} \right) \frac{k_\omega}{\sin\theta \, \Delta T} \left(\frac{\Delta S}{S} \right)$$

where

$$\Delta T = \left(T_w - T_\infty \right)$$

Assume that the uncertainty in h_{conv} is due to uncertainties in the quantities h, ΔS, S, T_W, P, θ, z_{eff} and ΔT and that those due to k_ω, λ, K_{GD} and R are neglected. Then,

$$h = \beta(f - \frac{uw}{f} + w),$$

$$\frac{\partial h}{\partial \beta} = \left(f - \frac{uw}{f} + w\right); \frac{\partial h}{\partial f} = \beta\left(1 + \frac{uw}{f^2}\right),$$

$$\frac{\partial h}{\partial u} = -\frac{\beta w}{f}, \quad \frac{\partial h}{\partial w} = \beta\left(1 - \frac{u}{f}\right).$$

and

$$\omega_\beta = 5\%, \ \omega_f = 1.0 \ inch, \ \omega_w = .25 \ inch, \ \omega_v = .5 \ inch,$$

assume that

$$f = 64 \ inch, \ v = 91 \ inch, \ w = 18 \ inch,$$

and

$$u = \frac{1}{\left(\frac{1}{f} - \frac{1}{v}\right)} = \left(\frac{vf}{v - f}\right) = 215.7037 \ inch,$$

Then,

$$\omega_u = \frac{\partial u}{\partial f} = \left(\frac{v}{v - f}\right) + \left(\frac{1}{v - f}\right)^2 vf,$$

$$\frac{\partial u}{\partial v} = \frac{f}{v - f} + \frac{vf}{v - f},$$

$$\omega_u = \left[\left(\omega_f \frac{\partial u}{\partial f}\right)^2 + \left(\omega_v \frac{\partial u}{\partial v}\right)^2\right]^{1/2},$$

and

$$\omega_u = \left[\left(1.0 \left(\frac{91}{91-64} + \frac{91(64)}{(91-64)^2} \right) \right)^2 + \left(0.5 \left(\frac{91}{91-64} - \frac{91(64)}{(91-64)^2} \right) \right)^2 \right]^{1/2},$$

or,

$$\omega_u = 11.59 \; inches = 5.4\% .$$

Similarly,

$$\omega_h = \left[\left(\omega_\beta \frac{\partial h}{\partial \beta} \right)^2 + \left(\omega_f \frac{\partial h}{\partial f} \right)^2 + \left(\omega_u \frac{\partial h}{\partial u} \right)^2 + \left(\omega_w \frac{\partial h}{\partial w} \right)^2 \right]^{1/2} .$$

or,

$$\omega_h = \left[\left(\frac{0.0026\pi}{180} \left(64 - \frac{215.7(18)}{64} + 18 \right) \right)^2 \right.$$

$$+ \left(1.0 \; \frac{0.0527\pi}{180} \left(1 + \frac{215.7(18)}{(64)^2} + \cancel{18} \right) \right)^2$$

$$+ \left(\frac{11.59(0.0527)\pi}{180} \; \frac{(18)}{64} + 18 \right)^2$$

$$\left. + \left(\frac{0.25(0.0527)\pi}{180} \left(1 - \frac{215.7}{64} \right) \right)^2 \right]^{1/2}$$

$$\omega_h = 0.0037 = 18.7\% \quad = uncertainty \; in \; the \; double \; image \; distance$$

Assume:

$$\omega_{\Delta S} = 2\% \, , \; \omega_S = 2\% \, , \; \omega_T = 0.5°R \, , \; \omega_{\Delta T} = 0.5°R \, ,$$

$$\omega_\theta = 1\% \, , \; \omega_P = 0.13\% \, , \; \omega_{Z_{eff}} = 1.5\% \, .$$

Then, we may calculate the following quantities:

$$\frac{\partial h_c}{\partial z_{eff}} = \left(\frac{-\lambda}{K_{GD} z_{eff}^2 h}\right)\left(\frac{\Delta S}{S}\right)\left(\frac{RT_w^2}{P}\right)\left(\frac{K_w}{\sin\theta\,\Delta T}\right) = \frac{A(\Delta S)}{z_{eff}}$$

$$\frac{\partial h_c}{\partial h} = \left(\frac{-\lambda}{K_{GD} z_{eff} h^2}\right)\left(\frac{\Delta S}{S}\right)\left(\frac{RT_w^2}{P}\right)\left(\frac{K_w}{\sin\theta\,\Delta T}\right) = \frac{A(\Delta S)}{h} \quad ,$$

$$\frac{\partial h_c}{\partial \Delta S} = \left(\frac{\lambda}{K_{GD} z_{eff} h}\right)\left(\frac{1}{S}\right)\left(\frac{RT_w^2}{P}\right)\left(\frac{K_w}{\sin\theta\,\Delta T}\right) = A \quad ,$$

$$\frac{\partial h_c}{\partial S} = \left(\frac{\lambda}{K_{GD} z_{eff} h}\right)\left(\frac{-\Delta S}{S^2}\right)\left(\frac{RT_w^2}{P}\right)\left(\frac{K_w}{\sin\theta\,\Delta T}\right) = \frac{A(\Delta S)}{S} \quad ,$$

$$\frac{\partial h_c}{\partial T_w} = \left(\frac{\lambda}{K_{GD} z_{eff} h}\right)\left(\frac{\Delta S}{S}\right)\left(\frac{2RT_w}{P}\right)\left(\frac{K_w}{\sin\theta\,\Delta T}\right) = \frac{2A(\Delta S)}{T_\omega} \quad ,$$

$$\frac{\partial h_c}{\partial P} = \left(\frac{\lambda}{K_{GD} z_{eff} h}\right)\left(\frac{\Delta S}{S^2}\right)\left(\frac{-RT_w^2}{P^2}\right)\left(\frac{K_w}{\sin\theta\,\Delta T}\right) = \frac{A(\Delta S)}{P} \quad ,$$

$$\frac{\partial h_c}{\partial \theta} = \left(\frac{\lambda}{K_{GD} z_{eff} h}\right)\left(\frac{\Delta S}{S}\right)\left(\frac{RT_w^2}{P}\right)\left(\frac{-K_w\cos\theta}{\sin^2\theta\,\Delta T}\right) = \frac{A(\Delta S)}{\tan\phi} \quad ,$$

$$\frac{\partial h_c}{\partial \Delta T} = \left(\frac{\lambda}{K_{GD} z_{eff} h}\right)\left(\frac{\Delta S}{S}\right)\left(\frac{RT_w^2}{P}\right)\left(\frac{-K_w}{\sin\theta\,\Delta T^2}\right) = \frac{A(\Delta S)}{\Delta T} \quad ,$$

and

$$\omega_{h_{c_x}} = \left[\left(\omega_{z_{eff}} \frac{\partial h_c}{\partial z_{eff}}\right)^2 + \left(\omega_h \frac{\partial h_c}{\partial h}\right)^2 + \left(\omega_{\Delta S} \frac{\partial h_c}{\partial \Delta S}\right)^2 + \left(\omega_S \frac{\partial h_c}{\partial S}\right)^2\right.$$

$$\left. + \left(\omega_{T_w} \frac{\partial h_c}{\partial T_w}\right)^2 + \left(\omega_P \frac{\partial h_c}{\partial P}\right)^2 + \left(\omega_\theta \frac{\partial h_c}{\partial \theta}\right)^2 + \left(\omega_{\Delta T} \frac{\partial h_c}{\partial \Delta T}\right)^2\right]^{1/2}.$$

where:

$$A = \left[\frac{\lambda}{K_{GD} Z_{eff}\, h}\right]\left(\frac{R T_w^2}{P}\right)\frac{k_w}{\sin\theta\, \Delta T}\left(\frac{1}{S}\right)$$

$$= 17.768\,.$$

Therefore,

$$\omega_{h_{conv}} = \left[\left(\frac{0.015\, z_{eff}\, A(\Delta S)}{z_{eff}}\right)^2 + \left(\frac{0.187 h\, A(\Delta S)}{h}\right)^2 + \left(0.02\, A(\Delta S)\right)^2\right.$$

$$+ \left(\frac{0.02(S) A(\Delta S)}{S}\right)^2 + \left(\frac{0.278(2)\, A(\Delta S)}{T_w}\right)^2 + \left(\frac{0.0013 P\, A(\Delta S)}{P}\right)^2$$

$$\left. + \left(\frac{0.01 \sin\theta\, \cos\theta\, A(\Delta S)}{\sin\theta}\right)^2 + \left(\frac{0.5\, A(\Delta S)}{\Delta T}\right)^2\right]^{1/2}$$

$$\omega_{h_{conv}} = A \Delta S\left[\left(.015\right)^2 + \left(.187\right)^2 + 2\left(.02\right)^2 + \left(.0017\right)^2\right.$$

$$\left. + \left(.0013\right)^2 + \left(.005\right)^2 + \left(.009\right)^2\right]^{1/2}$$

$$\omega_{h_{conv}} = 17.768\ (0.190\ \Delta S)$$

$$= \textit{uncertainty in the convective heat transfer coefficient on the channel wall}$$

From Table C1, for ΔS = 0.0816244 inch we have:

$$h_{conv} = 1.45\ \frac{Btu}{hr\,ft^2F}$$

$$\therefore\ \omega_{h_{conv}} = 3.3761\ (0.0816244) = 0.27558\,\frac{Btu}{hr\,ft^2F}$$

$$or\quad \omega_{h_{conv}} = \frac{0.27558}{1.45} = 19\%\ .$$

APPENDIX E

AVERAGE NUSSELT NUMBER

The following is the procedure used to calculate the average Nusselt number for the obstructed channel:

Average Nusselt number is defined as:

$$\overline{N}u = \frac{\overline{h}\,b}{k} \tag{1}$$

where	h	is the average heat transfer coefficient
	b	is the spacing between the two vertical walls
	k	is the thermal conductivity of fluid

The heat transfer coefficient, h, is defined as

$$\overline{h} = \frac{\overline{Q}}{A\Delta T} \tag{2}$$

where	Q	is the total heat transfer from the channel walls to the fluid
	A	wetted area of the channel walls
	ΔT	difference between the wall temperature and ambient temperature (T_W-T_∞)

$$\overline{Q} = \overline{Q}_1 + \overline{Q}_2 \tag{3}$$

$$A = A_1 + A_2 \tag{4}$$

$$\overline{Q}_1 = \overline{h}_1 A_1 \Delta T \tag{5}$$

$$\overline{Q}_2 = \overline{h}_2 A_2 \Delta T \tag{6}$$

$$A_1 = L_1 Z \tag{7}$$

$$A_2 = L_2 Z \tag{8}$$

where L height of the wall

Z length of the wall

Subscripts

1 refers to obstructed wall

2 refers to unobstructed wall

Substituting equations (3) to (8) into equation (2), we get

$$\overline{h} = \frac{\overline{h}_1 A_1 \Delta T + \overline{h}_2 A_2 \Delta T}{(A_1 + A_2)\Delta T}$$

$$= \frac{\overline{h}_1 A_1 + \overline{h}_2 A_2}{A_1 + A_2}$$

$$\overline{h} = \frac{\overline{h}_1 L_1 + \overline{h}_2 L_2}{L_1 + L_2} \tag{9}$$

Substituting equation (9) into equation (1) we get

$$\overline{N}u = \left(\frac{\overline{h}_1 L_1 + \overline{h}_2 L_2}{L_1 + L_2} \right) \frac{b}{k}$$

Note that in the case of an unobstructed channel ($L_1 = L_2$), the above eqn. reduces to eqn (1).

APPENDIX F

As has been pointed out in section 1.1, all the figures will be found in this Appendix.

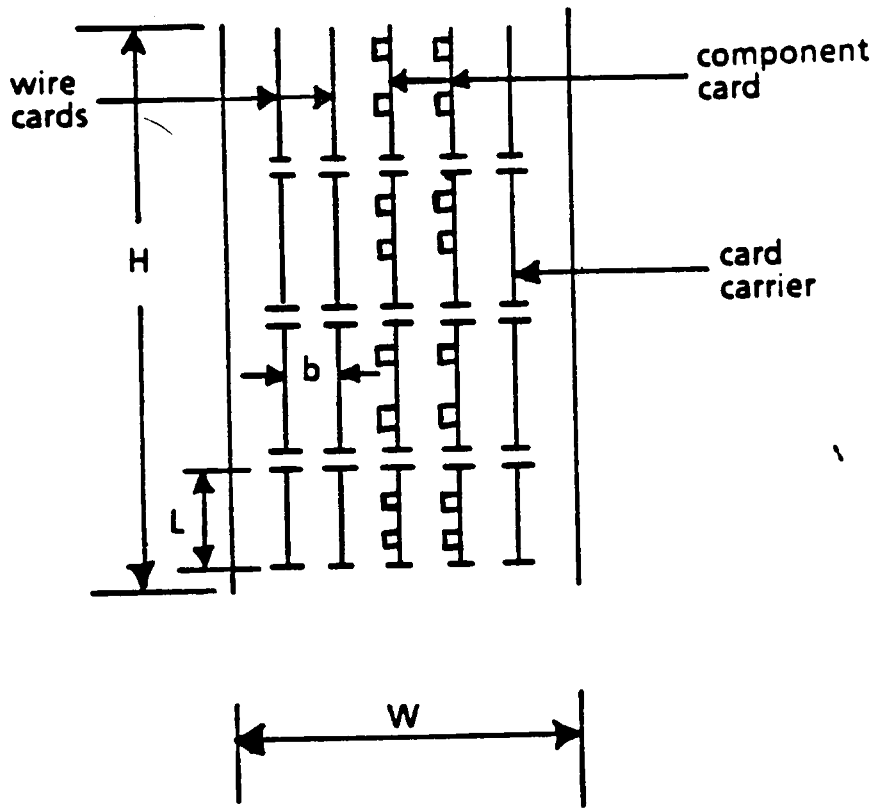

Figure 1. Arrays of component cards forming vertical channels cooled by natural convection.

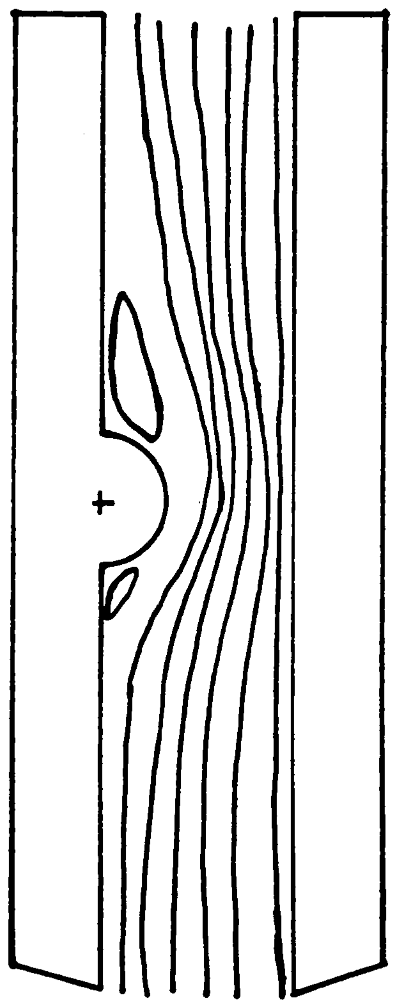

Figure 2. Geometry of an obstructed channel showing typical regions of recirculating flow.

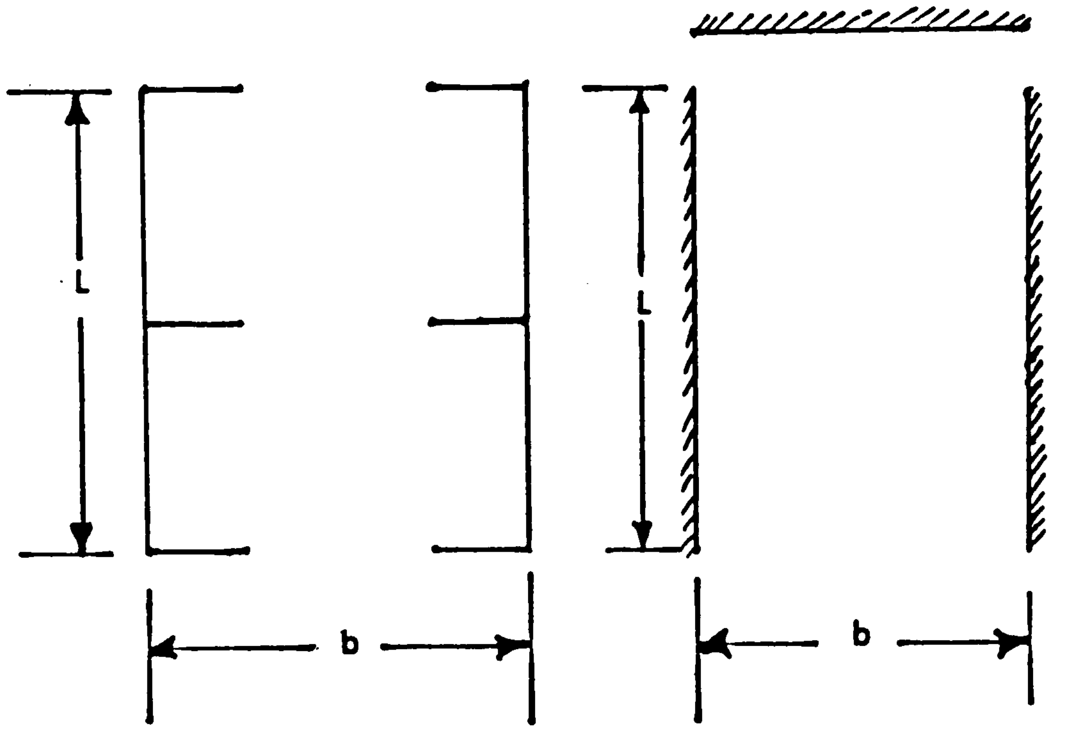

(a) staggered cards (b) baffle

Figure 3. Schematics of staggered cards and baffle arrangements [14].

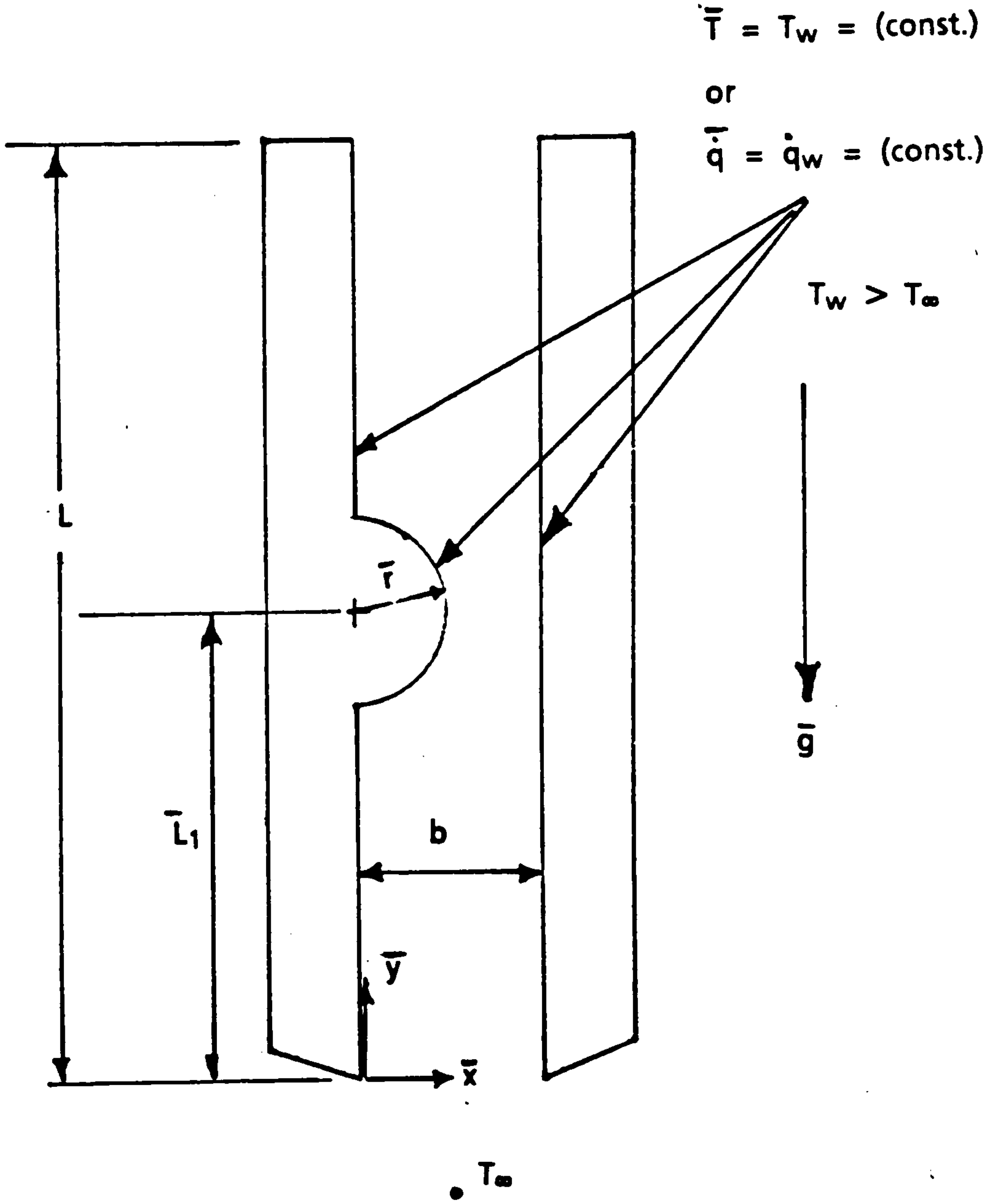

Figure 4. Geometry of the obstructed channel considered in this investigation.

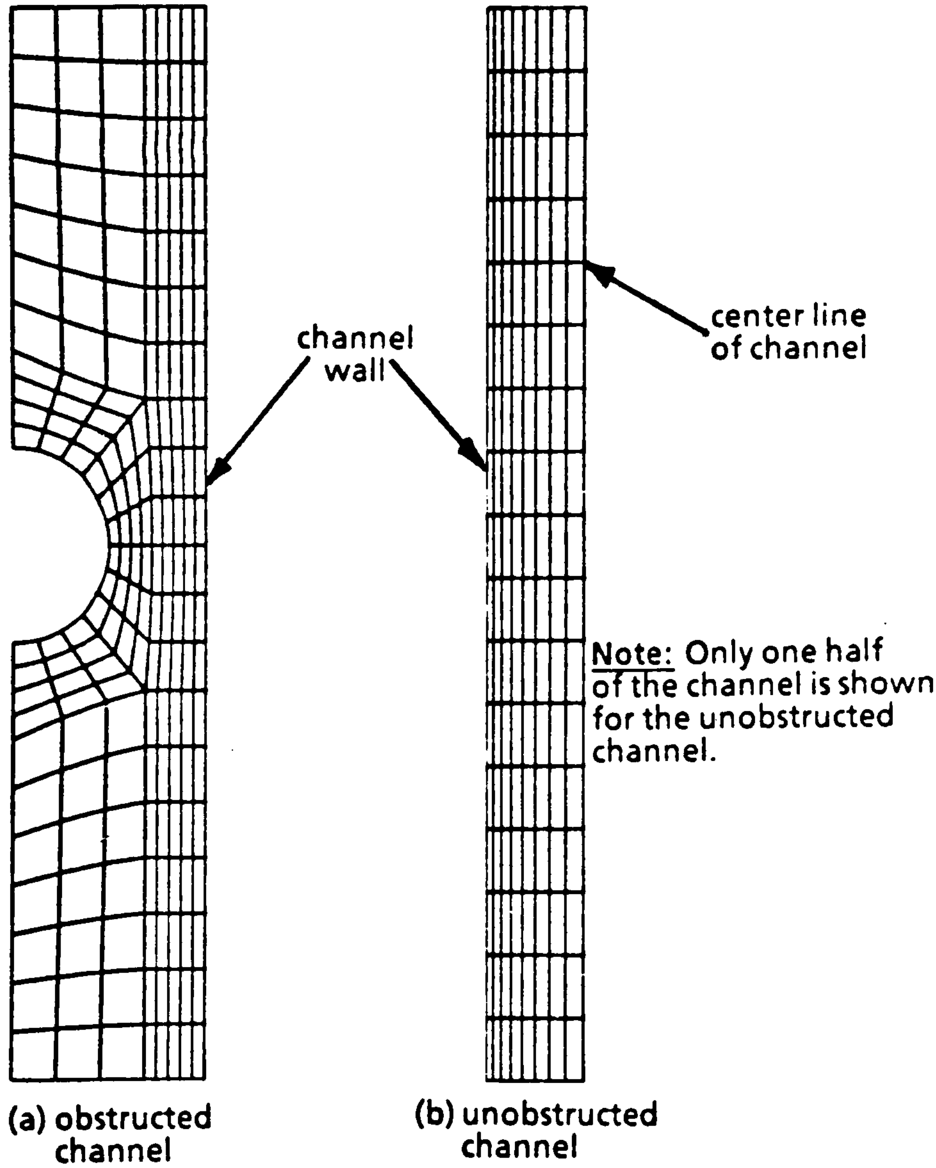

Figure 5. Mesh generation

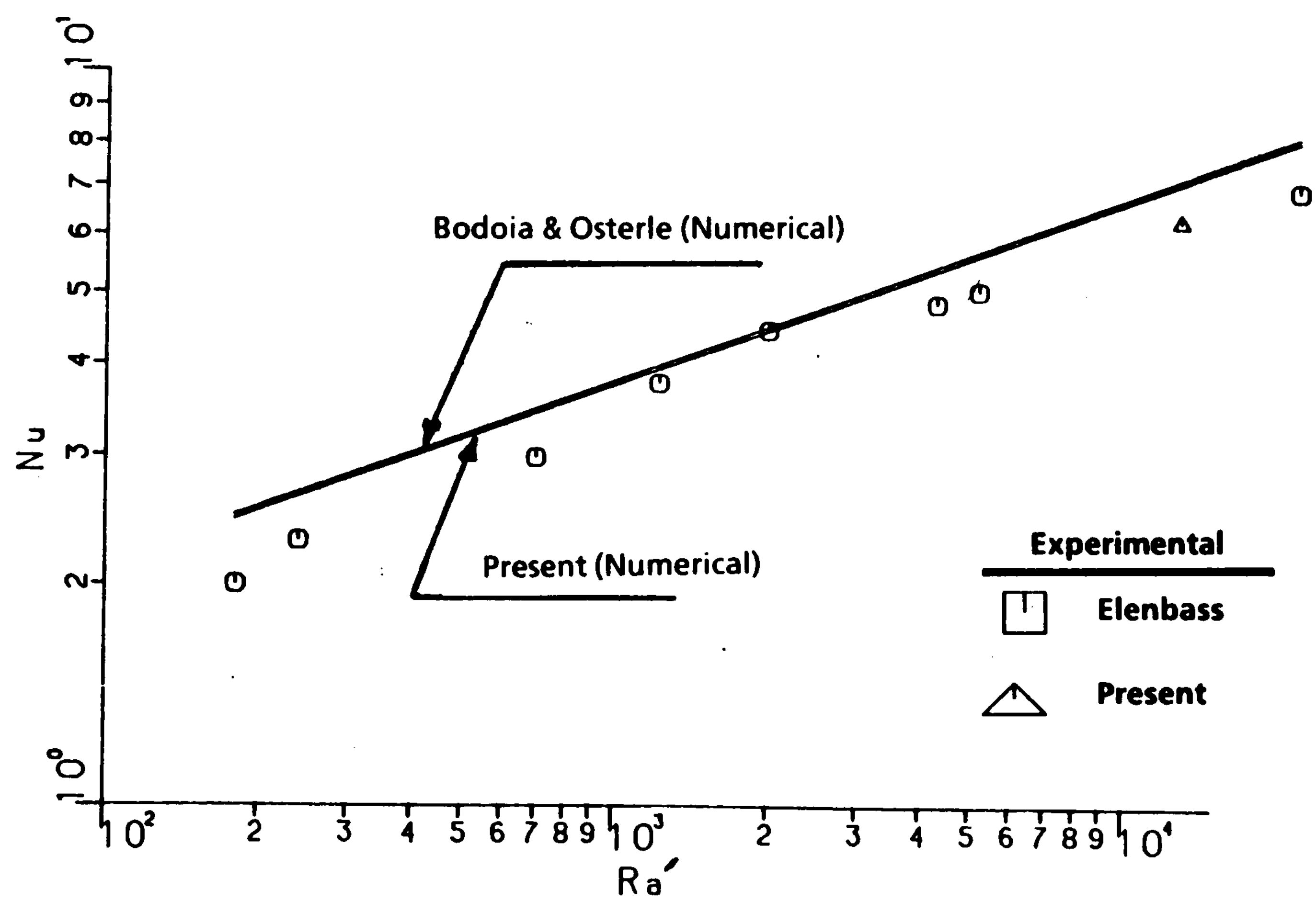

Figure 6. Comparison between present solution and those of Bodoia & Osterle [10] and Elenbass [26] for unobstructed channel.

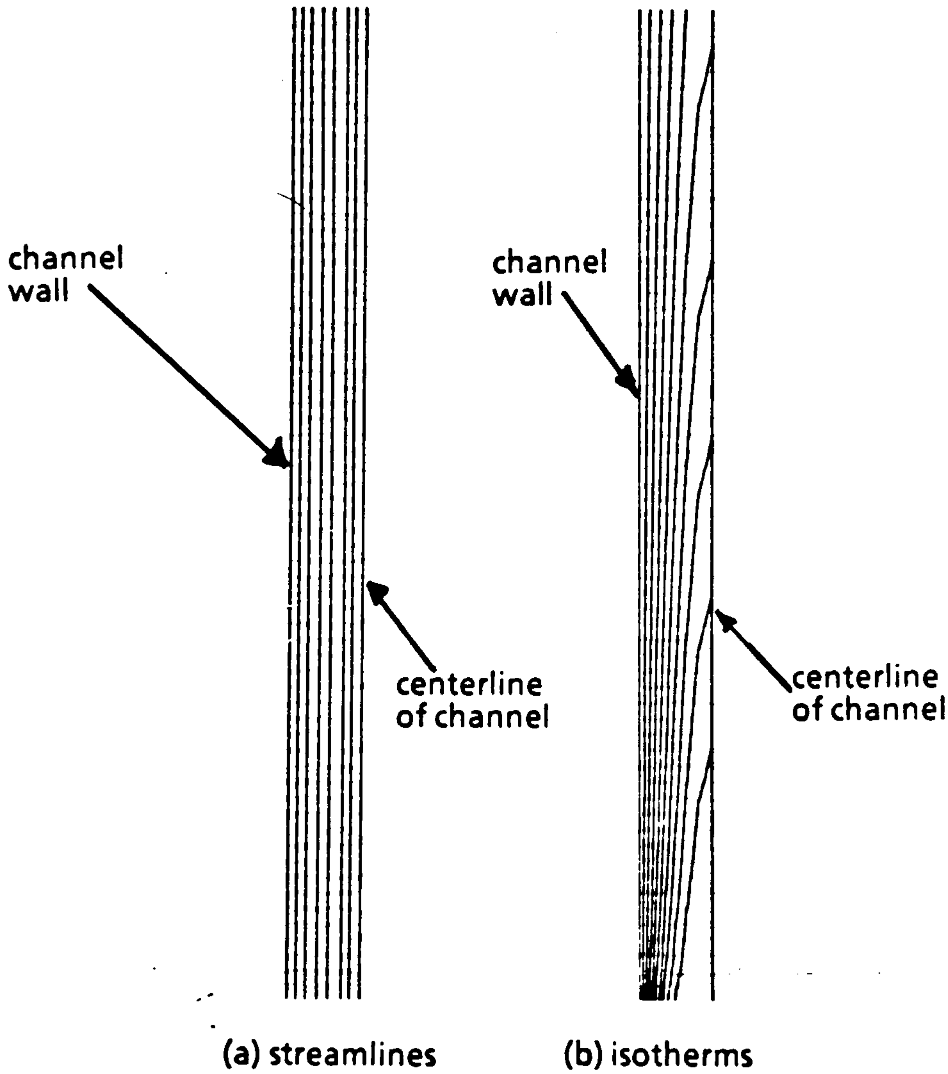

Figure 7. Pattern of the computed streamlines and isotherms for an unobstructed channel with Ra $= 3.5 \times 10^2$

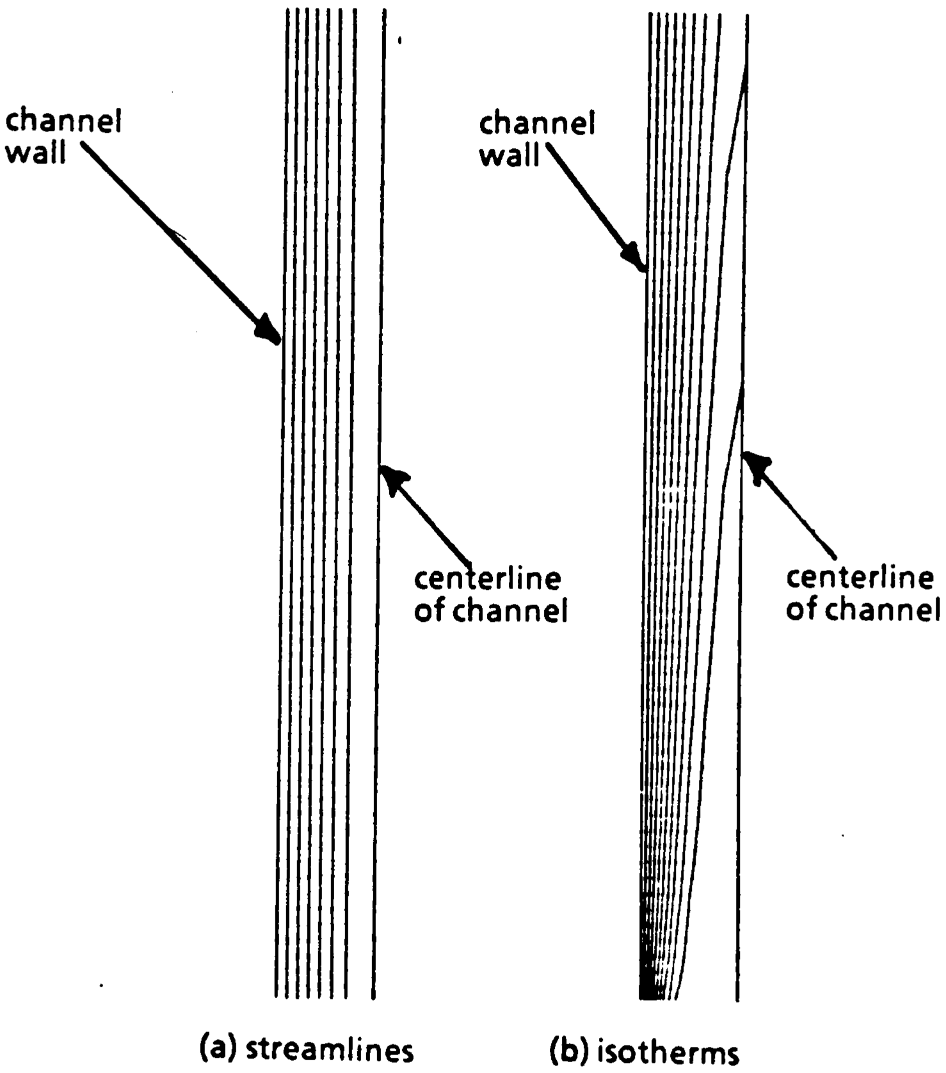

Figure 8. Pattern of the computed streamlines and isotherms for an unobstructed channel with Ra = 1.0×10^3

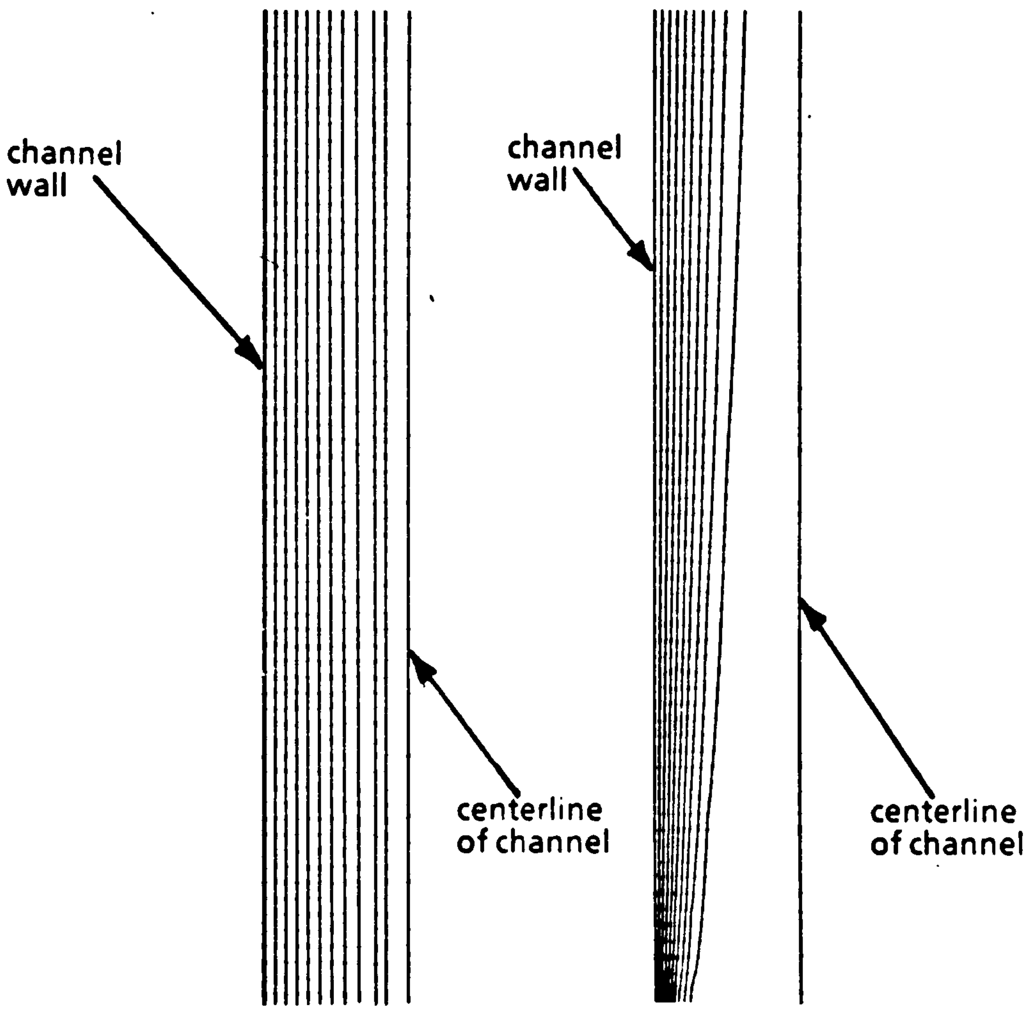

(a) streamlines (b) isotherms

Figure 9. Pattern of the computed streamlines and isotherms for an unobstructed channel with Ra $= 5.5 \times 10^3$

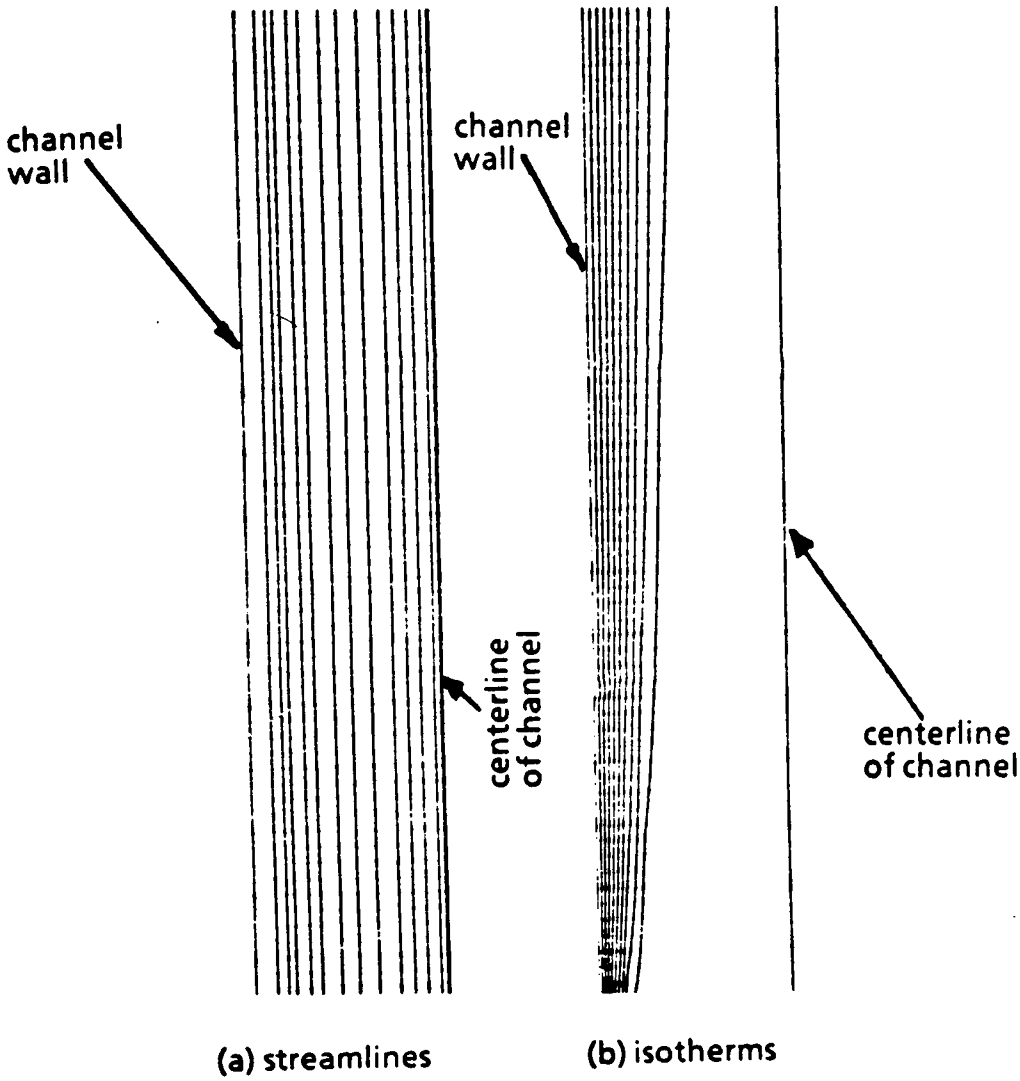

Figure 10. Pattern of the computed streamlines and isotherms for an unobstructed channel with $Ra = 1.8 \times 10^4$

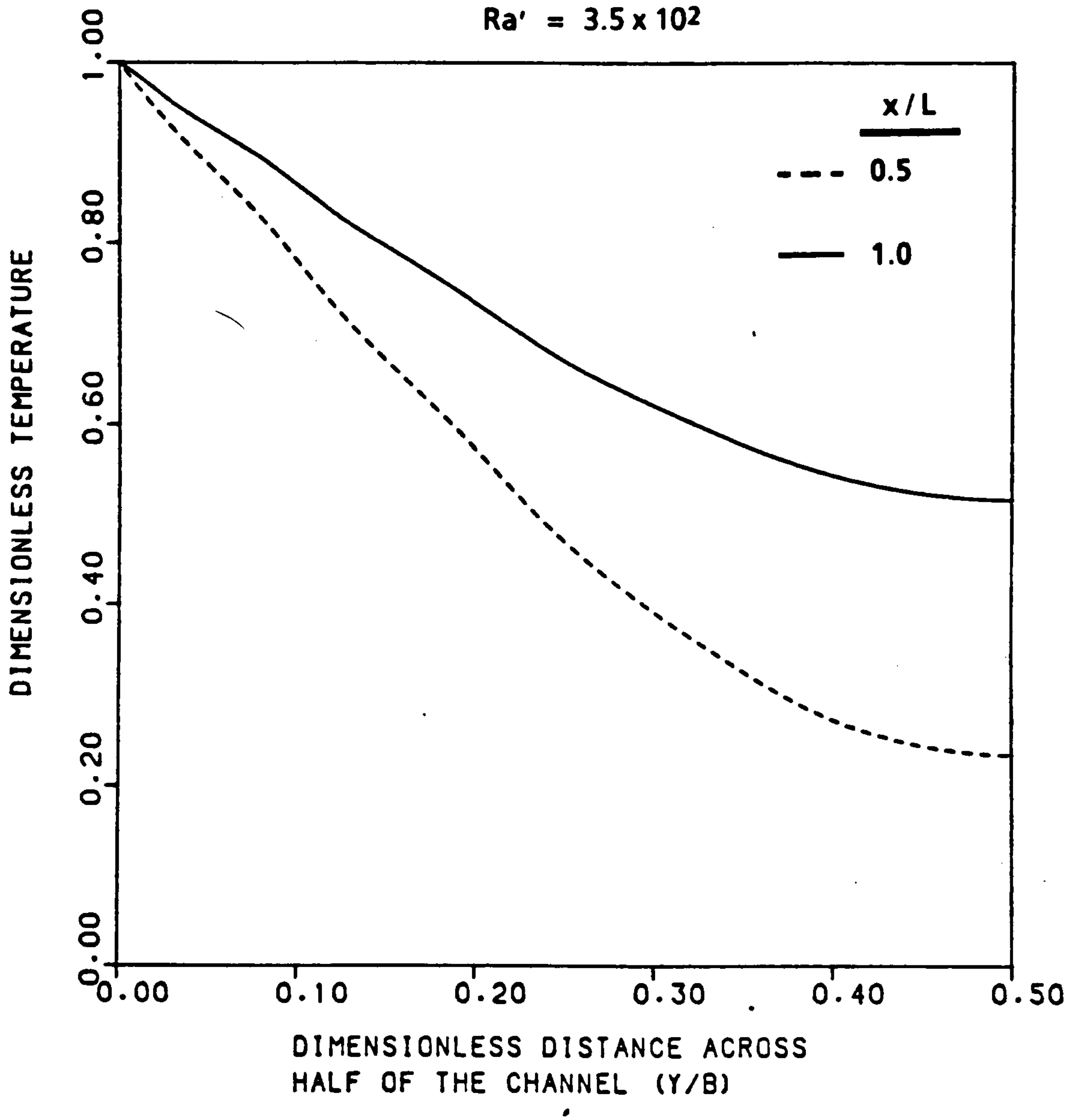

Figure 11. Transverse temperature distributions in an unobstructed vertical channel.

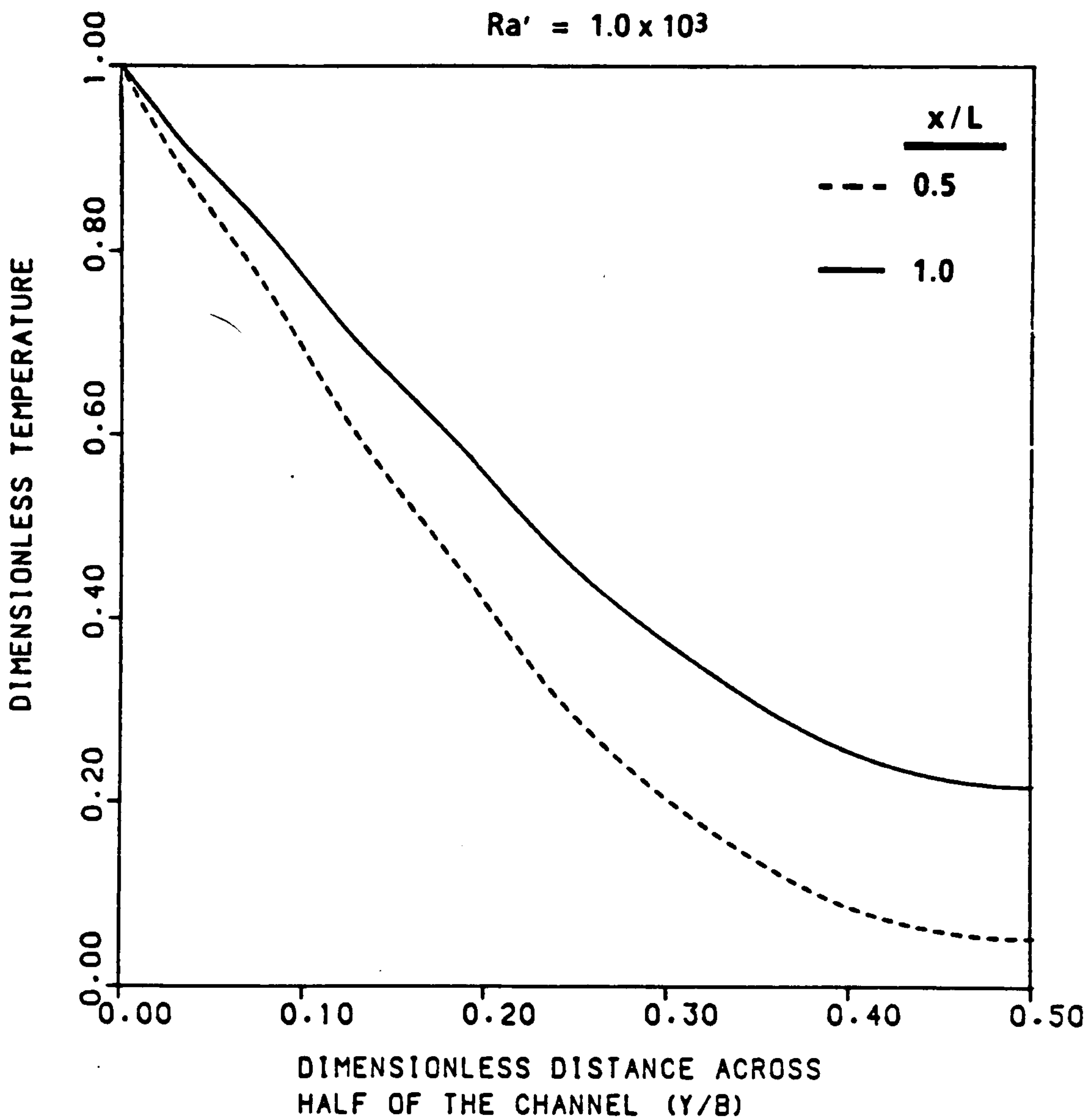

Figure 12. Transverse temperature distributions in an unobstructed vertical channel.

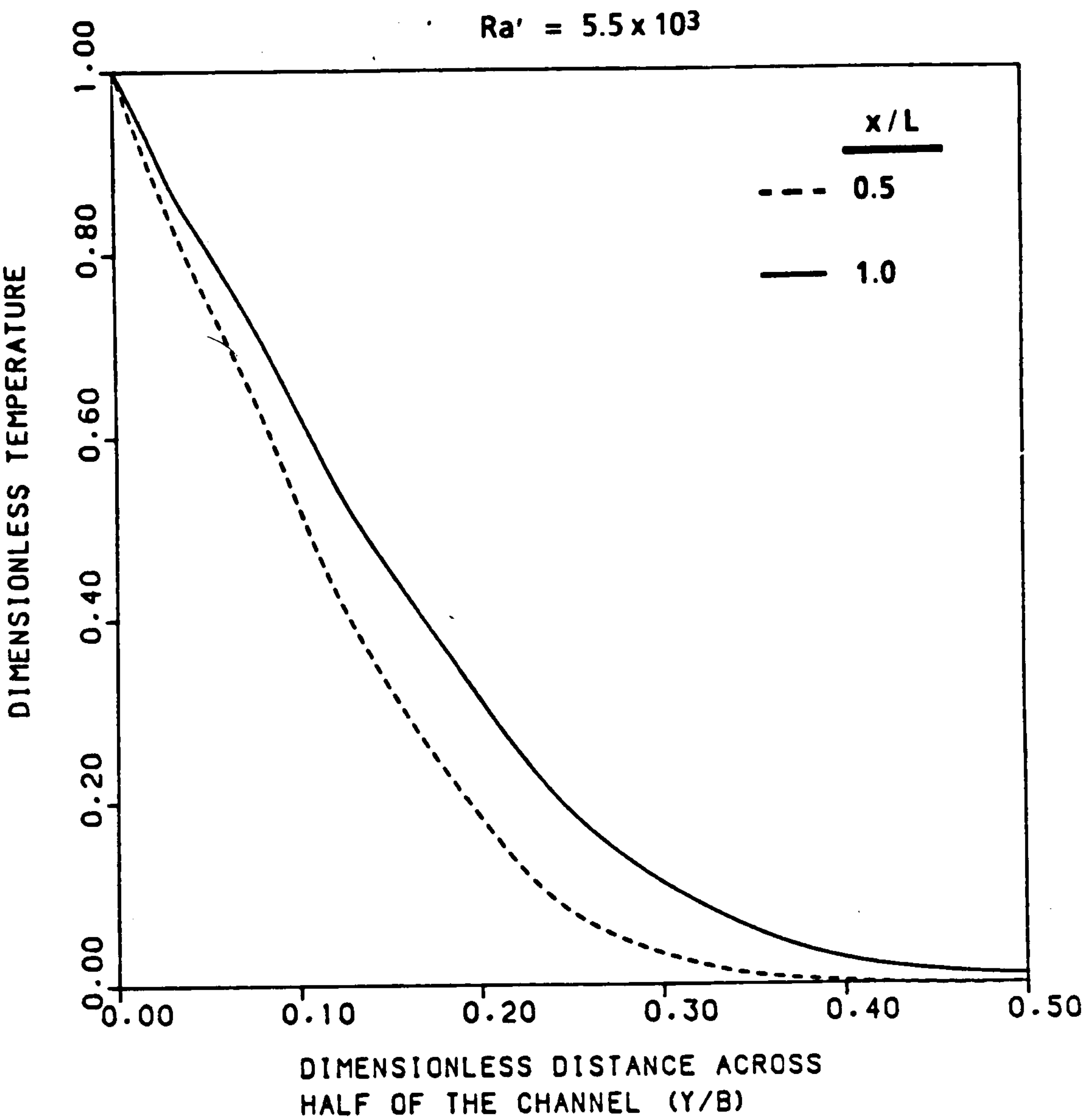

Figure 13. Transverse temperature distributions in an unobstructed vertical channel.

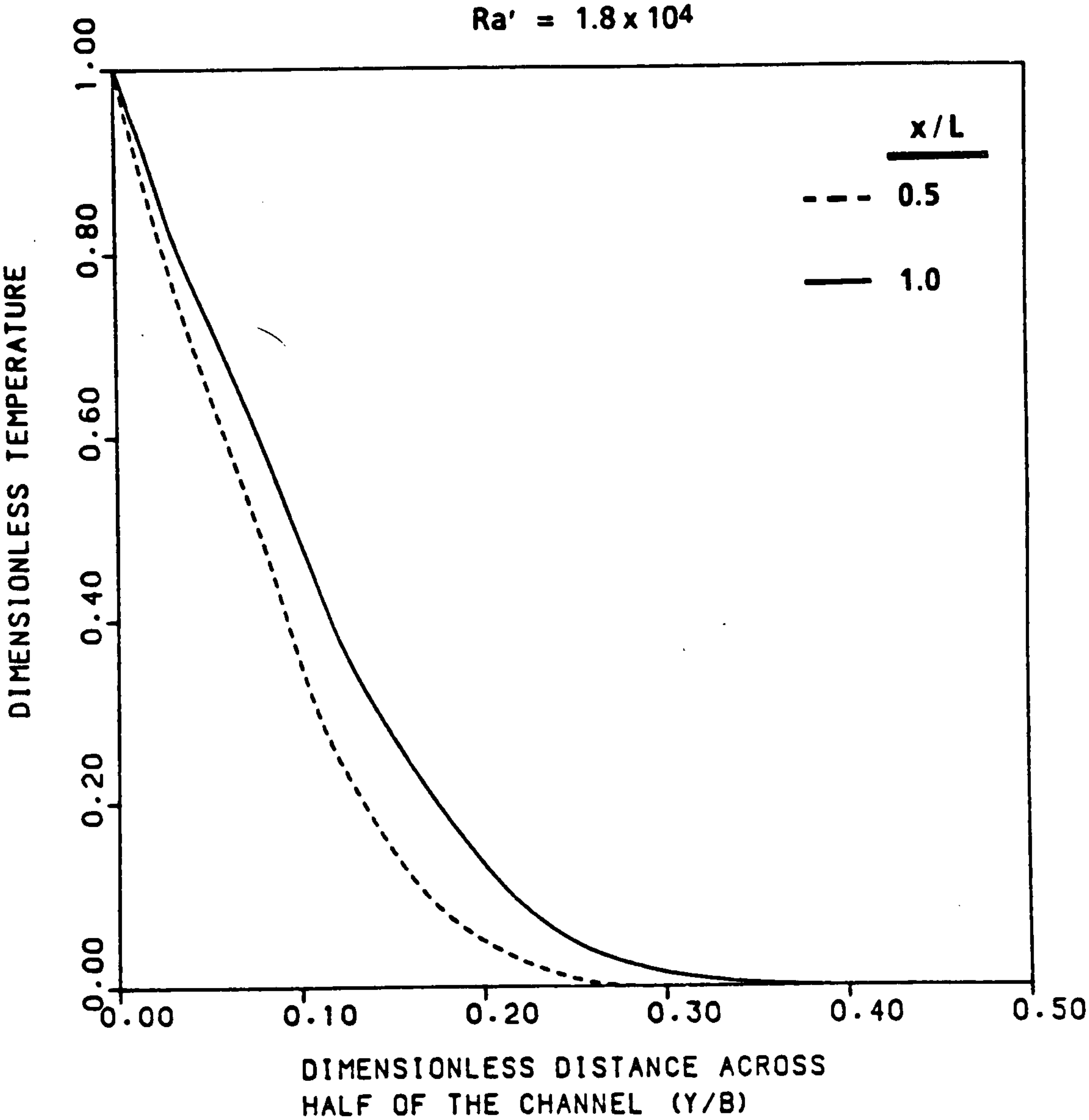

Figure 14. Transverse temperature distributions in an unobstructed vertical channel.

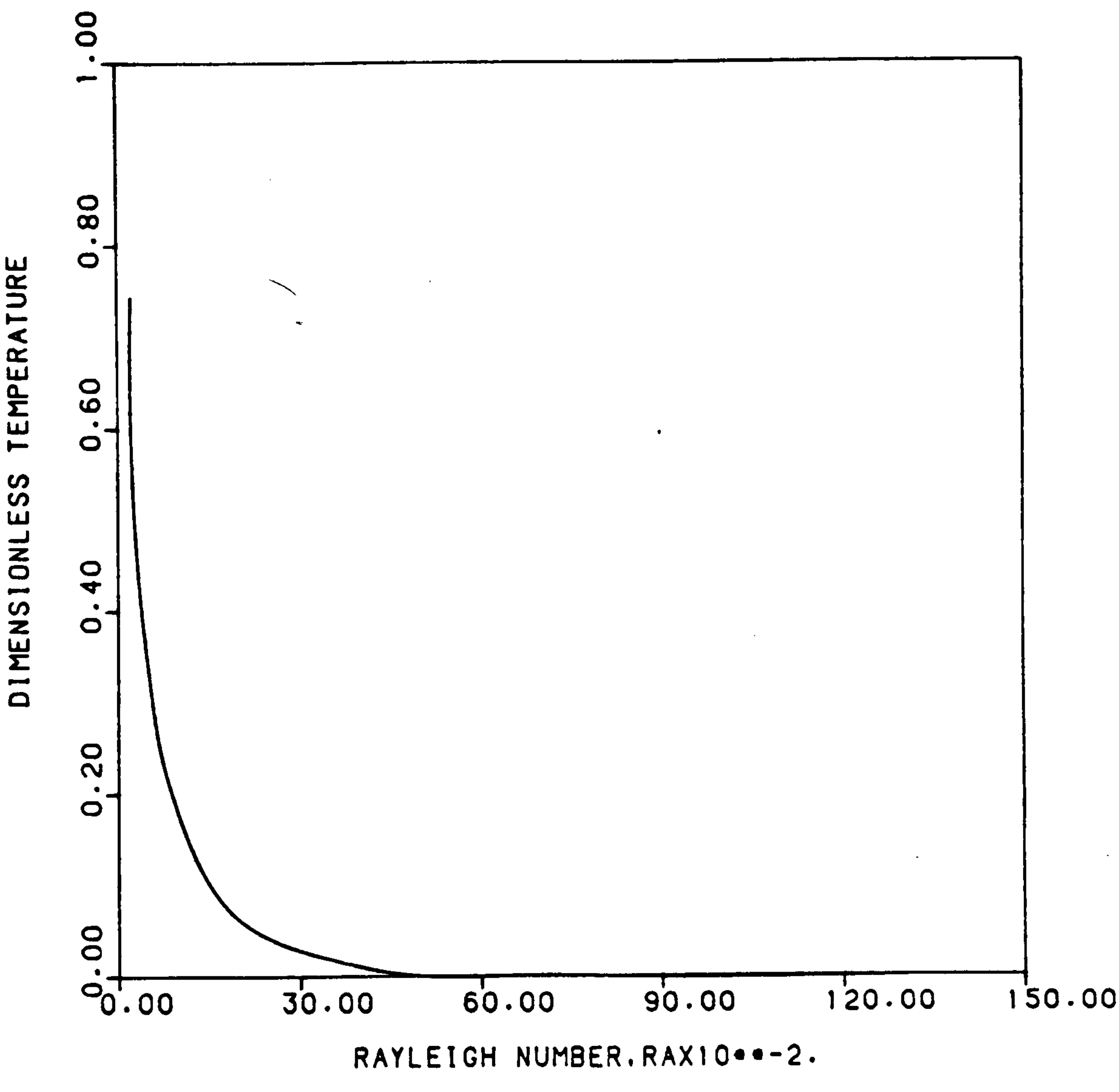

Figure 15. Variation of the maximum dimensionless temperature on the center line at the exit plane.

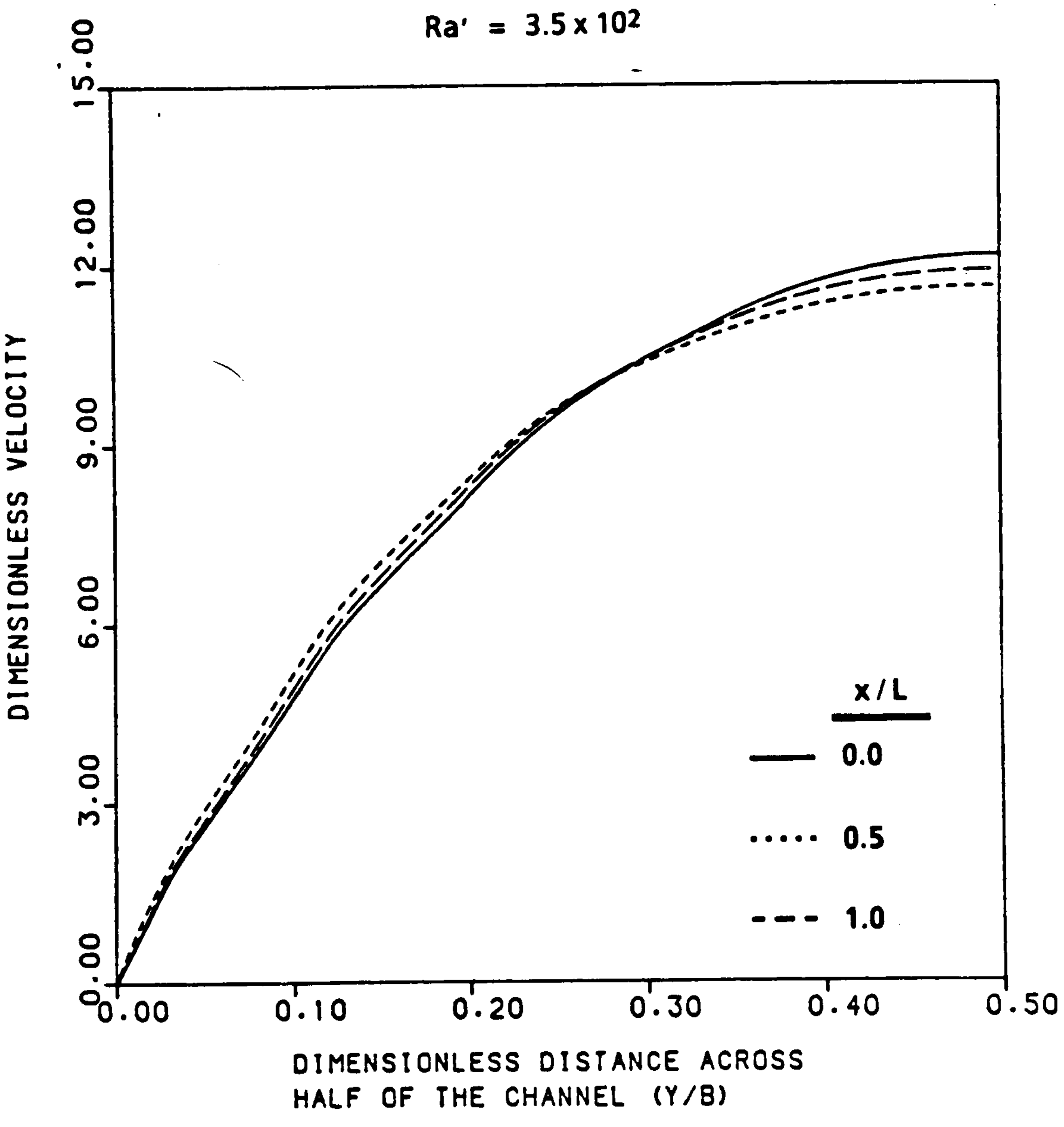

Figure 16. Velocity distributions in an unobstructed vertical channel.

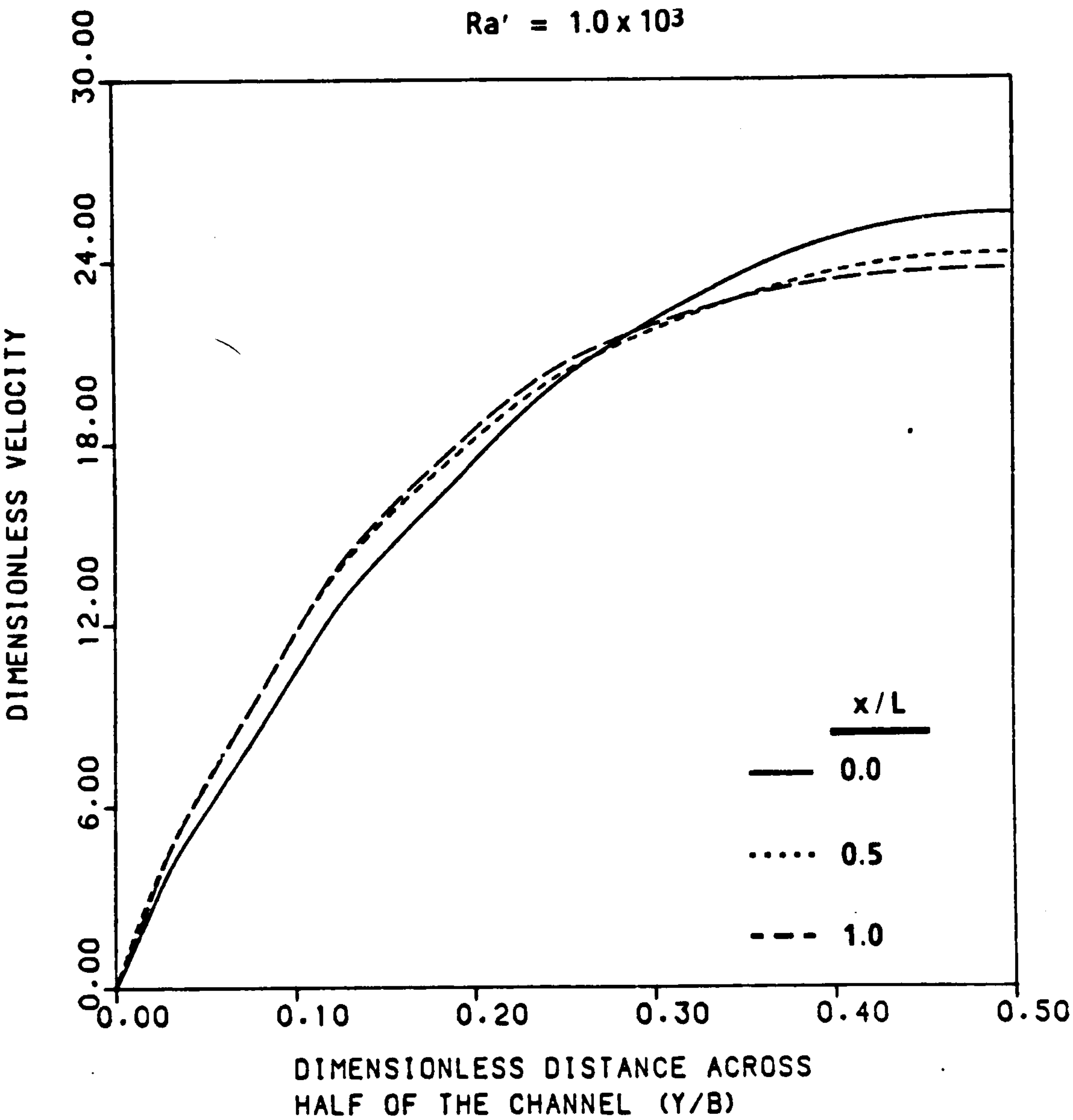

Figure 17. Velocity distributions in an unobstructed vertical channel.

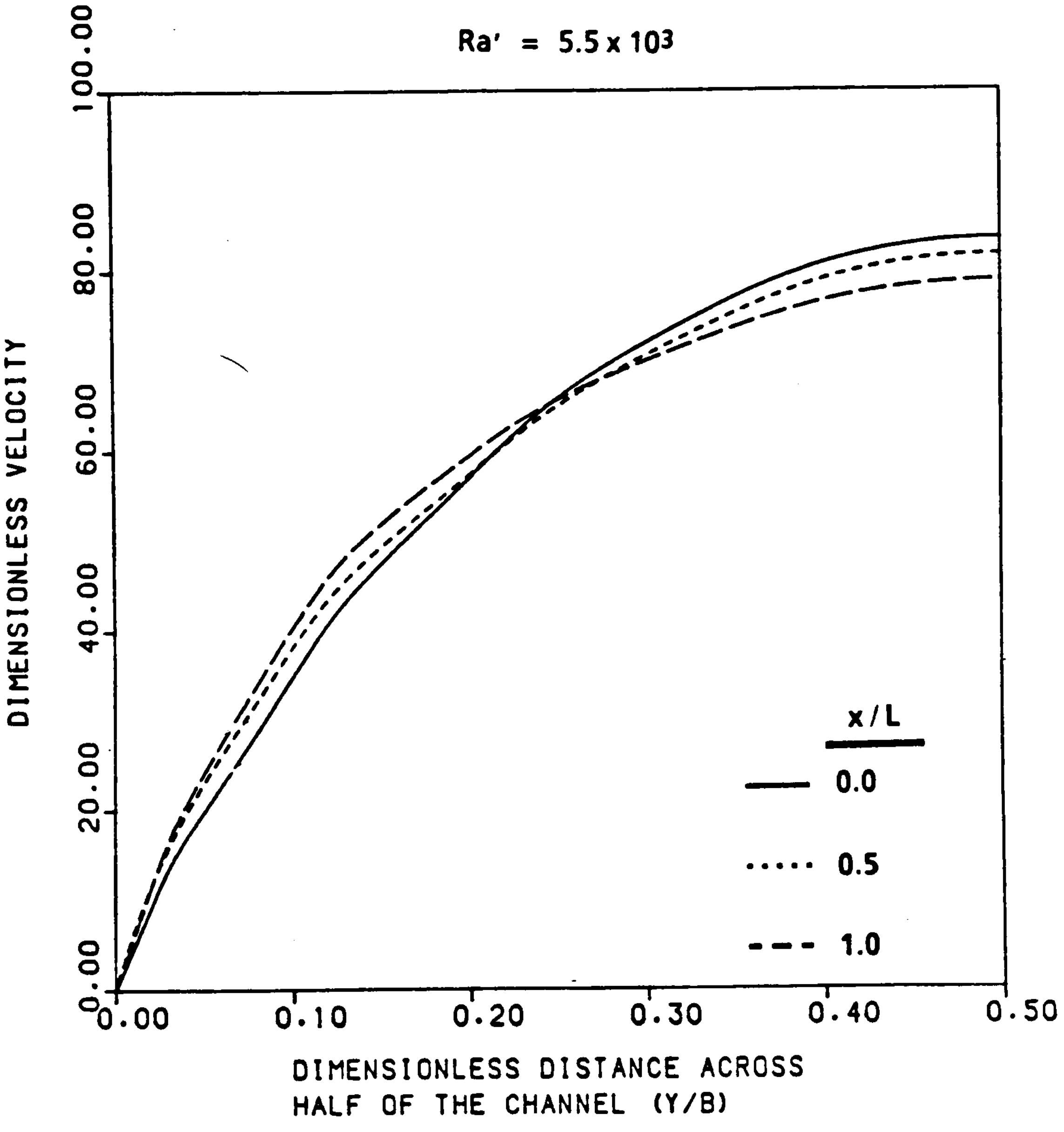

Figure 18. Velocity distributions in an unobstructed vertical channel.

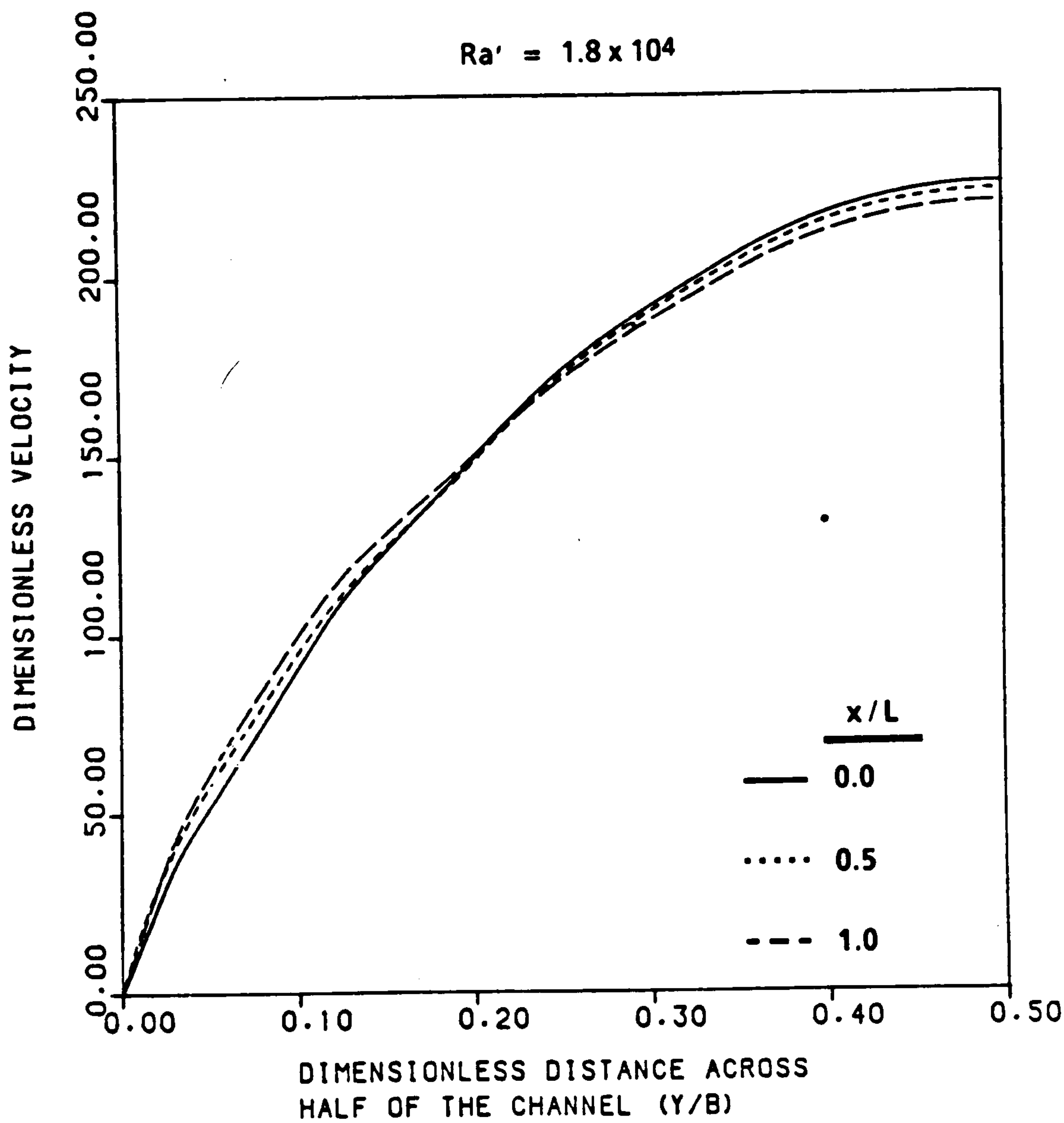

Figure 19. Velocity distributions in an unobstructed vertical channel.

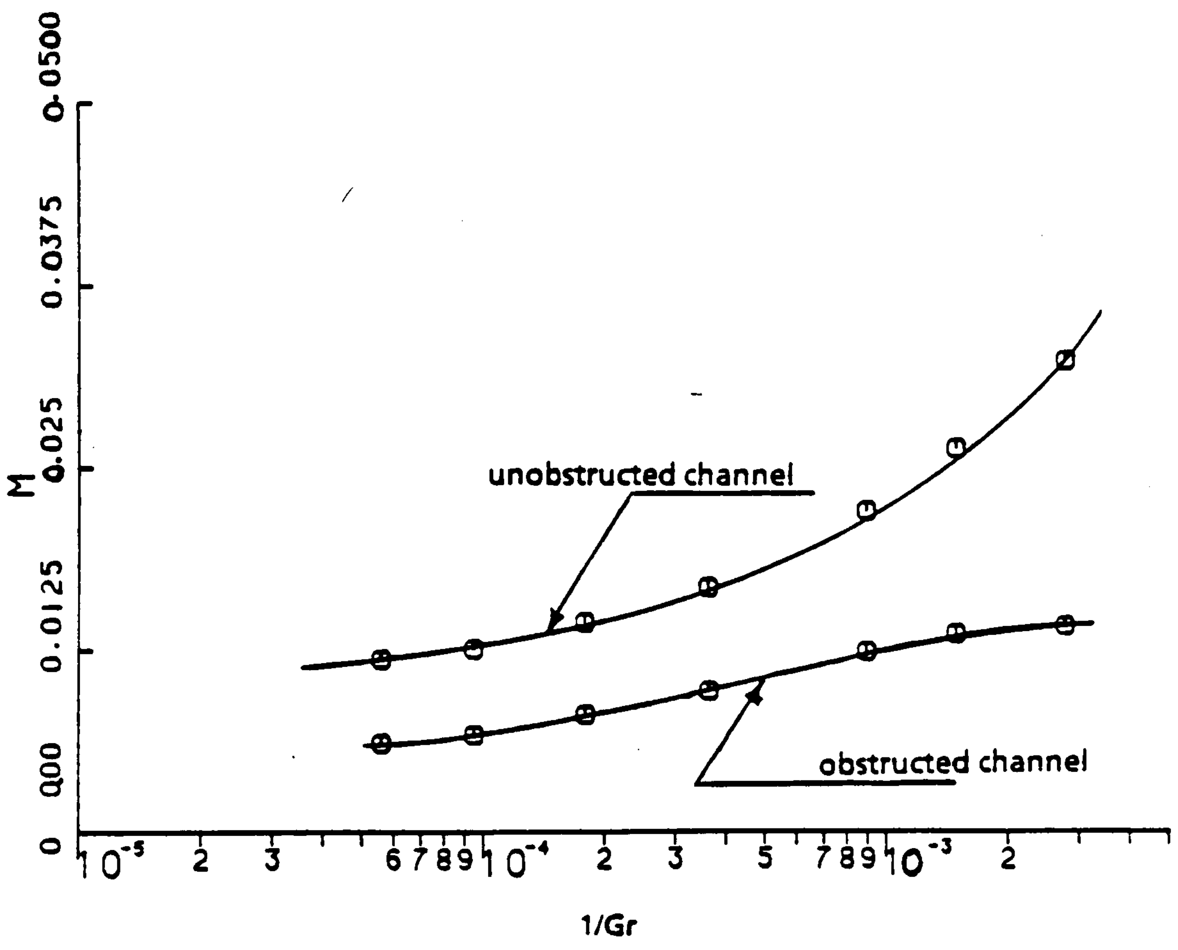

Figure 20. Dimensionless volumetric flow rate (M) versus the inverse of the Grashof number (1/Gr).

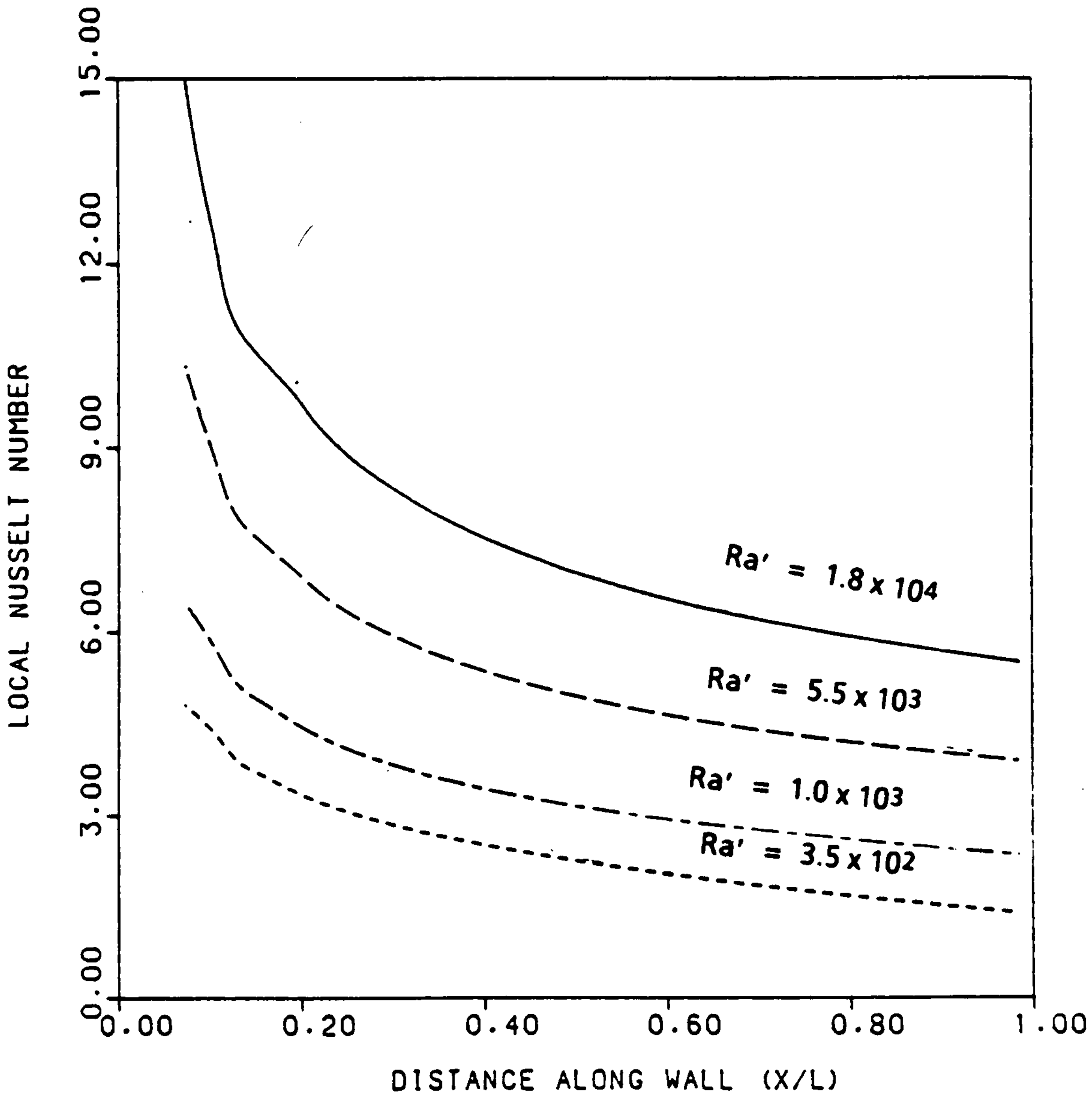

Figure 21. Variation of local Nusselt number with elevation in the channel.

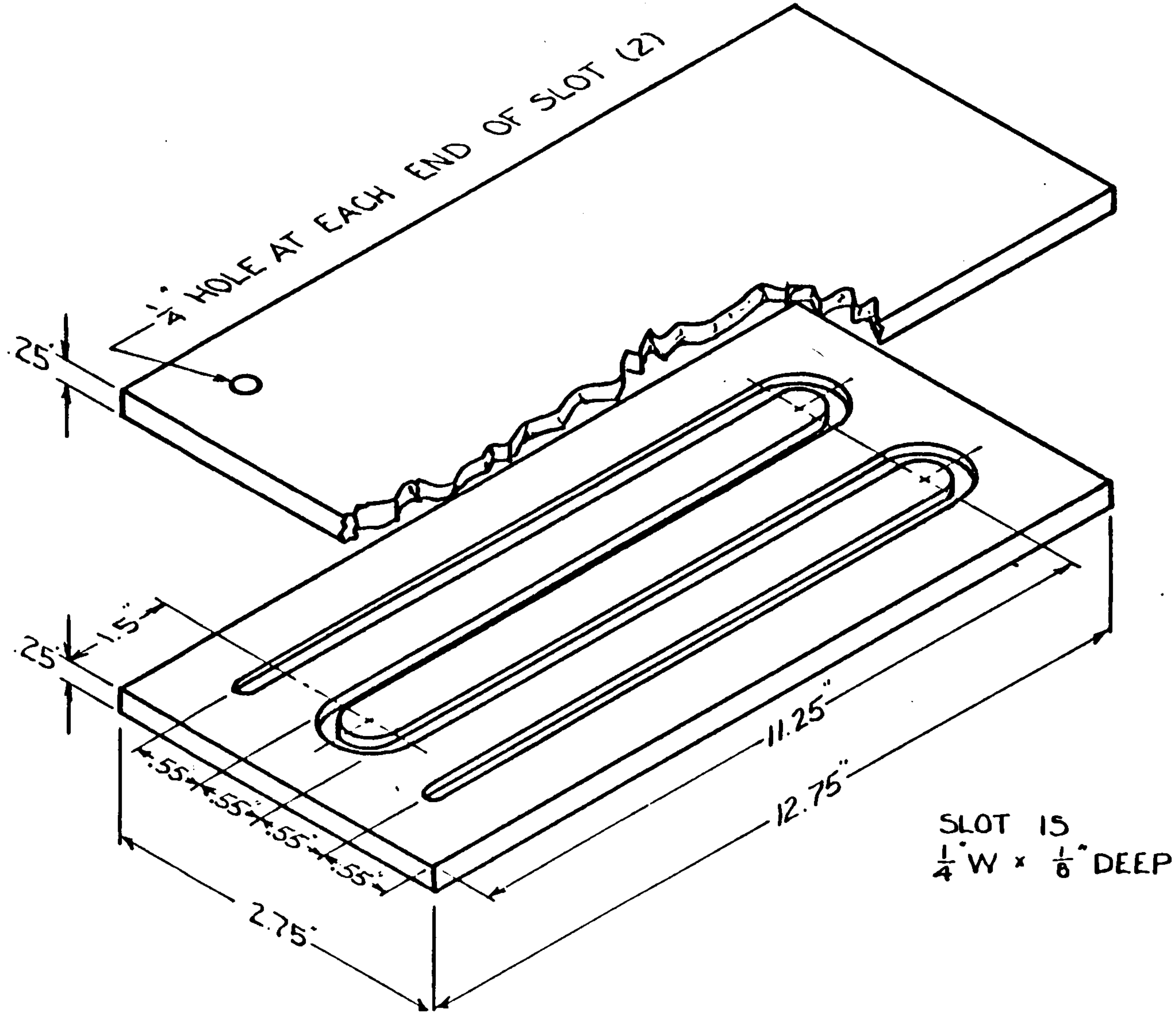

Figure 22. Construction details of isothermal walls.

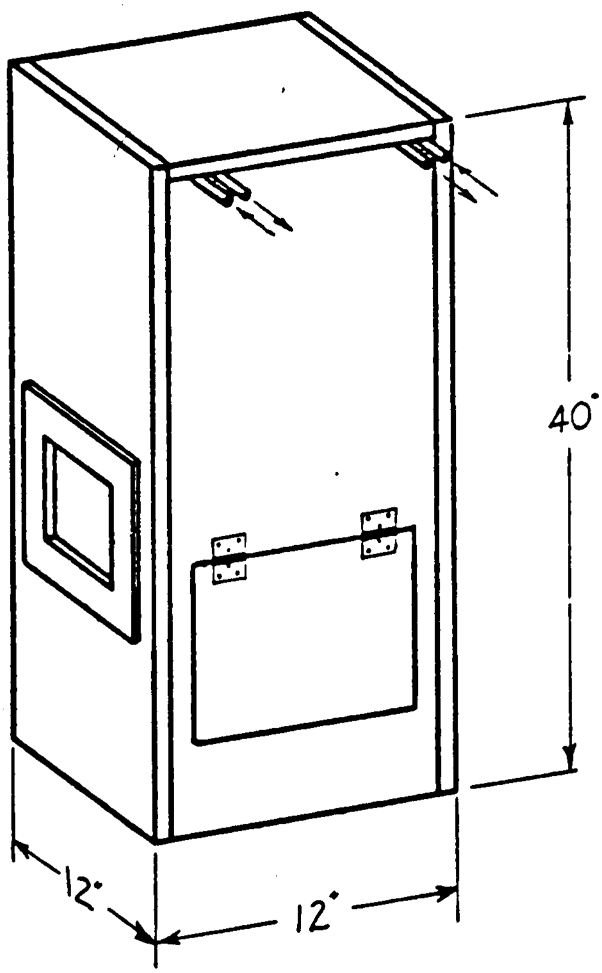

Figure 23. Test chamber.

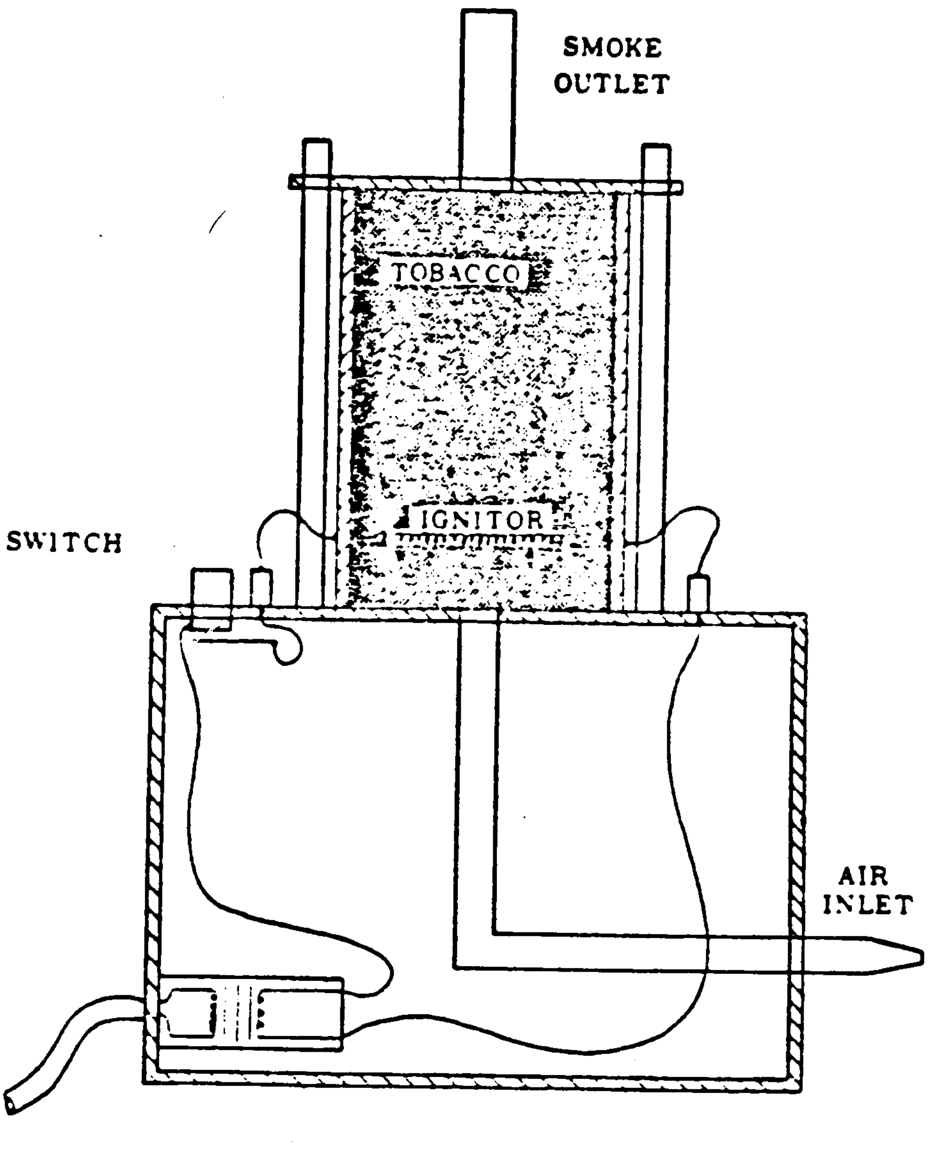

Figure 24. Schematic of smoke generator.

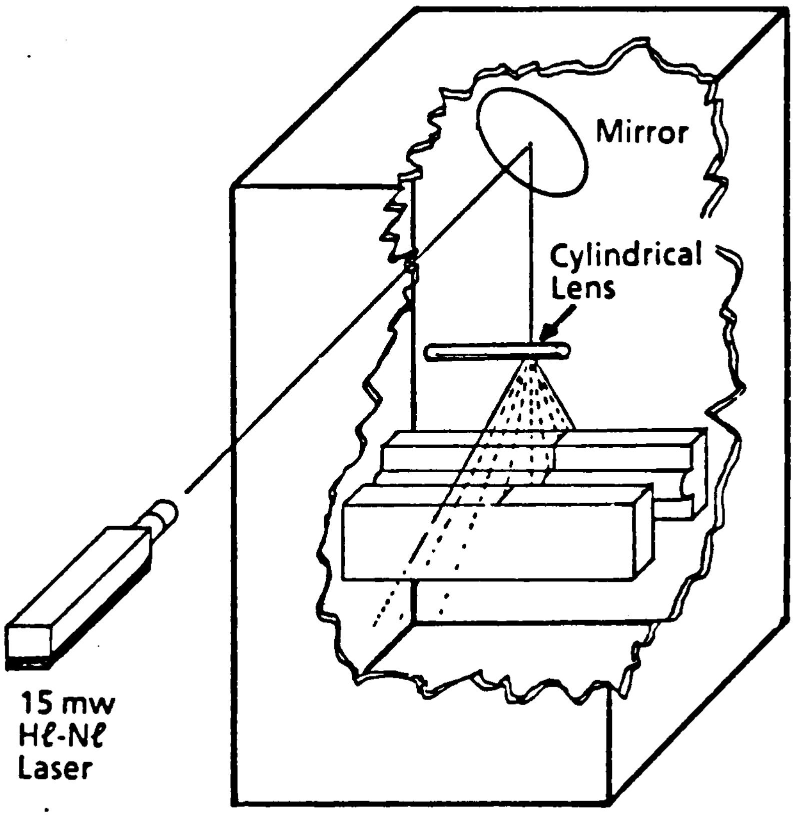

Figure 25. Optical configuration for producing a flat, narrow sheet of light.

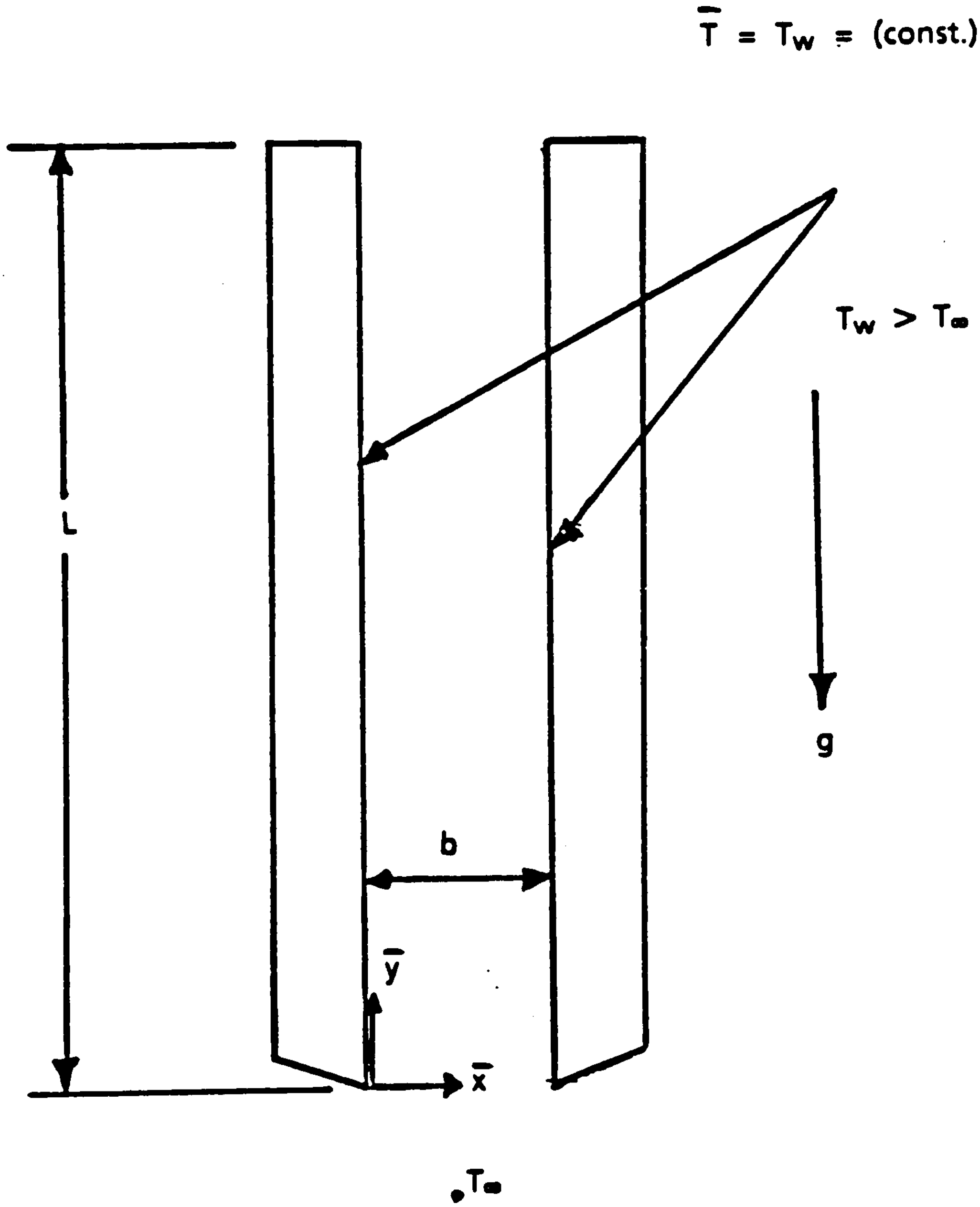

Figure 26. Geometry of the unobstructed channel considered in this investigation.

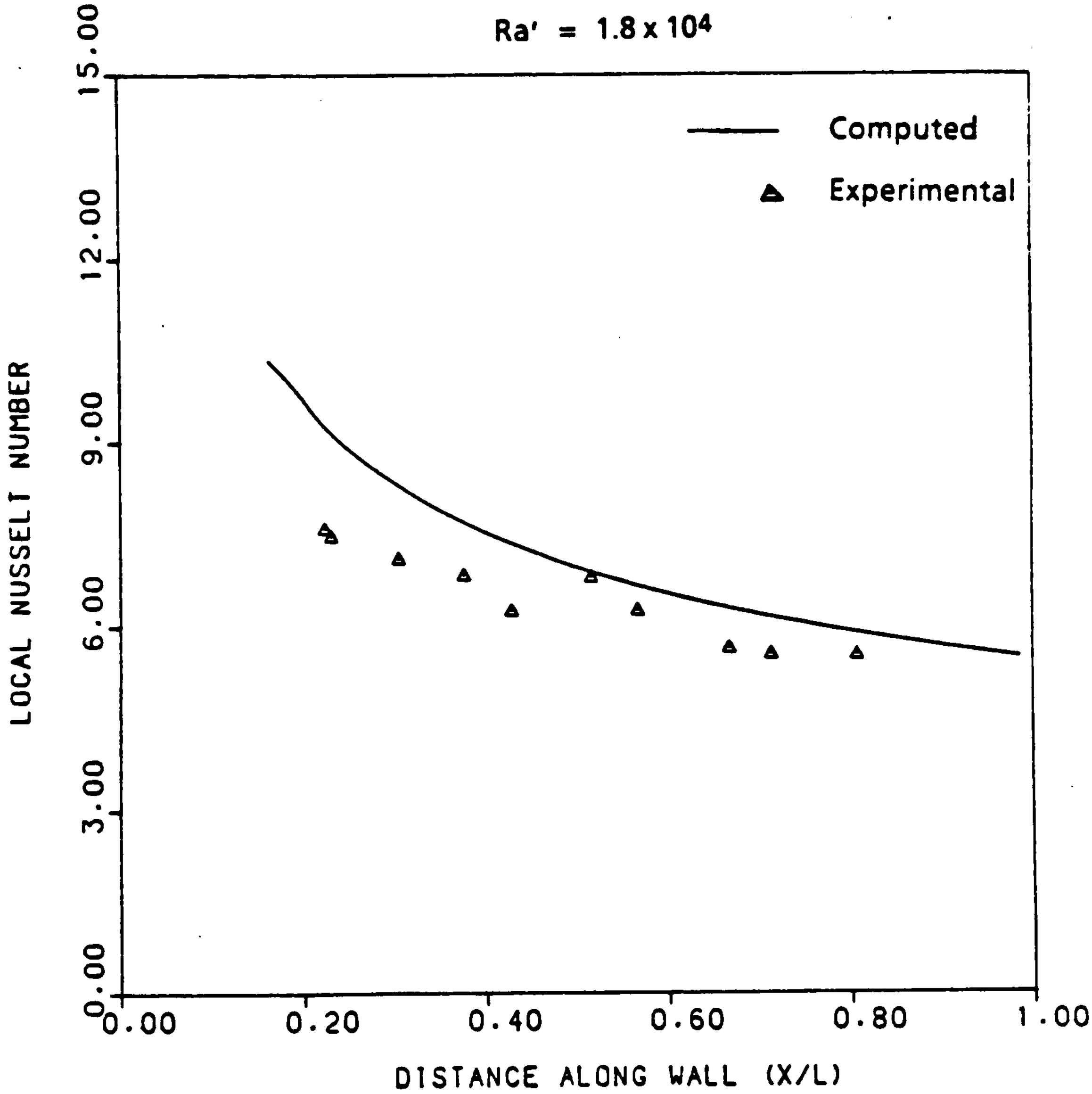

Figure 27. Computed local Nusselt number for the unobstructed channel and comparison with measurements.

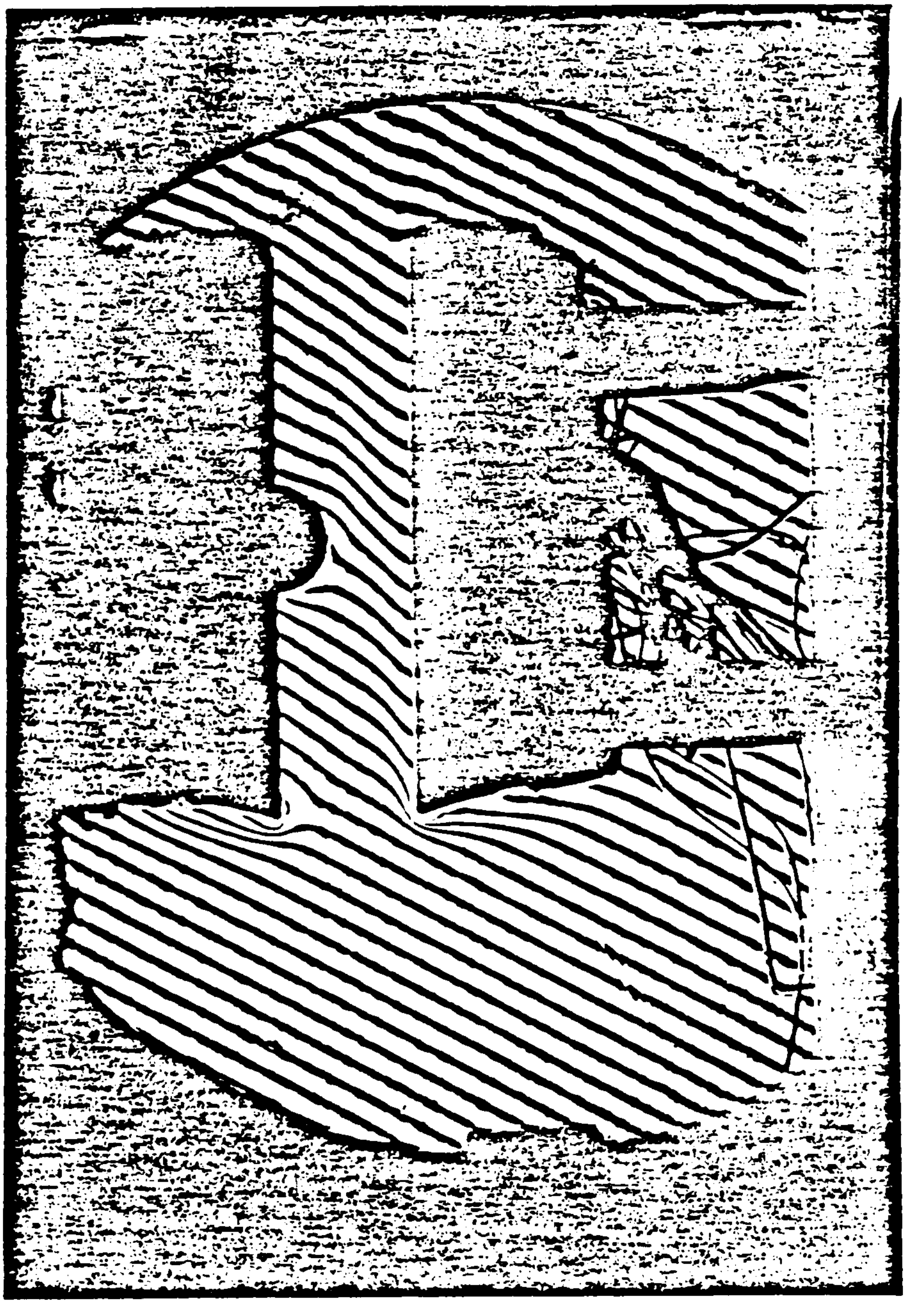

Figure 28. Wollaston Prism Interferometer fringe pattern.

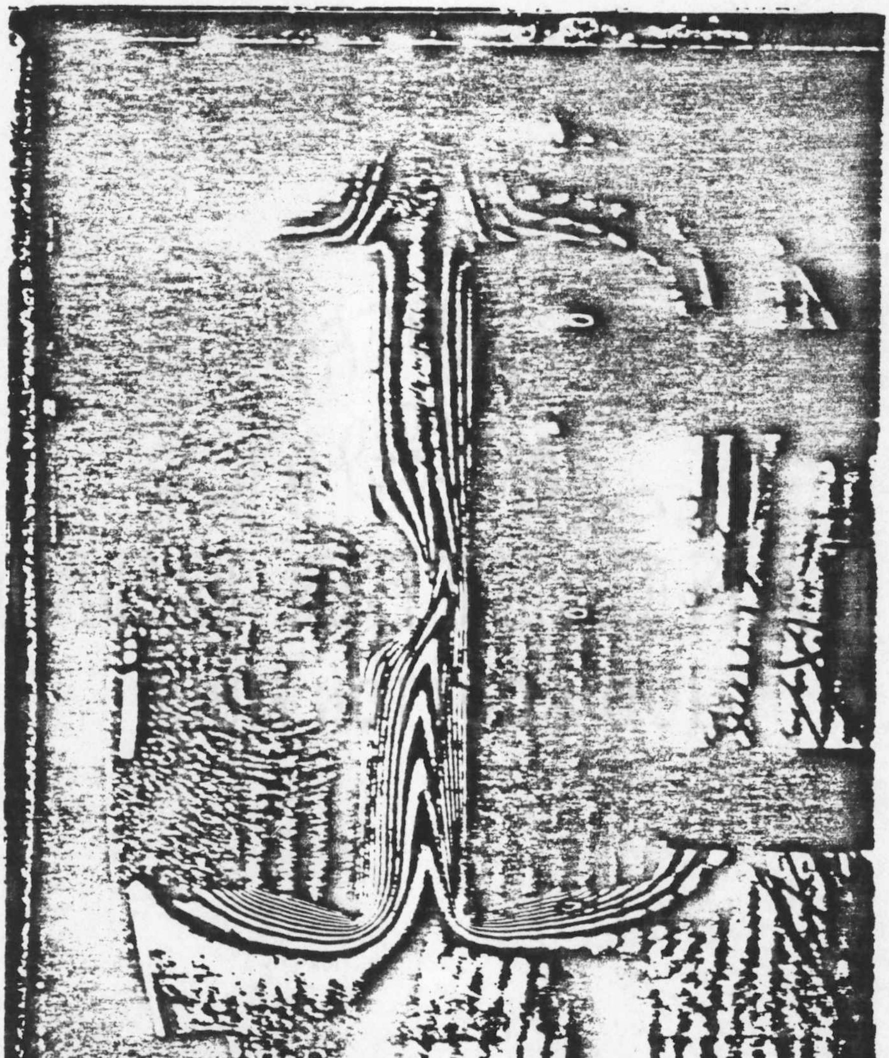

Figure 29. Mach-Zehnder Interferometer infinite fringe pattern.

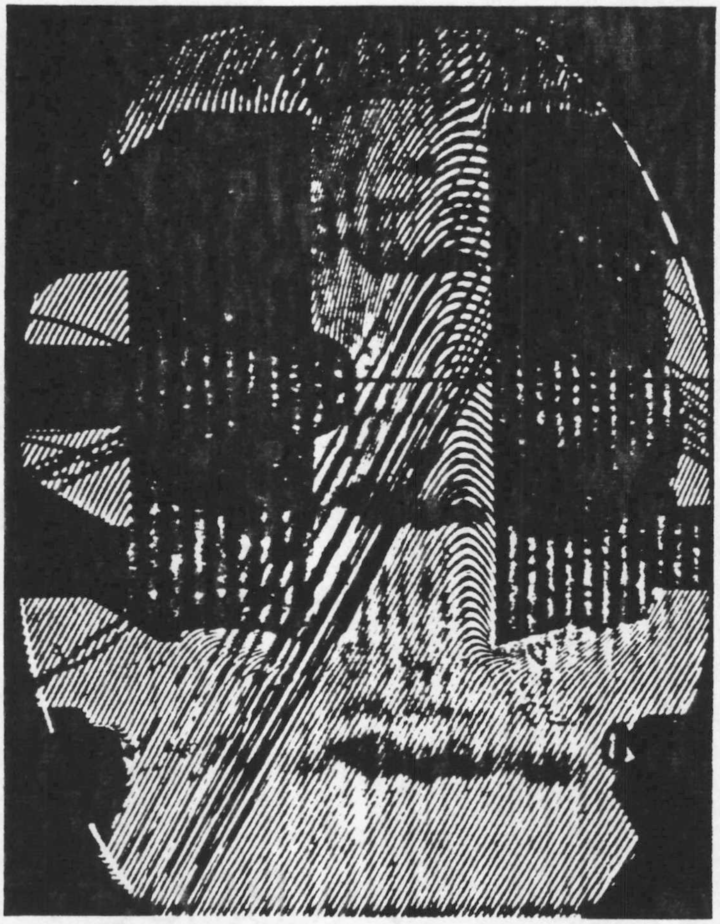

Figure 30. Mach-Zehnder Interferometer
Wedge fringe pattern.

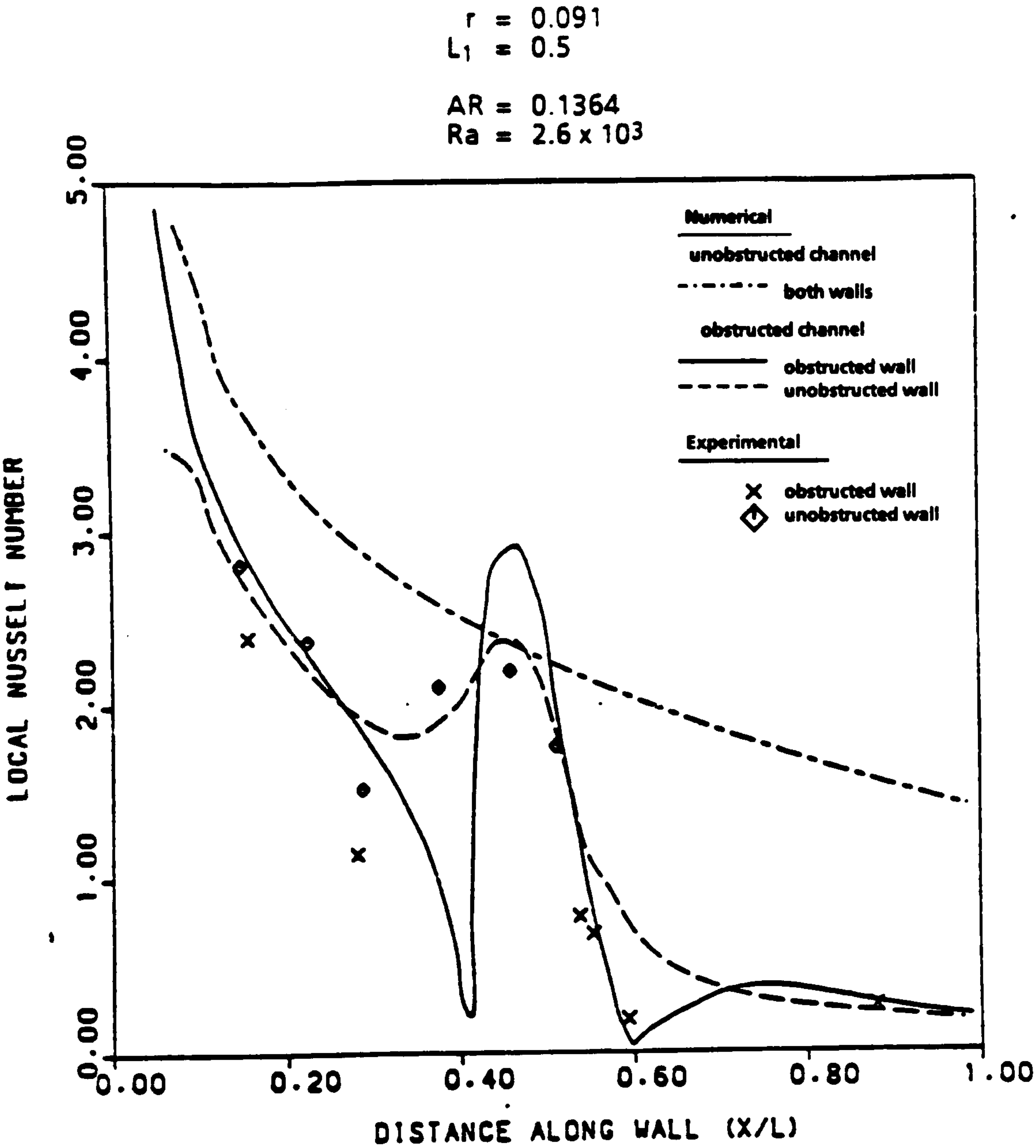

Figure 31. Comparison of numerical and experimental results for the local Nusselt number (N_{ux}).

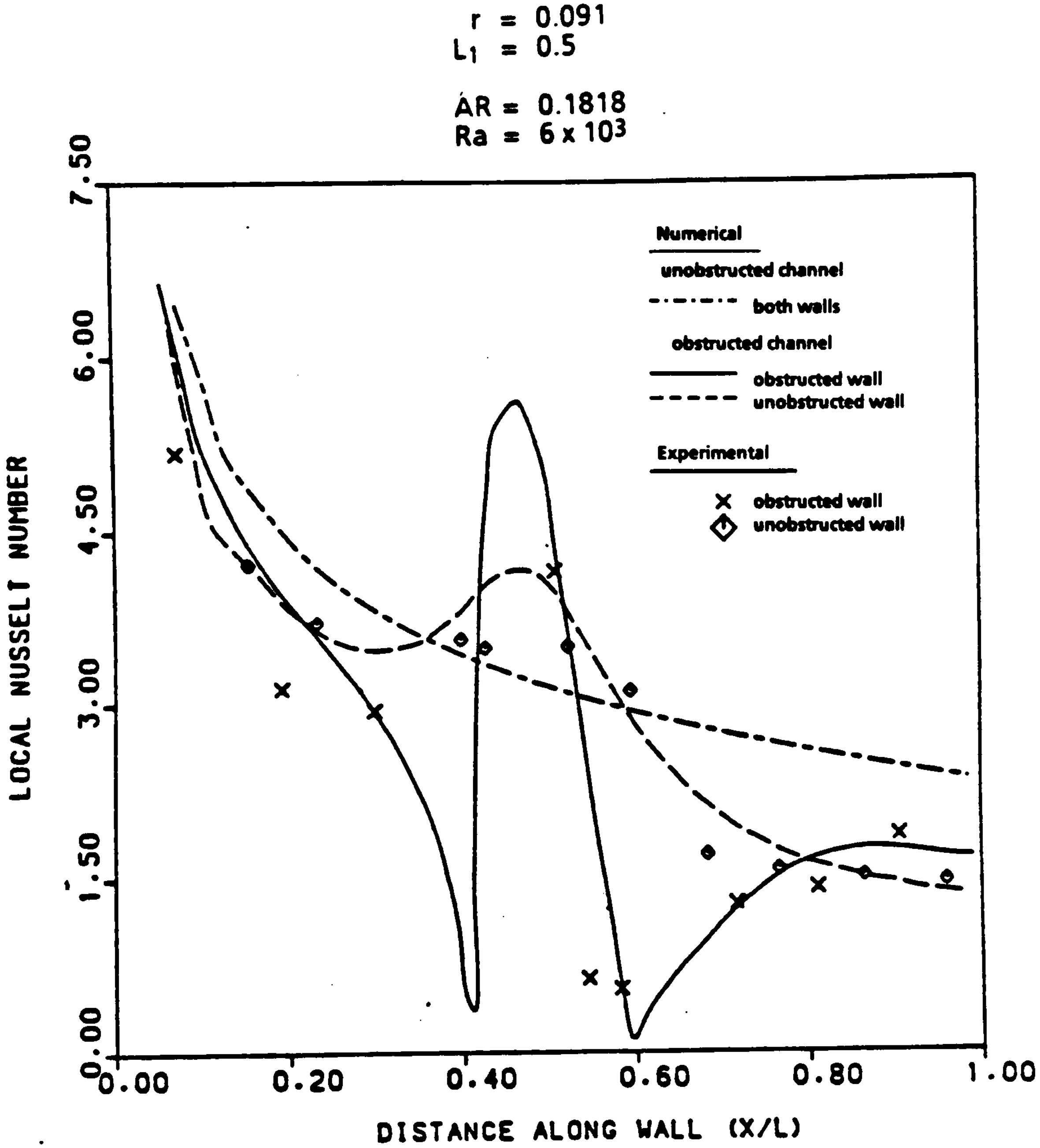

Figure 32. Comparison of numerical and experimental results for the local Nusselt number (N_{ux}).

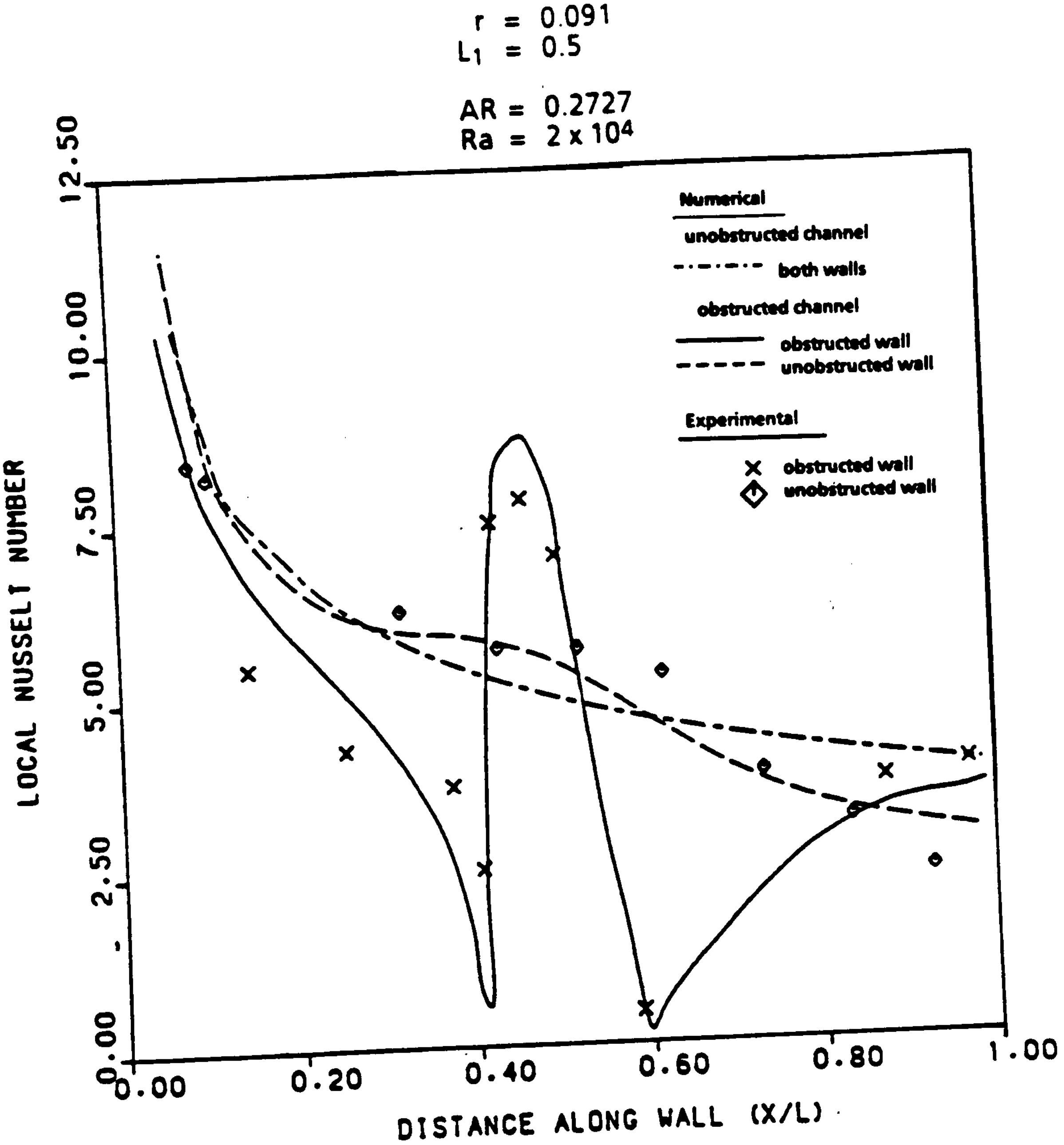

Figure 33. Comparison of numerical and experimental results for the local Nusselt number (N_{ux}).

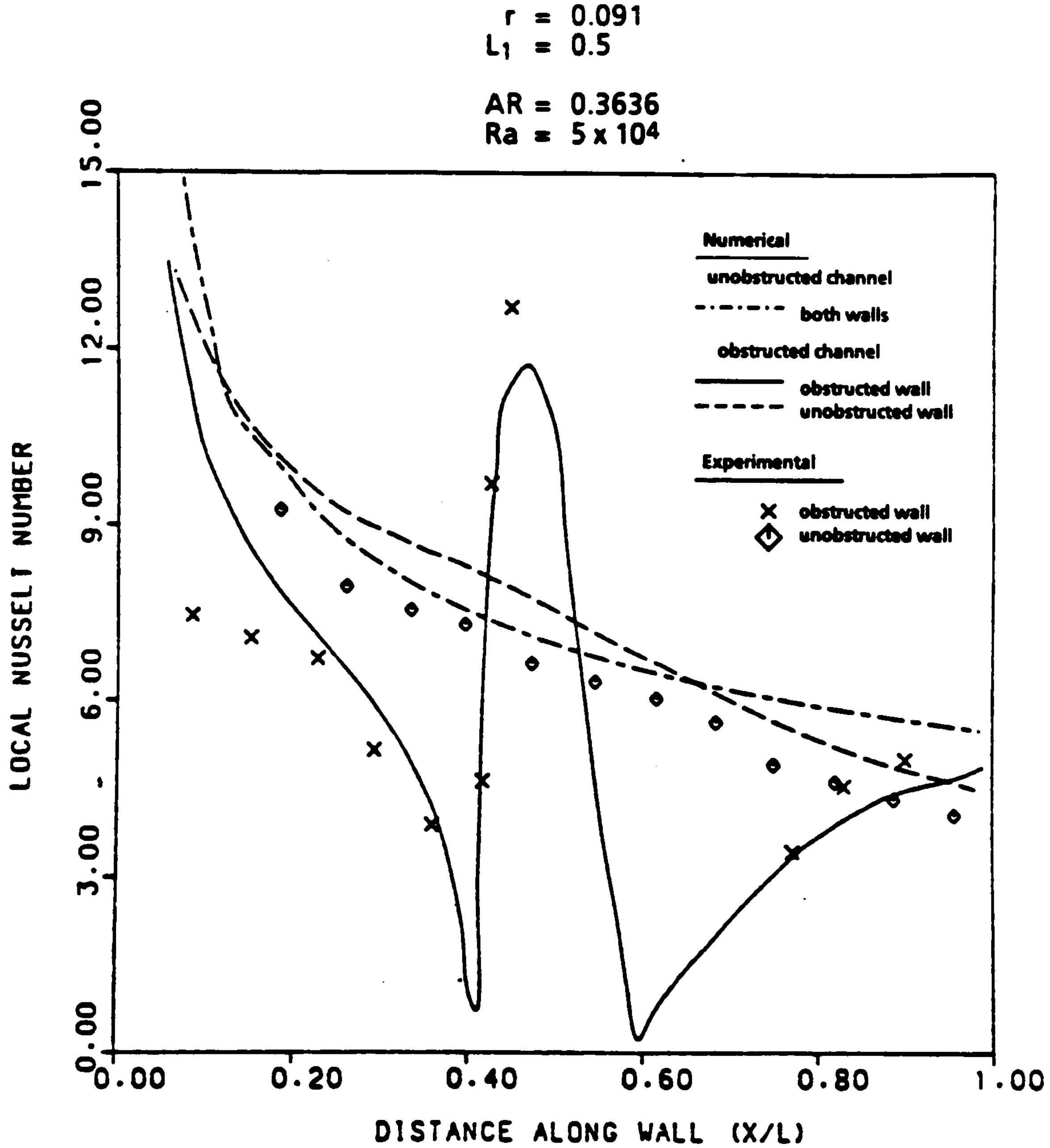

Figure 34. Comparison of numerical and experimental results for the local Nusselt number (N_{ux}).

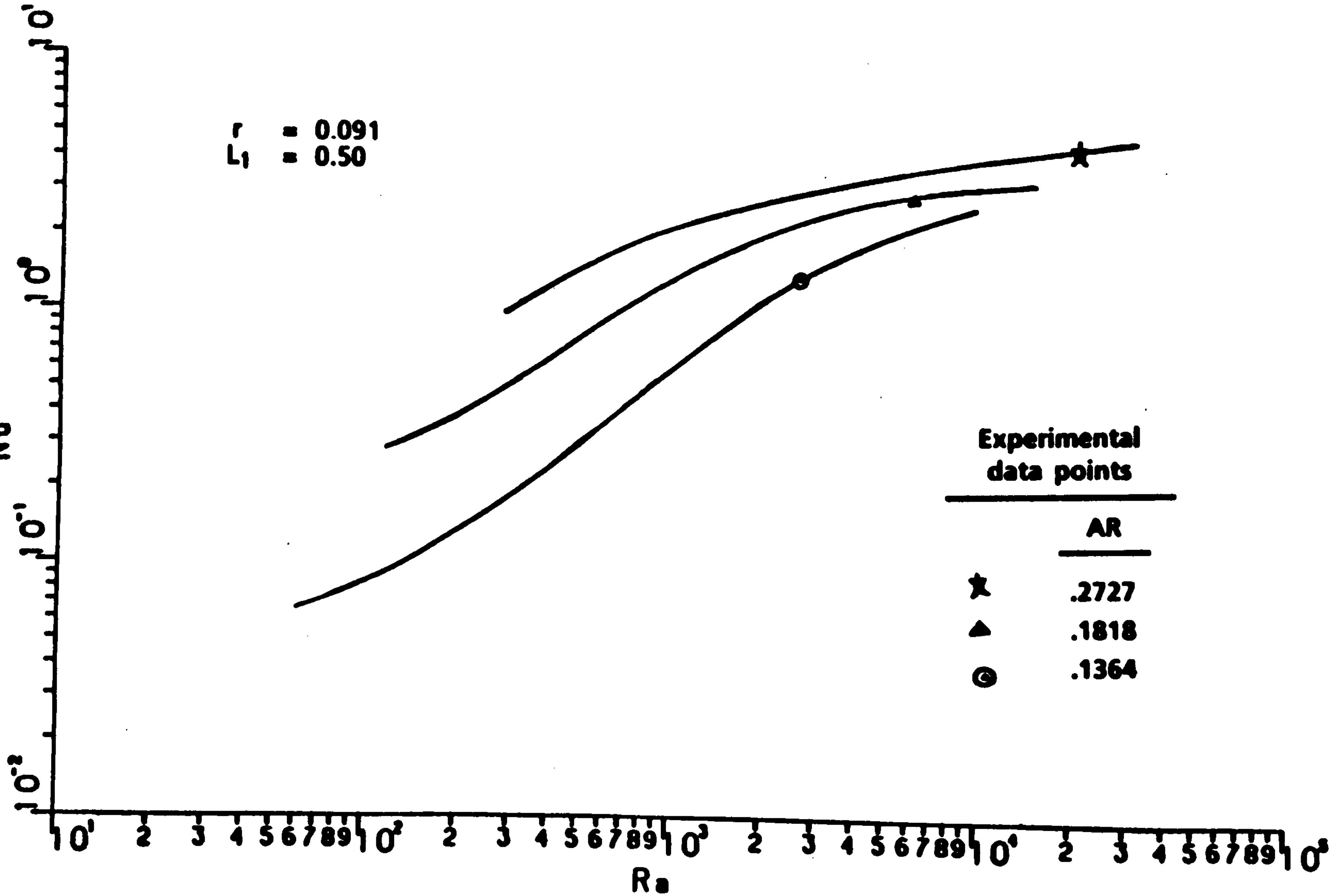

Figure 35. Comparison of the computed and measured Nusselt numbers for the obstructed channel.

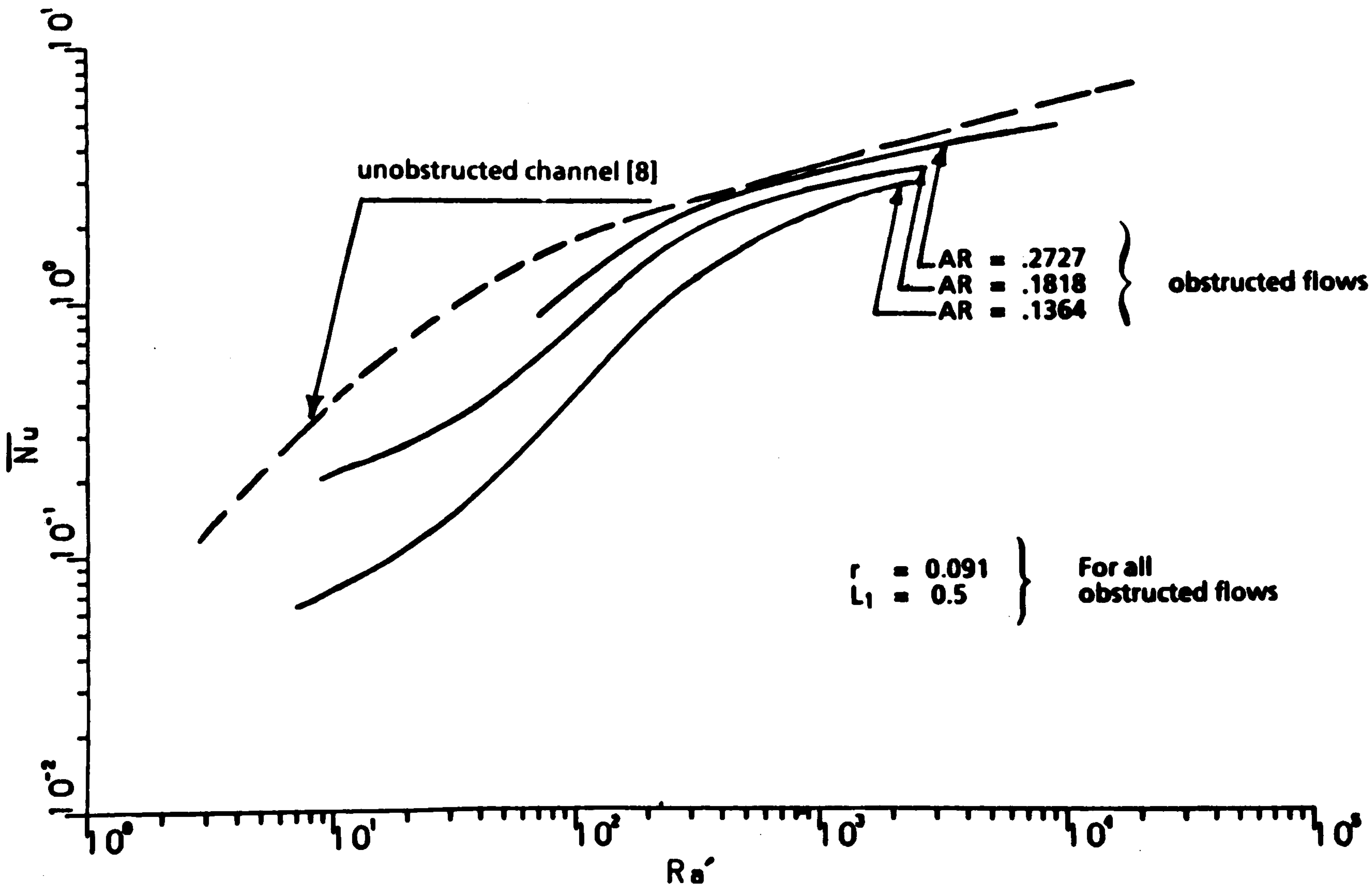

Figure 36. Comparison of the computed average Nusselt numbers for the obstructed and unobstructed channel flows.

$r = 0.091$
$L_1 = 0.5$

$AR = 0.1364$

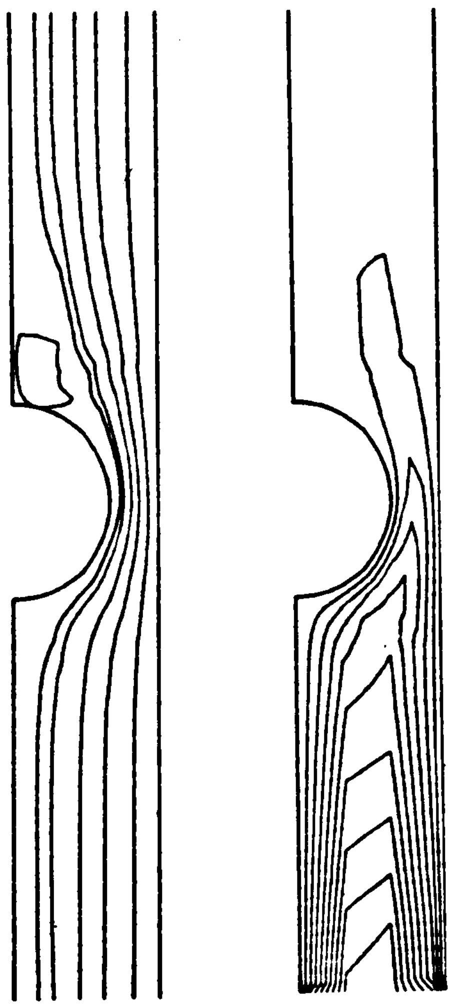

(a) streamlines (b) isotherms

Figure 37. Computed streamlines and isotherms for $Ra = 2.6 \times 10^3$

$r = 0.091$
$L_1 = 0.5$

$AR = 0.1818$

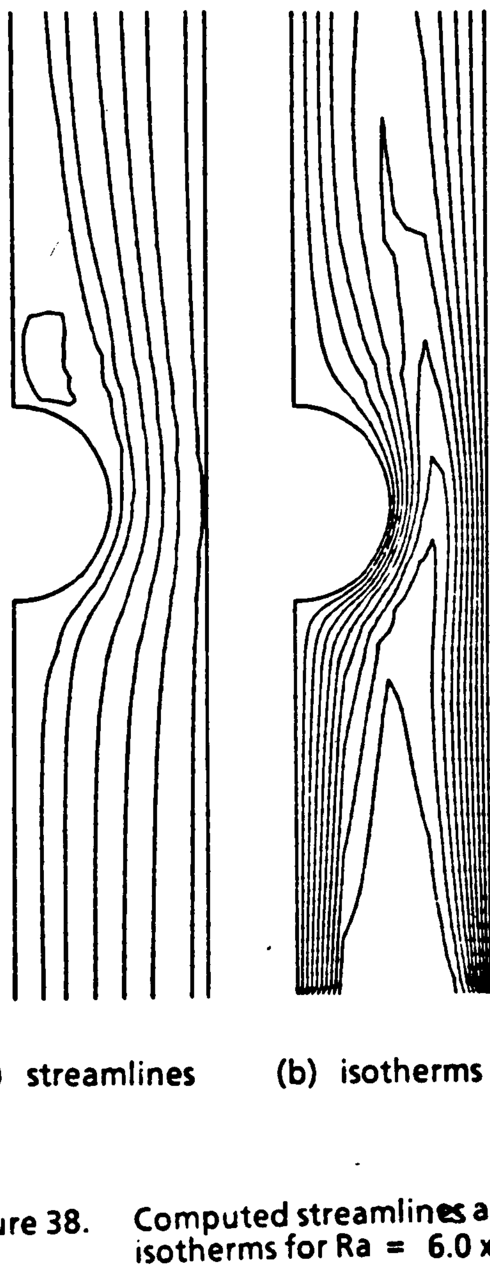

(a) streamlines (b) isotherms

Figure 38. Computed streamlines and isotherms for $Ra = 6.0 \times 10^3$

$r = 0.091$
$L_1 = 0.5$

$AR = 0.2727$

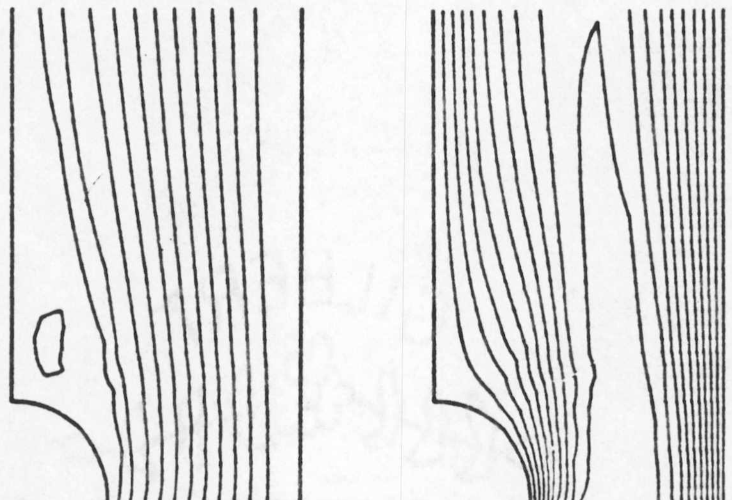

(a) streamlines (b) isotherms

Figure 39. Computed streamlines and isotherms for $Ra = 2.0 \times 10^4$

$r = 0.091$
$L_1 = 0.5$

$AR = 0.3636$

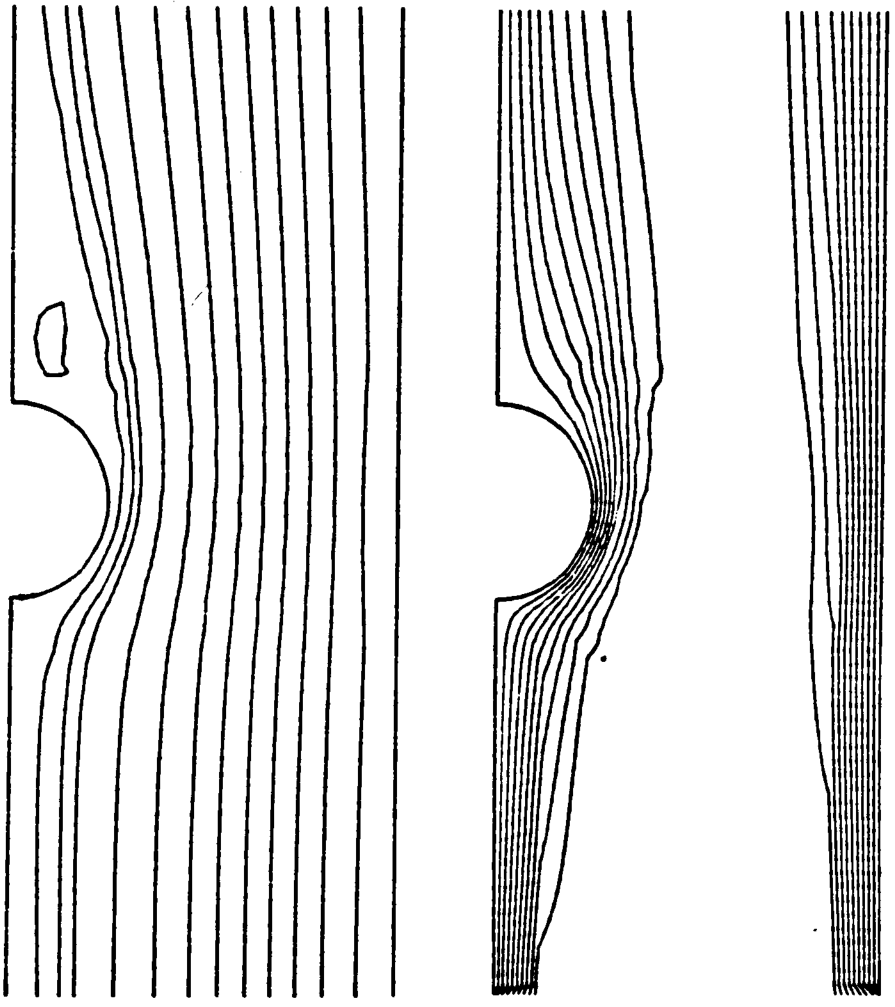

(a) streamlines (b) isotherms

Figure 40. Computed streamlines and isotherms for $Ra = 5.0 \times 10^4$

$r = 0.091$
$L_1 = 0.5$
$AR = 0.1818$

Figure 41. Mach-Zehnder interferogram (infinite fringe setting) for $Ra = 6.0 \times 10^3$

$r = 0.091$
$L_1 = 0.5$
$AR = 0.3636$

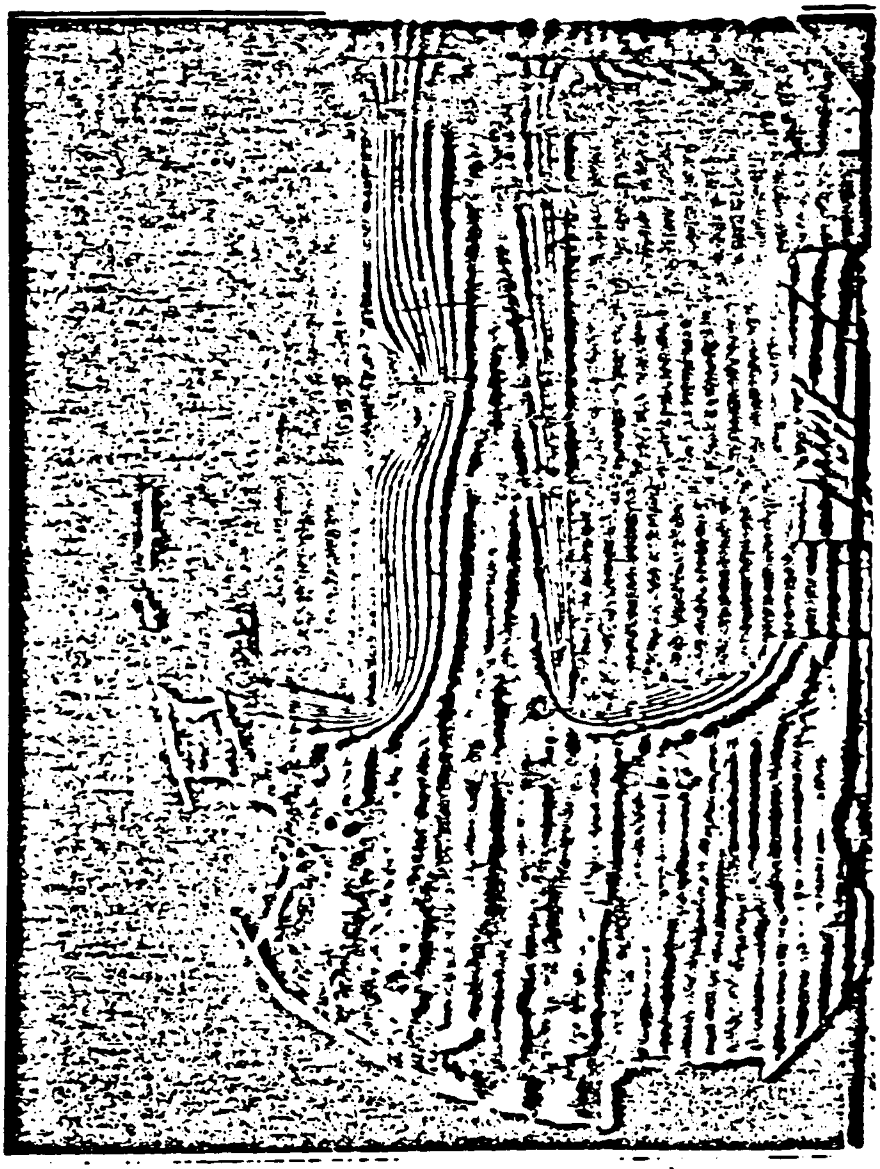

Figure 42. Mach-Zehnder interferogram (infinite fringe setting) for $Ra = 5.0 \times 10^4$

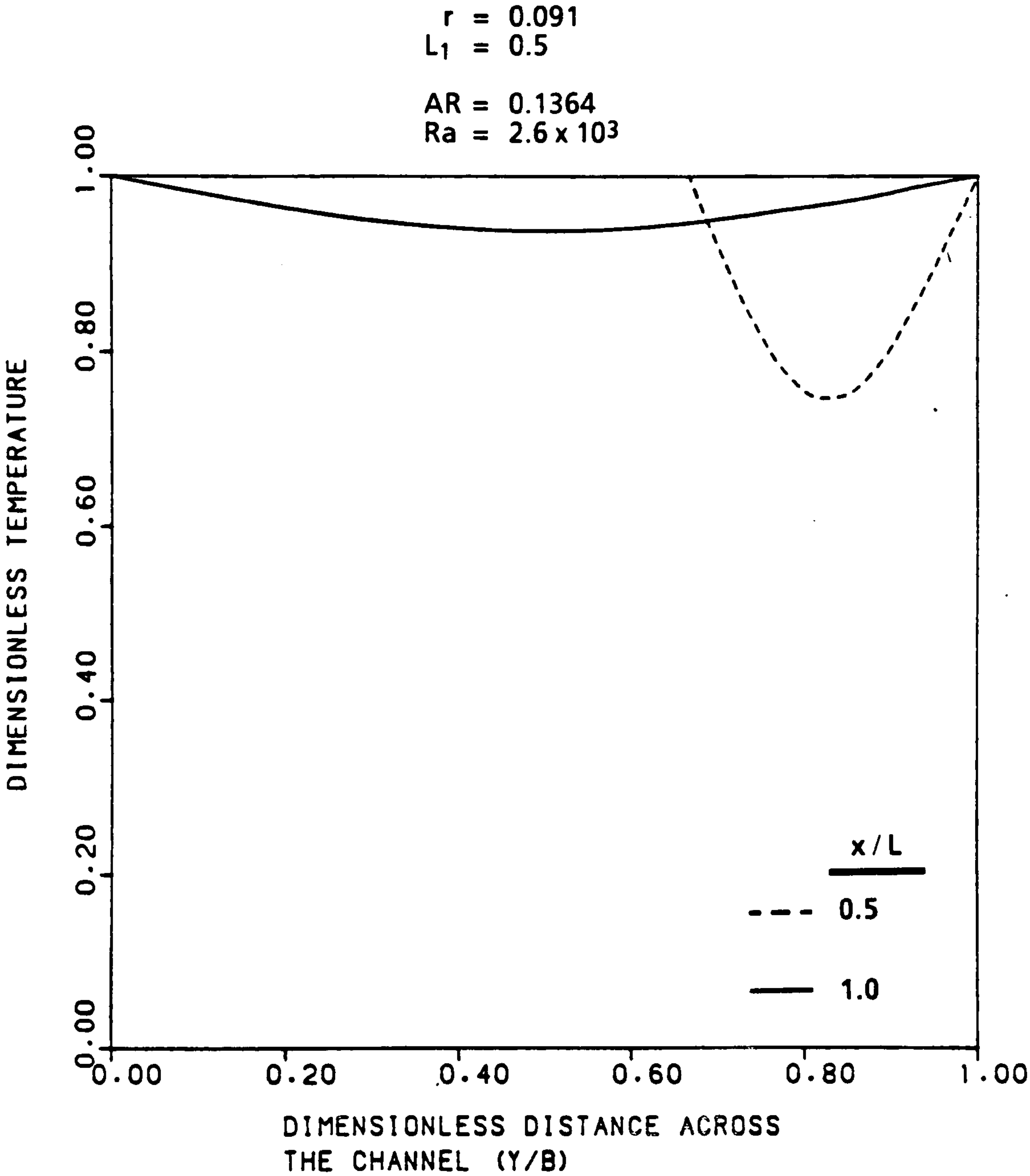

Figure 43. Transverse temperature distributions in the obstructed channel.

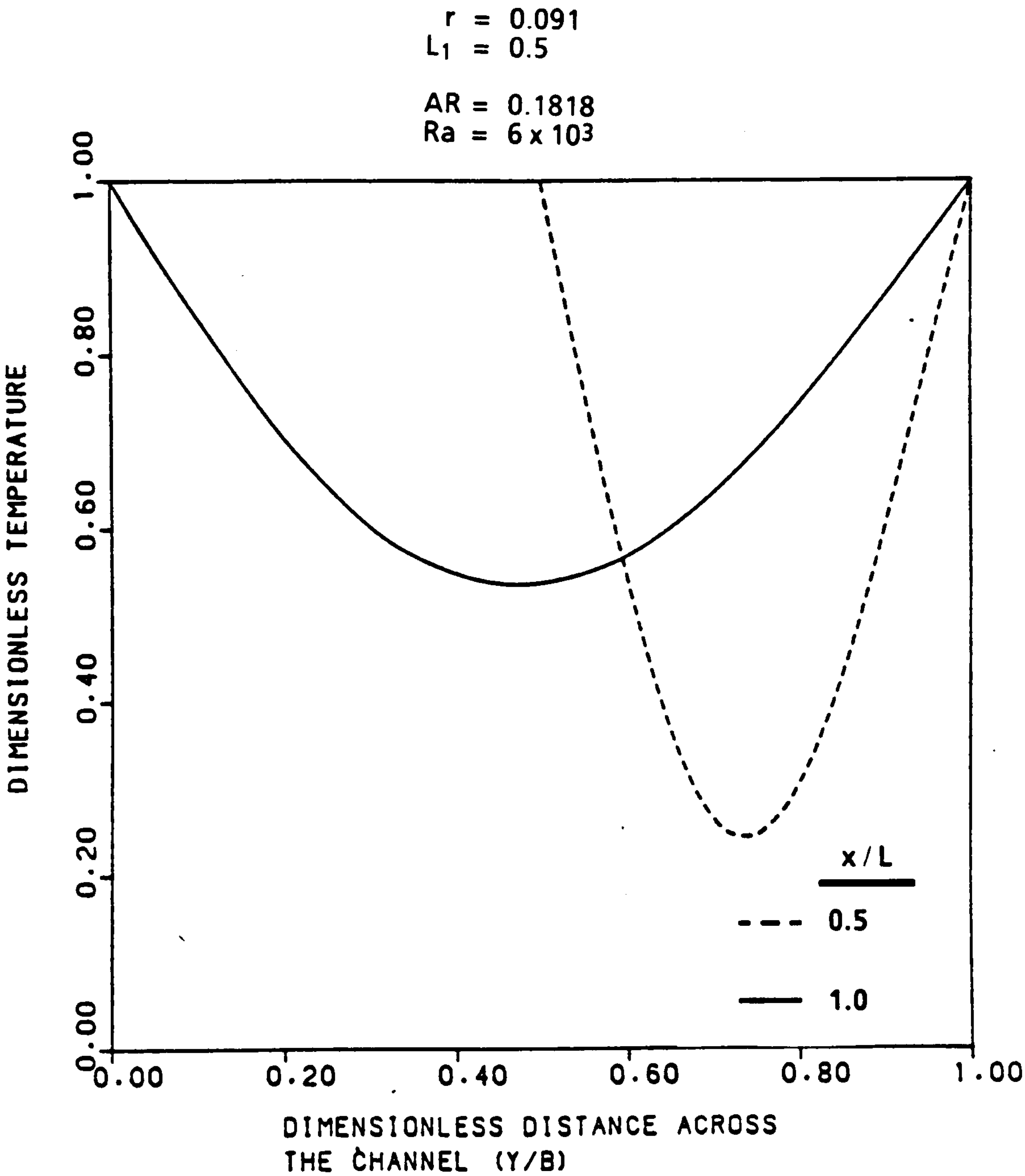

Figure 44. Transverse temperature distributions in the obstructed channel.

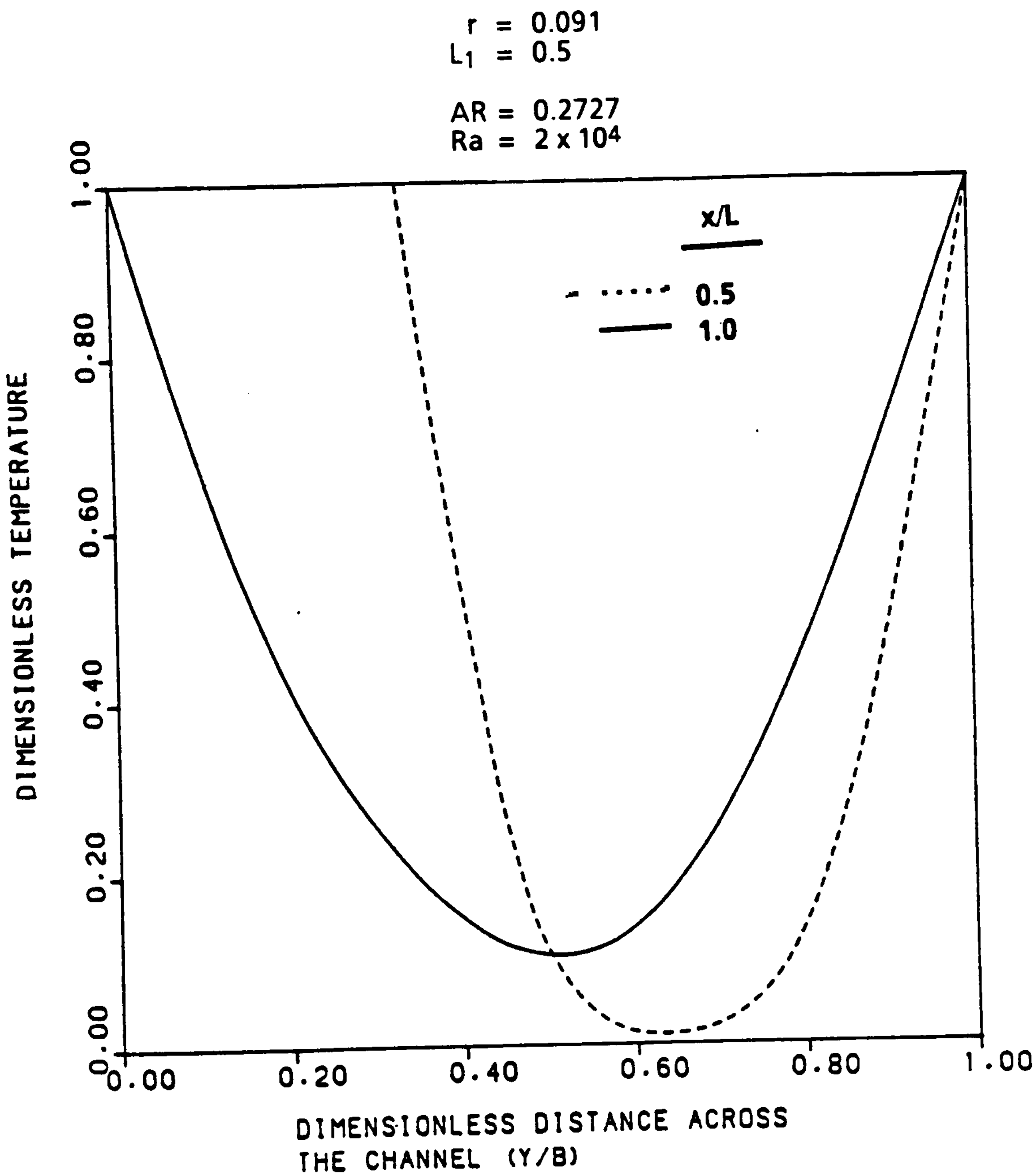

Figure 45. Transverse temperature distributions in the obstructed channel.

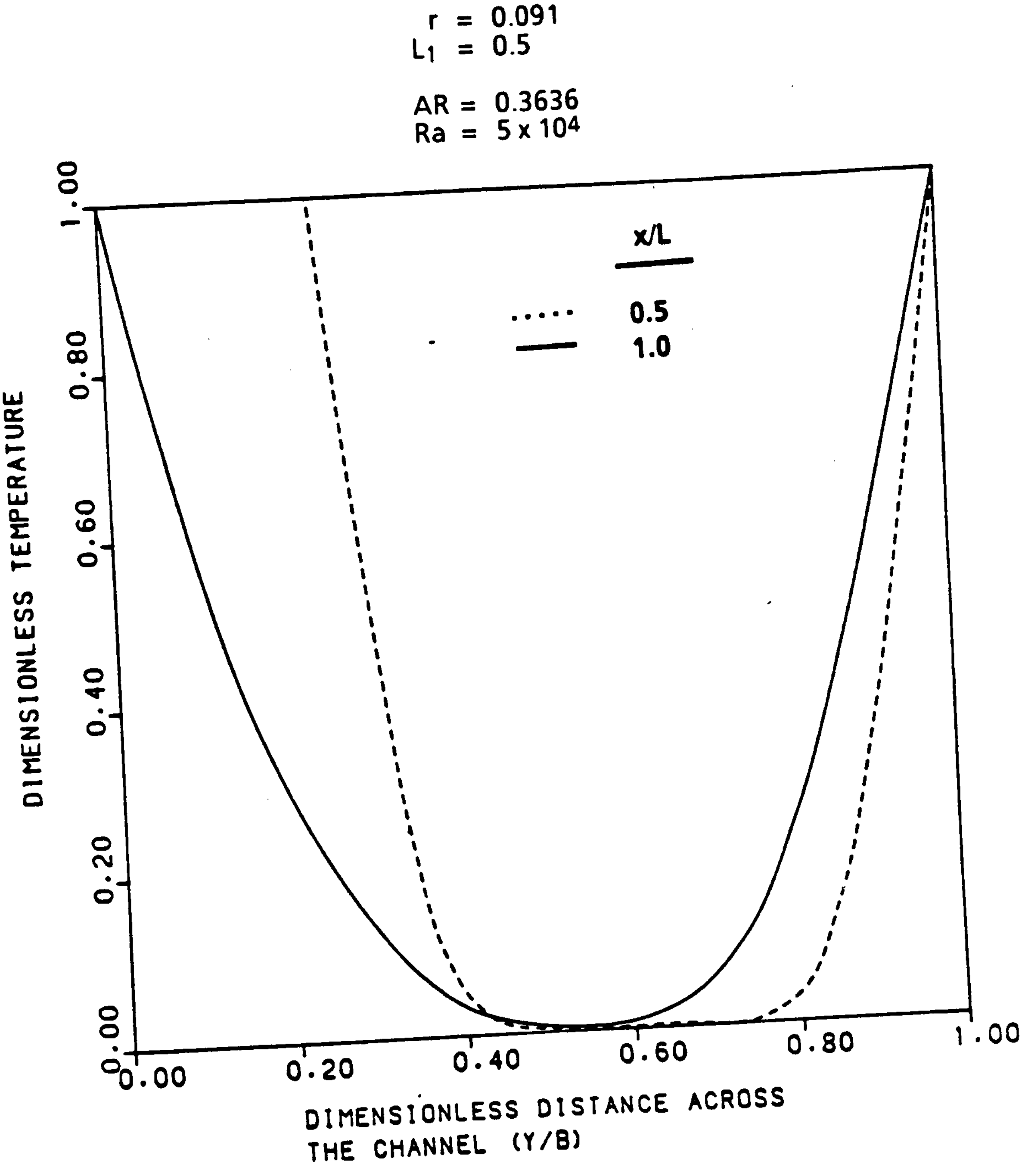

Figure 46. Transverse temperature distributions in the obstructed channel.

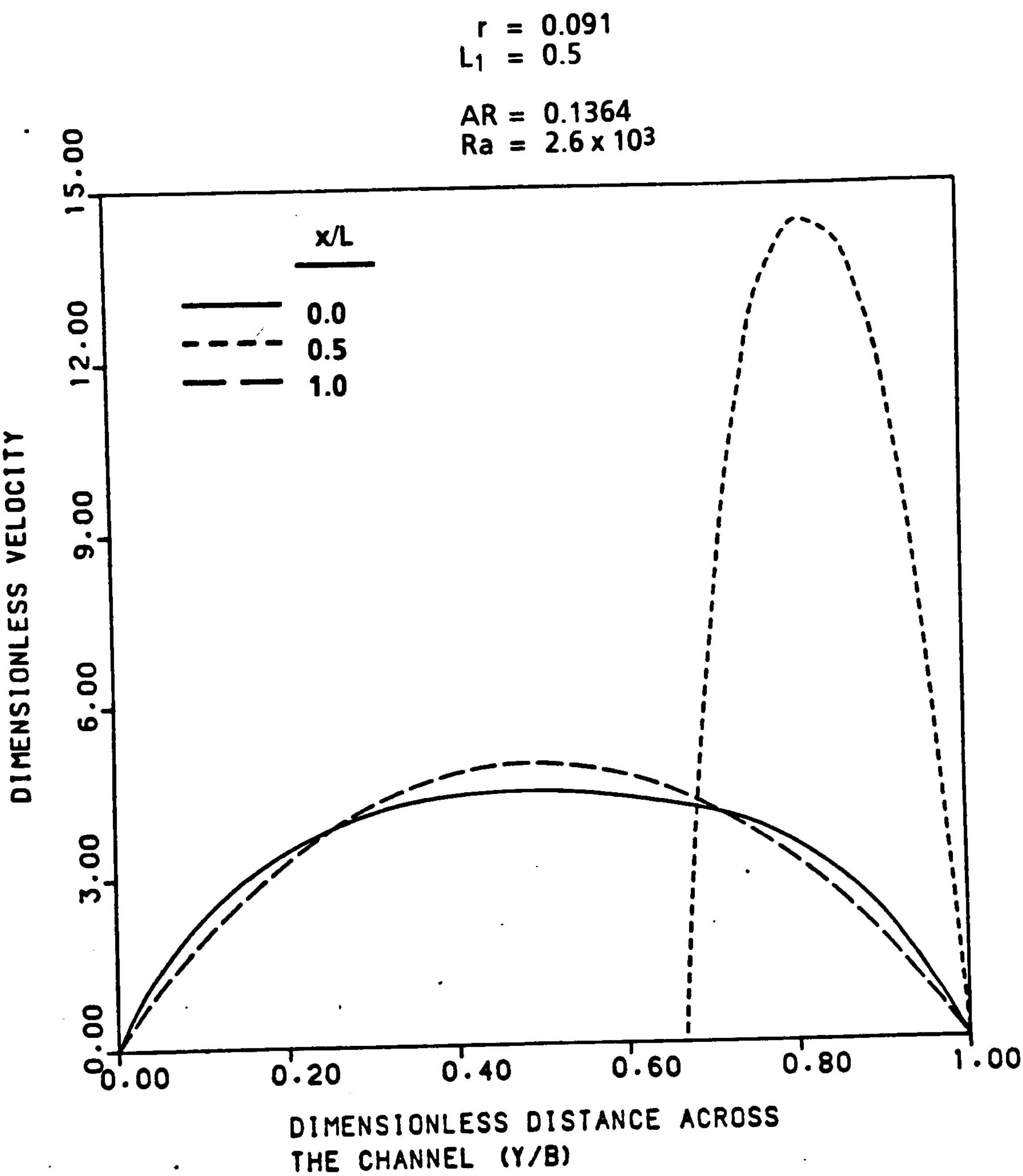

Figure 47. Transverse velocity distributions in the obstructed channel.

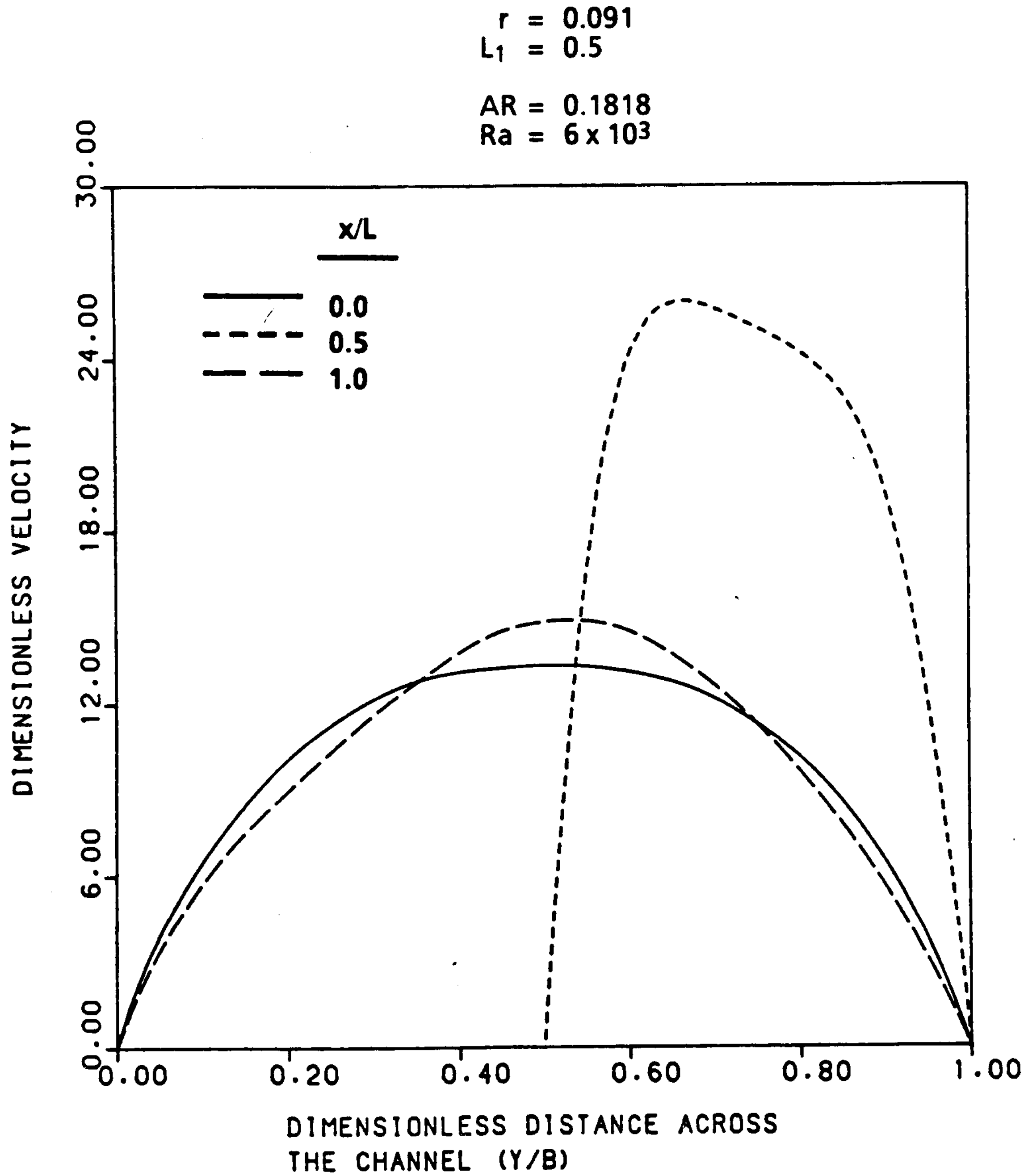

Figure 48. Transverse velocity distributions in the obstructed channel.

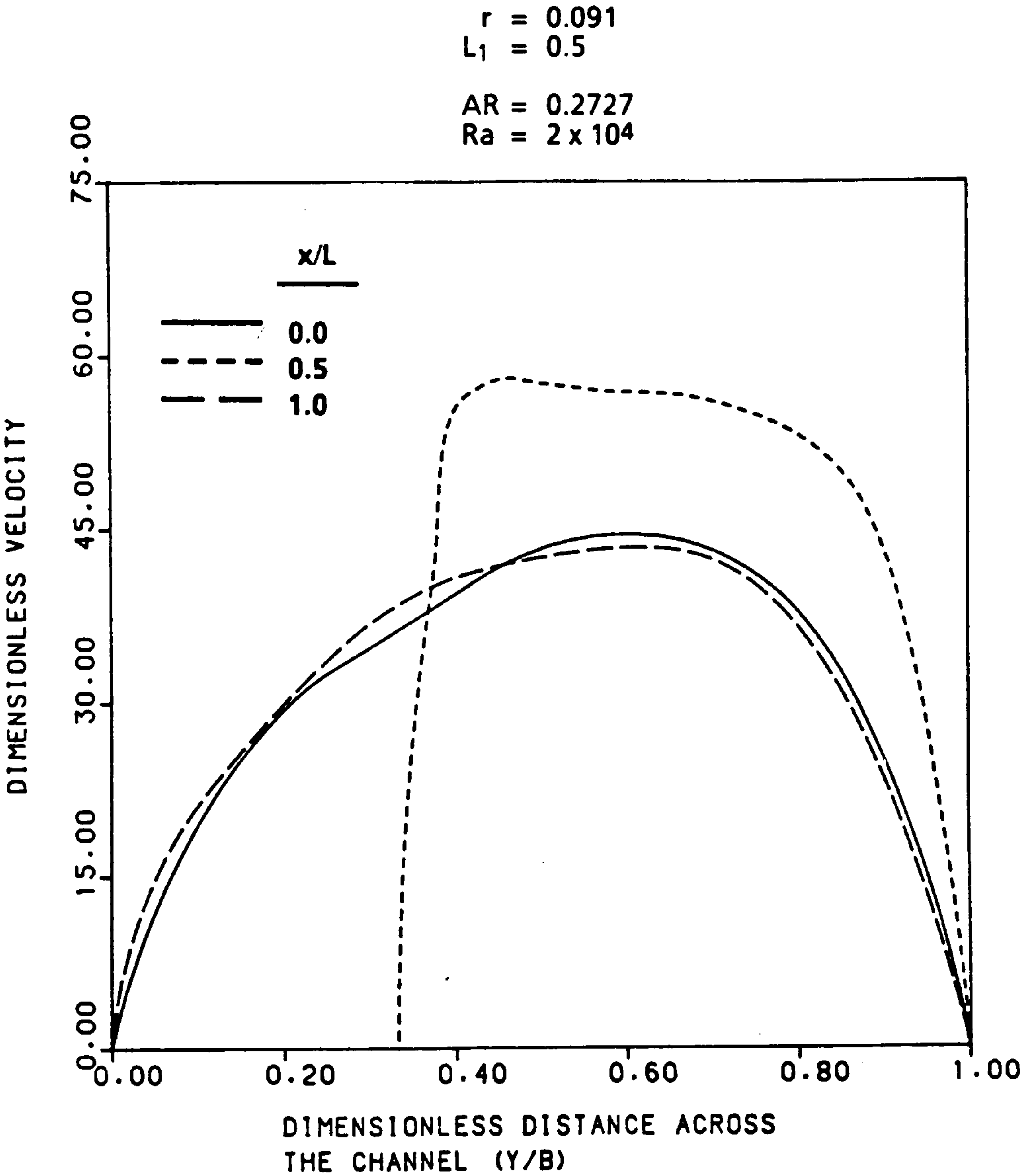

Figure 49. Transverse velocity distributions in the obstructed channel.

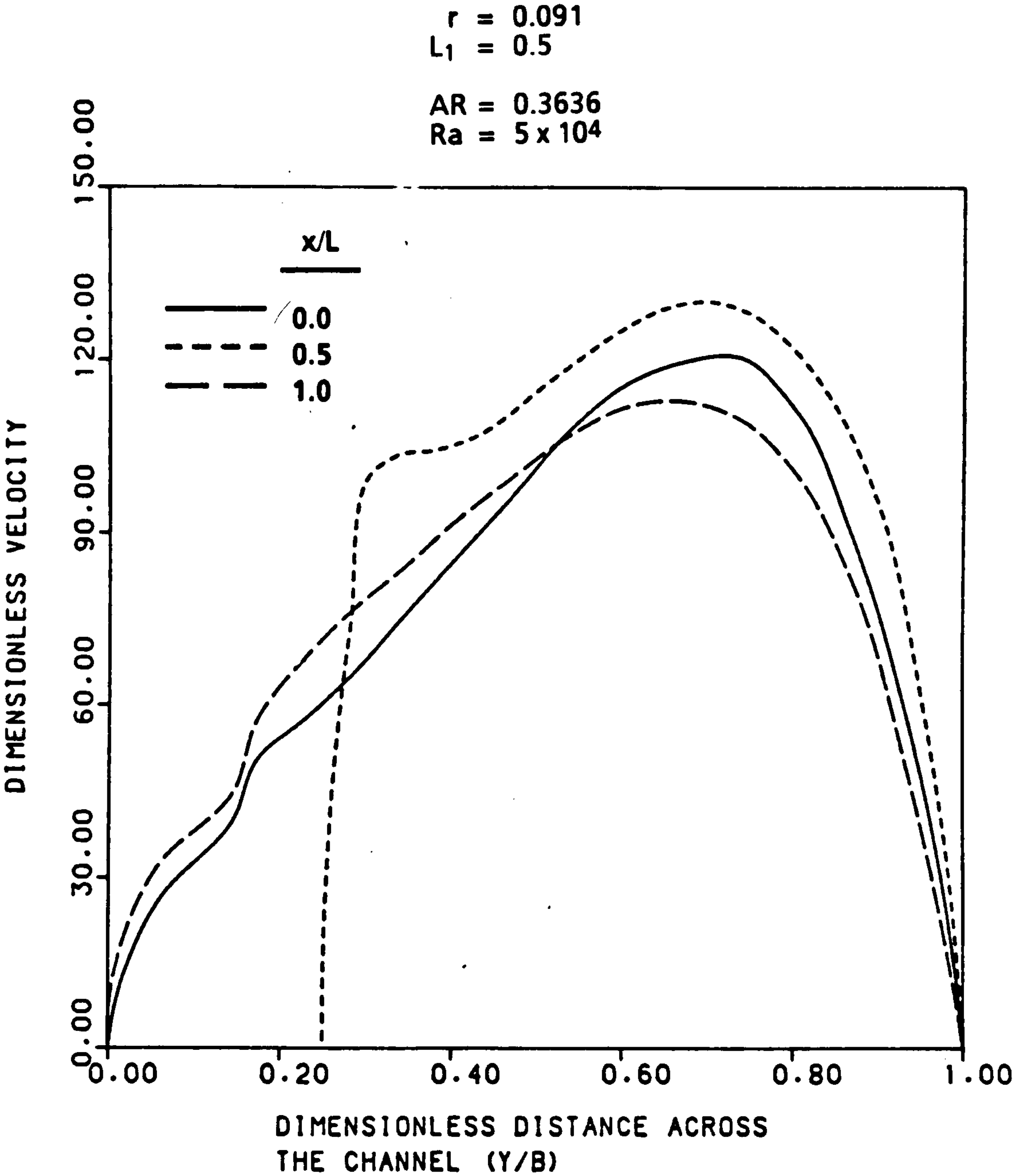

Figure 50. Transverse velocity distributions in the obstructed channel.

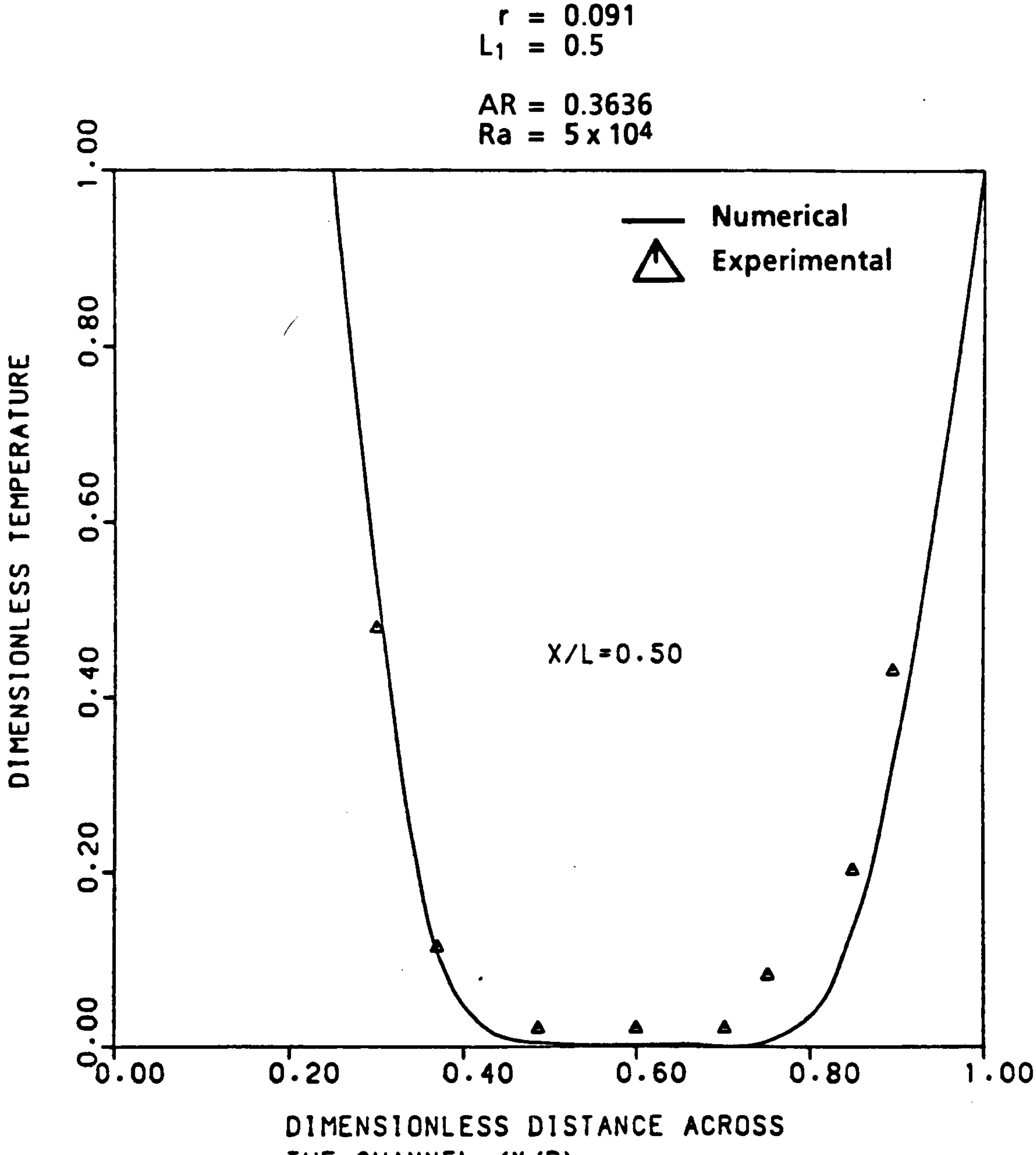

Figure 51. Comparison between the computed and measured temperature at x/L = 0.5 for the obstructed channel.

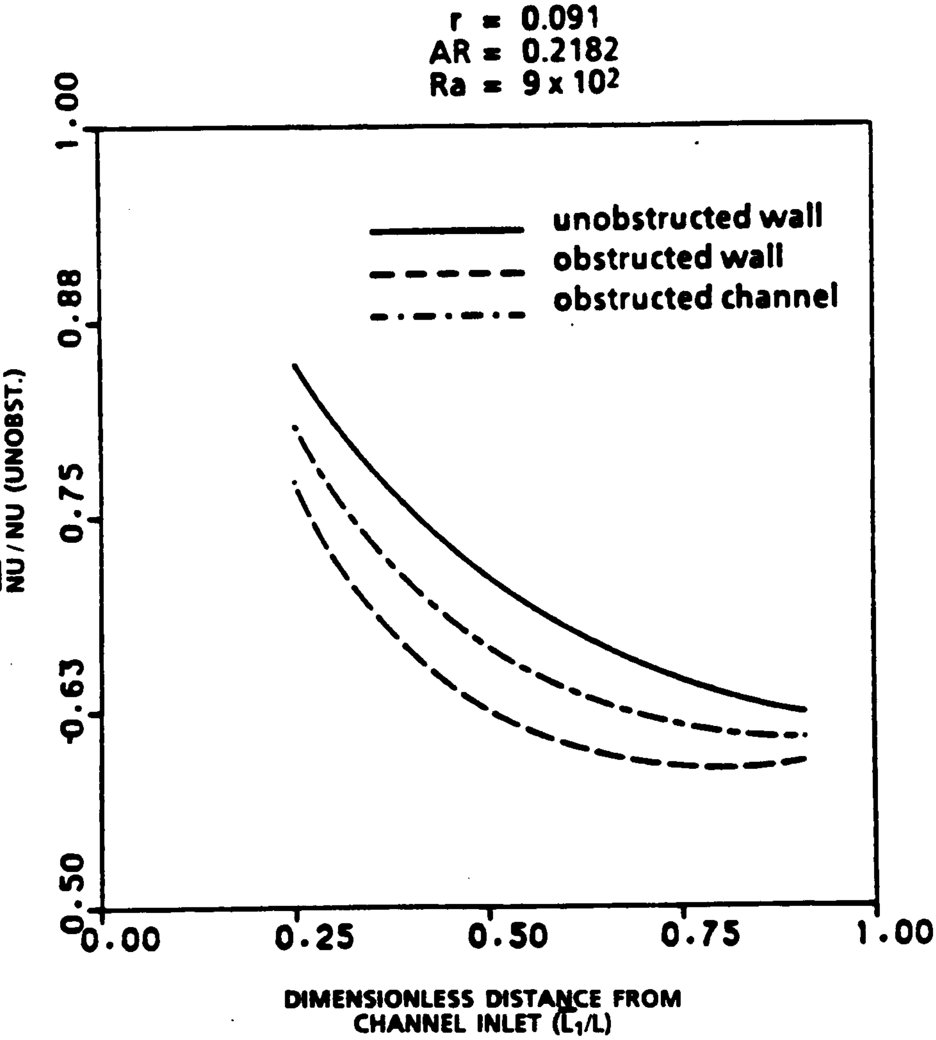

Figure 52. Effect of location of the obstruction ($\overline{L}_1$/L) on the average Nusselt numbers from the channel.

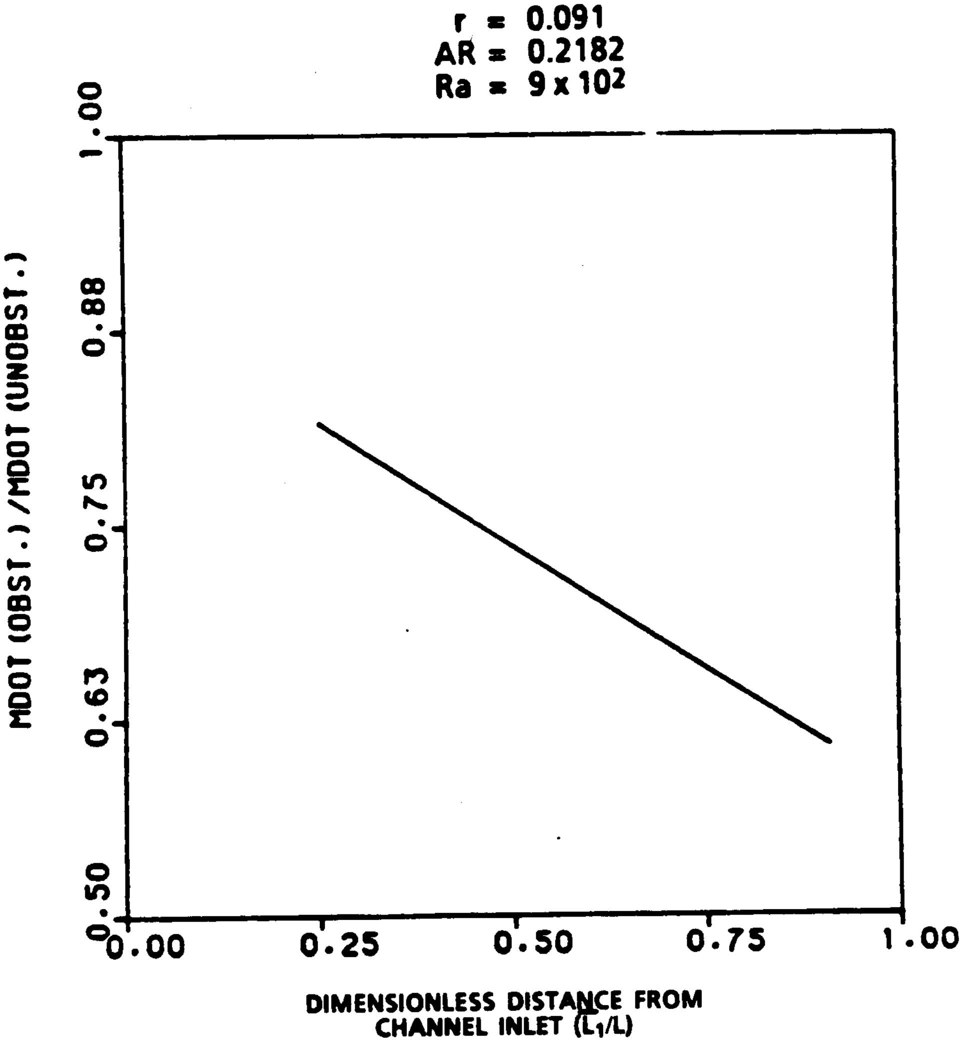

Figure 53. Relation between the mass flow rate through the channel and the location of the obstruction, ($\bar{L}_1/L$).

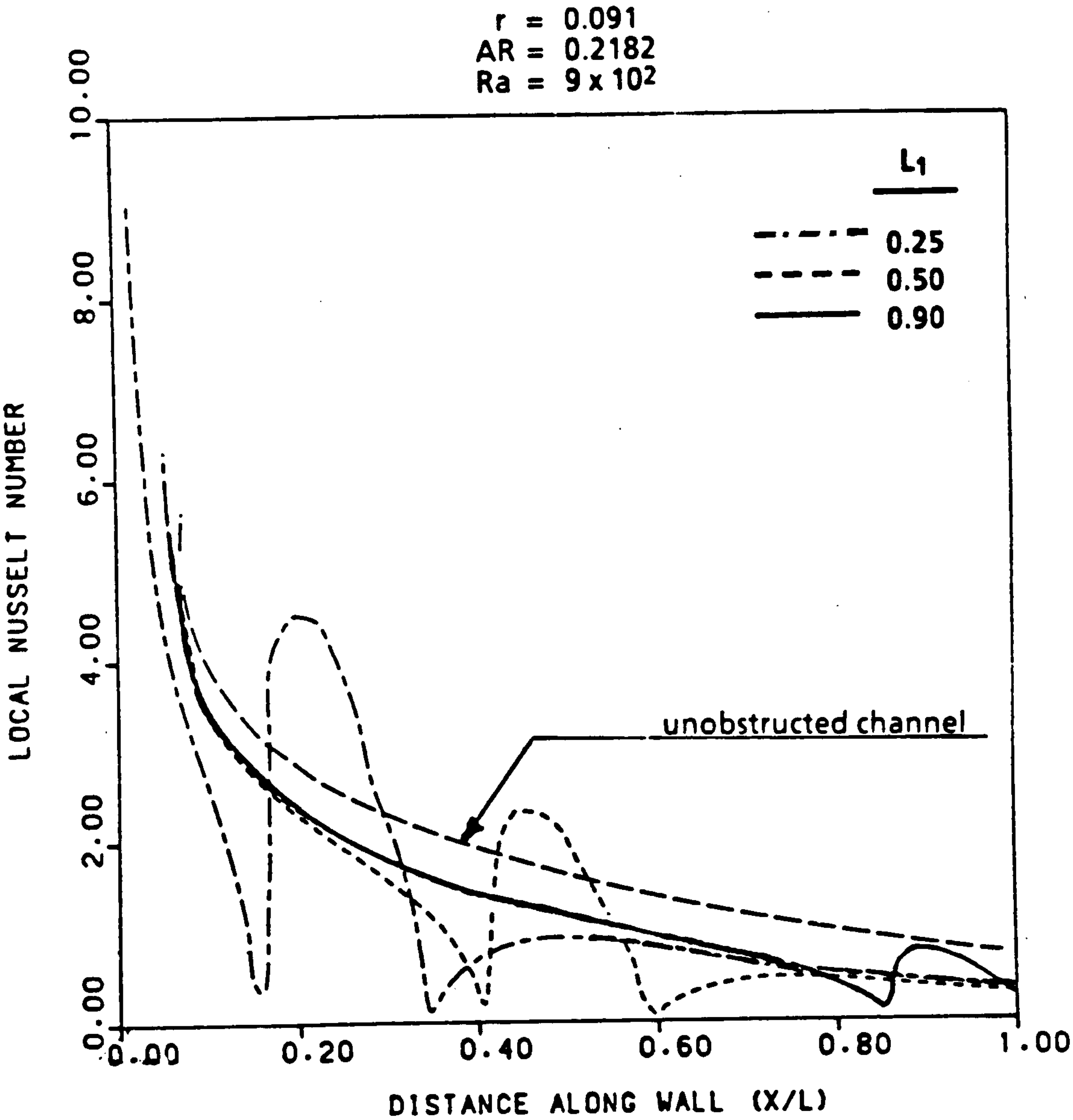

Figure 54. Variation of local Nusselt number with elevation in channel walls for different values of L_1.

r = 0.091
AR = 0.2182

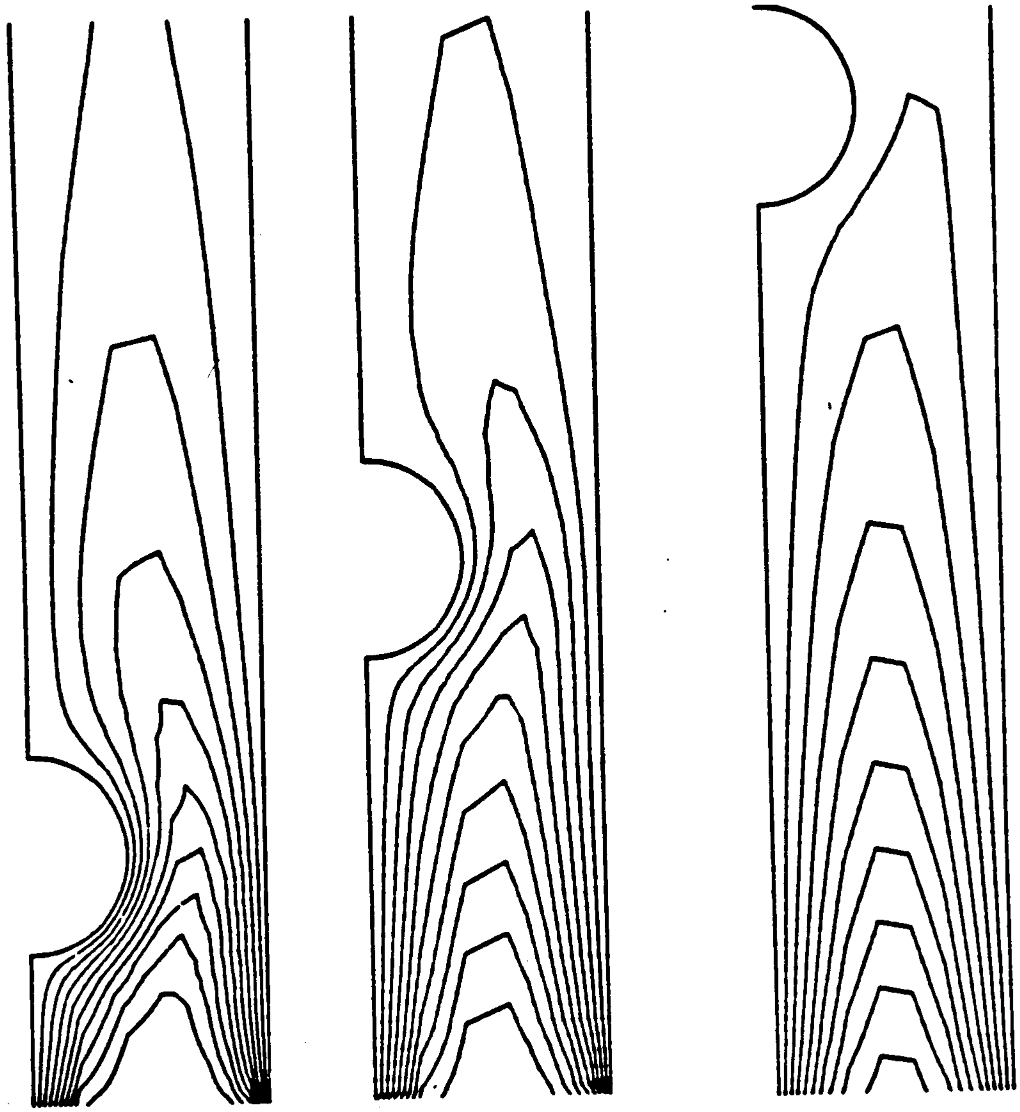

$L_1 = 0.25$ $L_2 = 0.50$ $L_3 = 0.91$

Figure 55. Computed isotherms for $Ra = 9 \times 10^2$ and different values of L_1.

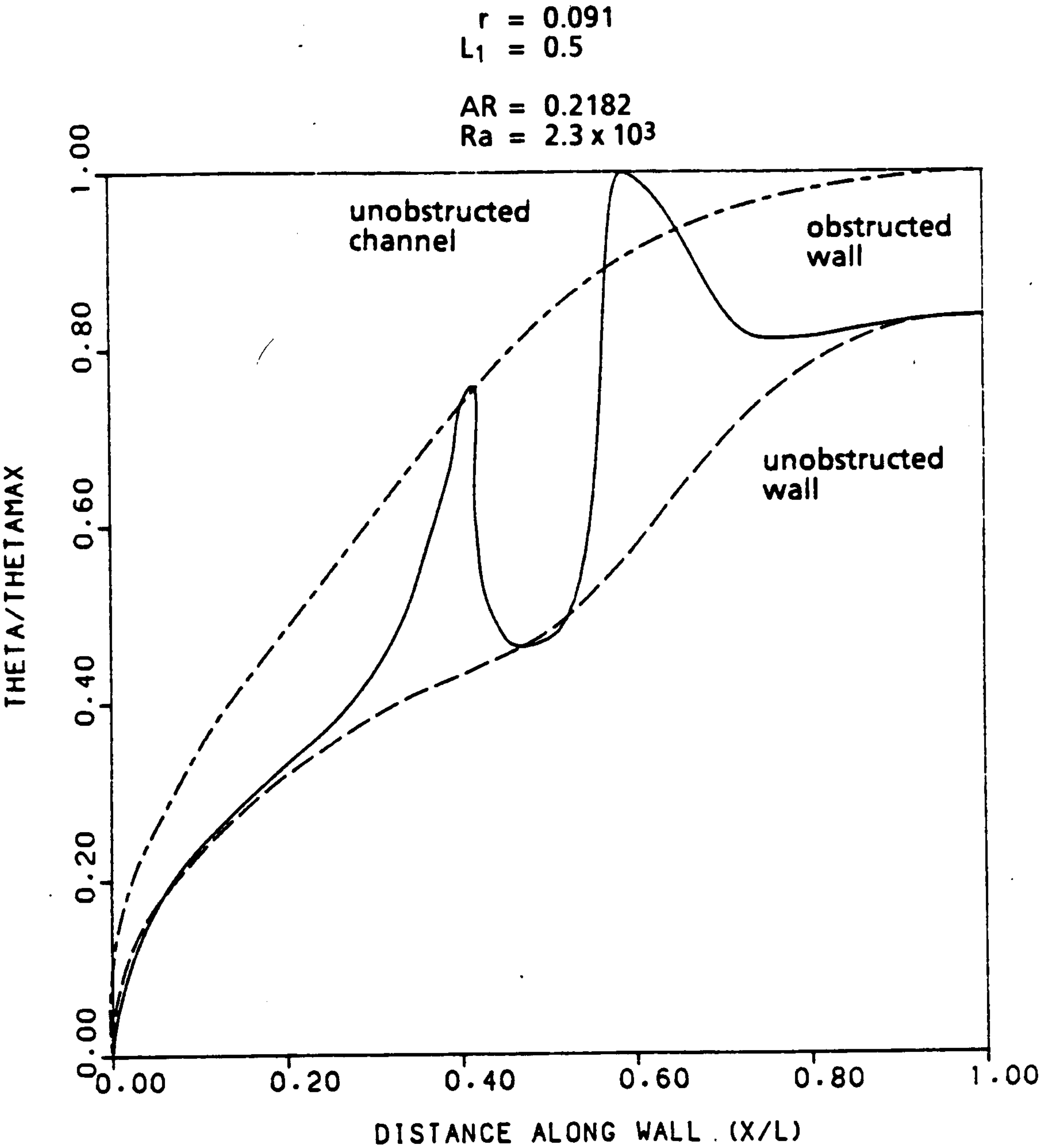

Figure 56. Axial variations of the walls temperatures for UHF.

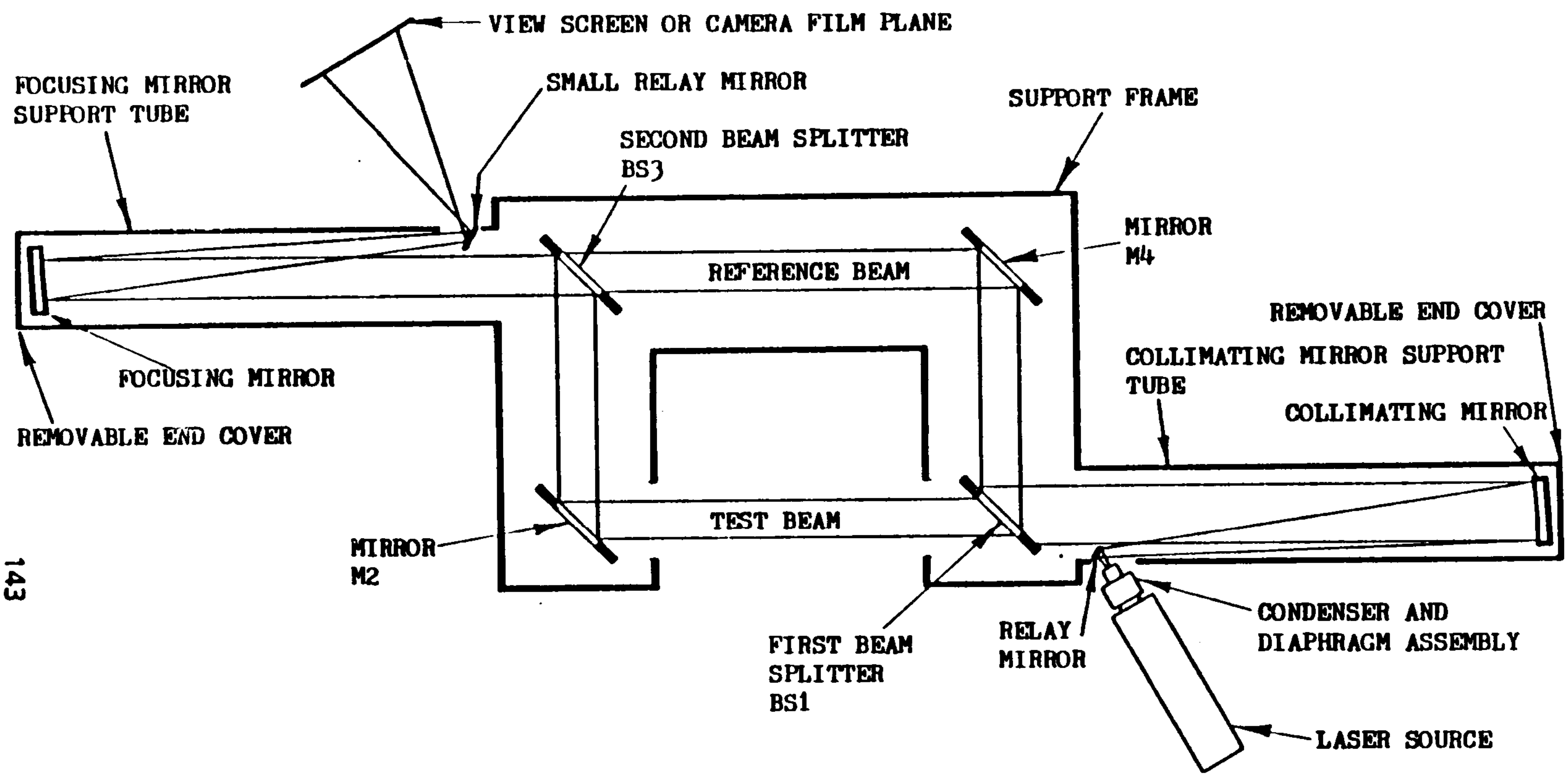

Figure B1. Layout of Aerolab, Inc. Mach-Zehnder Interferometer [46].

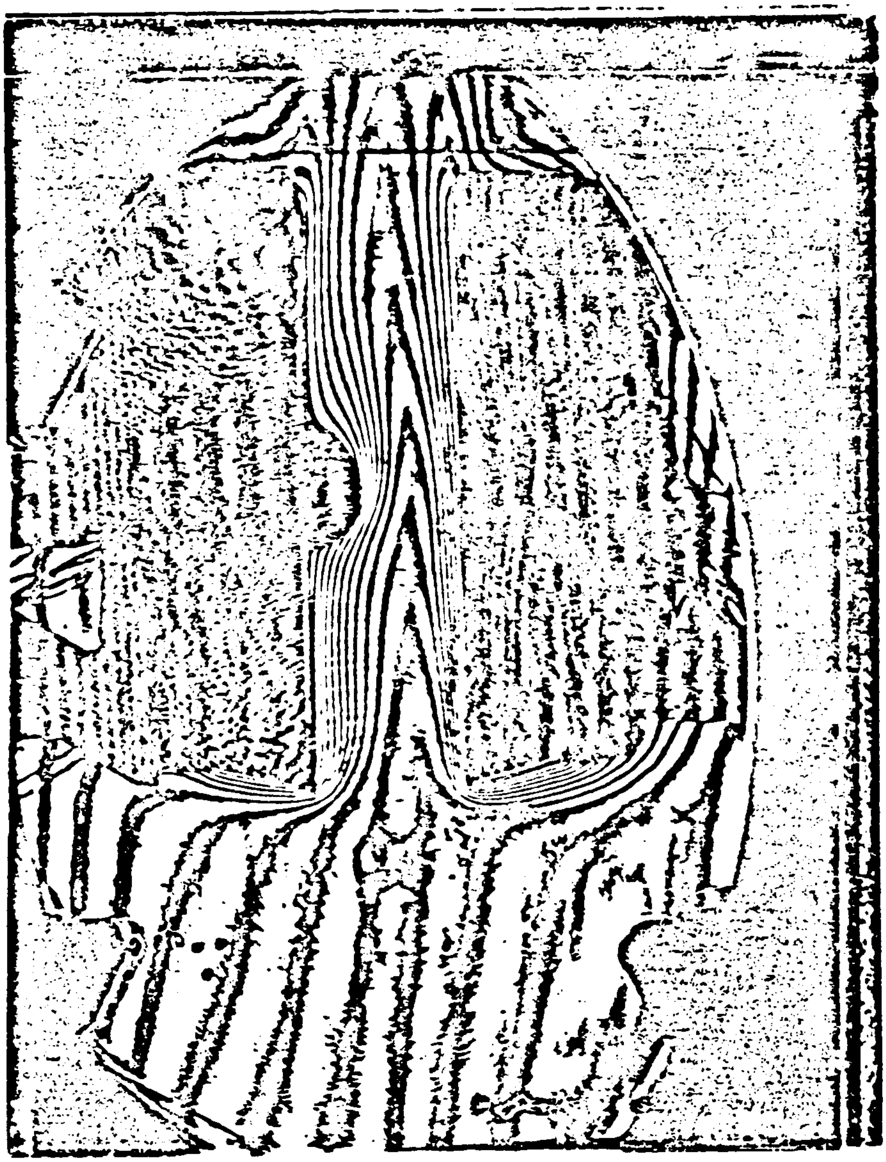

Figure B2. A reproduction of a MZI interferogram with MZI in the infinite fringe setting.

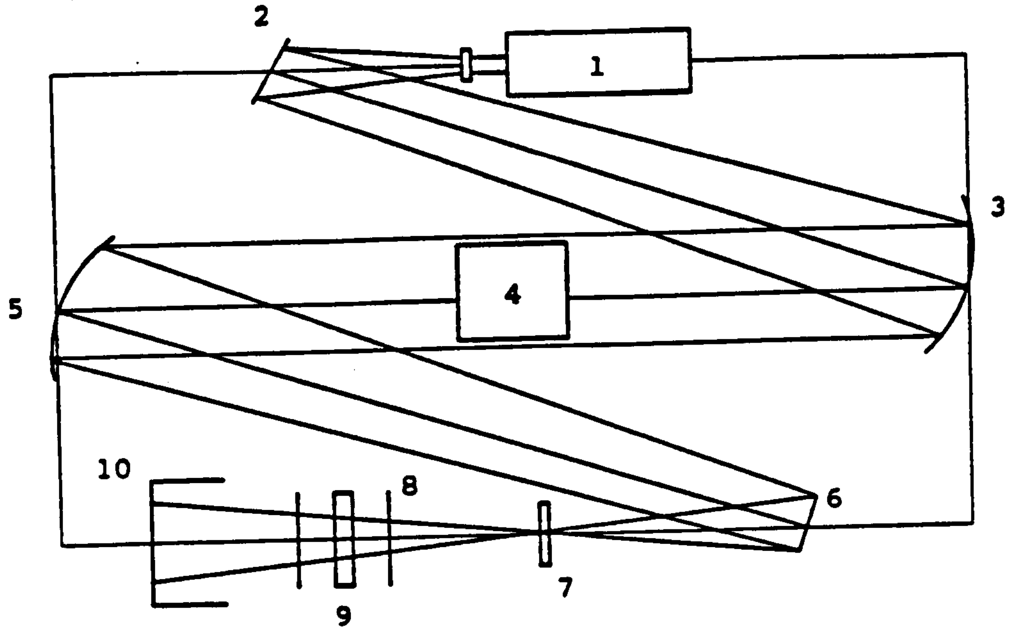

1. Laser
2. Plane Mirror
3. Spherical Mirror
4. Test Section
5. Spherical Mirror
6. Plane Mirror
7. Focusing Lens
8. Polarizer
9. Wollaston Prism
10. Camera

Figure C1. Schematic of The University of Tennessee's Wollaston Prism Schlieren Interferometer.

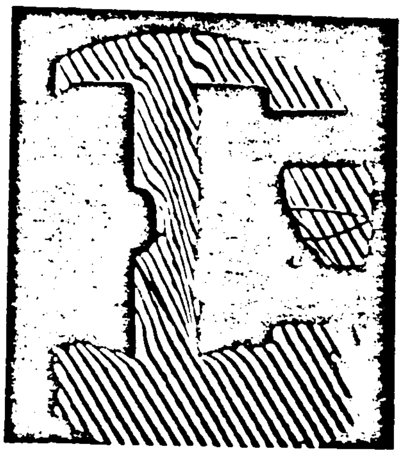

Figure C2. Wollaston Prism Interferometer fringe pattern.

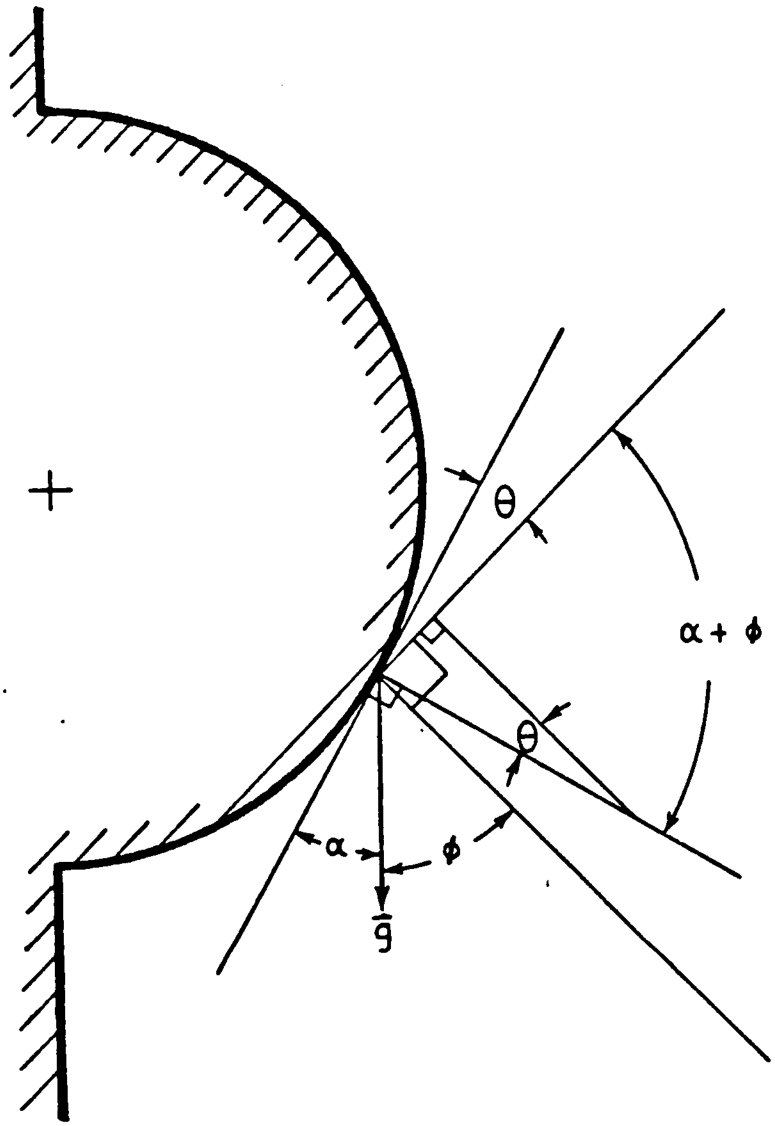

Figure C3. Determination of the angle, θ.

VITA

Syed-Ahmed M. Said was born in El Golid, The Sudan on November 22, 1951. He received a Bachelor of Science degree with honors in Mechanical Engineering from Brighton Polytechnic, Brighton, England in July 1976. In the Fall of 1977, he joined the Mechanical Engineering Department at the University of Petroleum and Minerals, Dhahran, Saudi Arabia as a Research Assistant; and began study toward a Master's degree. This degree was awarded in April 1979.

In June 1978, he joined the Research Institute (RI) of the University of Petroleum and Minerals as an Assistant Research Engineer. After four years of duty with the RI, he joined the Graduate School of The University of Tennessee, Knoxville, in June 1982. He received the degree of Doctor of Philosophy with a major in Mechanical Engineering in March 1986.

The author is a member of the Institution of Mechanical Engineers in the United Kingdom, and the American Society of Mechanical Engineers. He is married and has three children: Haithem, Mohammed and Hagar.